7-9-2008

Kaon photoproduction of the proton: contribution of higher angular momentum and energy resonances to the cross-section and polarization asymmetries through an effective Lagrangian model

Alejandro M. de la Puente
Florida International University

DOI: 10.25148/etd.FI14062219

FLORIDA INTERNATIONAL UNIVERSITY

Miami, Florida

KAON PHOTOPRODUCTION OF THE PROTON: CONTRIBUTION OF HIGHER ANGULAR MOMENTUM AND ENERGY RESONANCES TO THE CROSS-SECTION AND POLARIZATION ASYMMETRIES THROUGH AN EFFECTIVE LAGRANGIAN MODEL

A thesis submitted in partial fulfillment of the

requirements for the degree of

MASTER OF SCIENCE

in

PHYSICS

by

Alejandro M. de la Puente

2008

To: Dean Kenneth Furton
College of Arts and Sciences

This thesis, written by Alejandro M. de la Puente, and entitled Kaon Photoproduction of the Proton: Contribution of Higher Angular Momentum and Energy Resonances to the Cross Section and Polarization Asymmetries through an Effective Lagrangian Model, having been approved in respect to style and intellectual content, is referred to you for judgment.

We have read this thesis and recommend that it be approved.

Brian Raue

Stephan Mintz

Oren V. Maxwell, Major Professor

Date of Defense: July 9, 2008

The thesis of Alejandro M. de la Puente is approved.

Dean Kenneth Furton
College of Arts and Sciences

Dean George Walker
University Graduate School

Florida International University, 2008

DEDICATION

To my brother. The fighter and the wise, who always reminded me that nothing should stop me. You always told me that I could! I love you!

ACKNOWLEDGMENTS

I would like to thank my advisor Dr. Oren Maxwell for giving me the opportunity to work with him, and for his guidence throughout the course of this study as well as in my graduate career. Thanks also to the members of the committee for reviewing the thesis and providing their most valuable insight. Special thanks to Dr. Brian Raue for his mentorship and understanding.

Special thanks to my friend and colleague Brian Beckford for his guidence and mentorship in my life's journey. Thanks also to all the members of the Physics Department at Florida International University, for their guidence and support throughout the course of my studies.

Infinite thanks to my mother, for her mentorship, guidence, dedication and hardwork throughout my life. She is really a superhero. Thanks to my family, for their unconditional love and support. Thanks to my partner and best friend Jennifer, for helping me understand and reinforce the idea that there is a beautiful and positive side in everything.

ABSTRACT OF THE THESIS

KAON PHOTOPRODUCTION OF THE PROTON:

CONTRIBUTION OF HIGHER ANGULAR MOMENTUM AND ENERGY RESONANCES

TO THE CROSS-SECTION AND POLARIZATION ASYMMETRIES

THROUGH AN EFFECTIVE LAGRANGIAN MODEL

by

Alejandro M. de la Puente

Florida International University, 2008

Miami, Florida

Professor Oren Maxwell, Major Professor

The differential cross-section and polarization observables in the process $\gamma + p \rightarrow K^+ + \Lambda$ are studied within an isobaric approach that includes resonances with total angular momentum $J \leq \frac{5}{2}$ over a center of mass energy range from $W = 1.6$ GeV to $W = 2.6$ GeV. The model is used to fit recent experimental data as a function of the coupling products at the photon and strong vertices for the well established low energy resonances, as well as the total decay width for the high energy less well-established resonances.

The model employed in this study is based on an effective hadronic lagrangian using a tree-level approximation. The model uses Feynman diagrammatic techniques to extract the interaction vertices at a first order level in perturbation theory.

To extract the coupling strength products involved in the reaction, a χ^2-minimization technique is used to fit experimental data. The results suggests that both differential cross-section and double polarization observables need to be fit simultaneously to obtain an accurate description of the data. In addition, it was found that while resonances with angular momentum $J = \frac{5}{2}$ do not couple strongly to the $K\Lambda$ channel, higher energy states with $J = \frac{3}{2}$ do couple strongly to the $K\Lambda$ channnel and are highly relevant for an accurate description of the data at energies beyond 1.9 GeV.

TABLE OF CONTENTS

LIST OF TABLES

TABLE PAGE

FIGURE PAGE

Chapter 1

Introduction

Nuclear physicists study the structure of matter, and try to describe its interactions at a nuclear level. Theoreticians in nuclear physics use models that allow them to predict the properties of matter.

The reaction of interest for this study is the photoproduction of kaons from a proton target. To fully understand this reaction in an intermediate energy regime, it is important to study and include all well-accepted resonances.

1.1 Photoproduction

The overall photoproduction of mesons started with the works of Thom [1] and Renard [2] over 30 years ago and has been an extremely interesting topic of research since. This area of nuclear physics brings insight into understanding quark-model related research and experimental observation. A substantial number of Quantum Chromodynamics (QCD) inspired models have theorized the existence of a wide spectrum of baryonic and hyperonic excited states, i.e. resonance states. It seems that QCD, which appears to be the correct theory for strongly interacting particles, predicts more resonances than have been seen through analysis of experimental data.

The study of photoproduction has become an excellent tool for nuclear physicists since it is used mostly to probe the internal structure of both the proton and the neutron. There is still much to learn about the internal dynamics, as well as the spin and flavor structure of the nucleon. The resonance spectrum has been mostly studied by the production of pions and agrees well with predictions of various quark models. However, strangeness does not play a role in pion production reactions, and thus, pion reactions cannot be used to sudy hyperons and their excited states, which have been predicted with the same degree of significance. Furthermore, a large number of heavier less well-established nucleon resonances have been predicted but are not evident through pion photoproduction.

1.2 Quark models and strangeness production

Unlike pion photoproduction, the production of kaons introduces the strangeness degree of freedom. Quark models that study the spectrum of observed and predicted baryons incorporate the strange quark with a similar mass to the up and down quarks. Quark models make use of symmetries that govern interactions and use the language of group theory to arrange hadrons in representations of fundamental groups, such as flavor in an $SU(3)$ Lie algebra. Quark models using flavor $SU(3)$ have predicted with great success various fundamental properties of the hadrons' ground and excited states [3].

A larger symmetry has also been proposed and takes into account the intrinsic spin belonging to the constituent quarks and their relative angular momentum. The particles belonging to this group are members of representations of the group $SU(3) \otimes SU(2) \otimes O(3)$. This group representation has been used to explain the spectrum of excited states of hadrons. It also predicts symmetry relations of the interactions between mesons and baryons of different spins [4, 5, 6, 7, 8].

Due to the difference in mass between the u, d and s quarks, it has been very difficult to associate the wide spectrum of excited baryon and meson states with the right irreducible representations of the different symmetry groups. There is no clear explanation yet on why different flavors of quarks attain different masses.

1.3 Effective Models

Experiments in kaon photoproduction taken place within the medium energy regime, that is from threshold at 1.6 GeV up to, recently 2.6 GeV. In fact, cross-section and double polarization data for this energy region with high quality statistics are now available and have been made public by the CLAS collaboration [9, 10, 11]. Unfortunately, this energy regime is too low for a theoretical description using fundamental theories such as perturbative QCD or global symmetry models such as $SU(3)$ and $SU(6)$. Therefore, QCD cannot yet give a complete and concise picture that describes the reaction of interest as well as a full description of the wide spectrum of hadrons and mesons that exist in nature.

Effective models such as the isobaric approach bypass the difficulties encountered within the nonperturbative region of QCD by treating the interacting hadrons as fundamental point-like particles. They also assign to the photoproduction reaction a set of unknown coupling constants characterizing the different excited states involved, which are treated as parameters within a fitting scheme to experimental data.

In effective models, such as the one described in this study, the parameter that one tries to accurately extract is the leading coupling constant, $g_{kN\Lambda}$. This parameter determines the strength of the interaction between the kaon, proton, and lambda particles. Quark models such as [3] can be used to extract the leading coupling, using symmetry relations, from well established couplings such as $g_{\pi NN}$. The correct value for the $g_{\pi NN}$ coupling has been deduced using QCD sum rules [12]. QCD sum rules have also been used to calculate $g_{KN\Lambda}$ with results well within the value predicted using $SU(3)$ flavor symmetry [13].

Effective models in photoproduction are thus designed to provide more comprehensive knowledge of the production of strangeness as well as answer why and how the mediators in the reaction couple to hyperons, baryons and mesons. They also rely heavily on present experimental data, making them an excellent tool for understanding why there seems to be such a wide spectrum of resonances.

1.4 Motivation

There has been extensive research devoted to the modeling of strangeness photoproduction data with hopes of extracting the leading coupling constant, as well as the various couplings to the intermediate nucleon and strange resonances, N^* Y^* respectively. Resonances carry intrinsic spin, S, like their born-term counterparts and angular momentum L due to the motion of the constituent quarks. Resonances grouped in multiplets (similar mass) have the same total angular momentum, J, and parity of their spatial wavefunction. Most previous studies, such as the ones by Adelseck [14] and Maxwell [15], have not incorporated states with total angular momentum greater than $\frac{3}{2}$. Adelseck argued, based on previous literature, that since most experiments were conducted at energies near threshold, high angular momentum states could not be easily excited and thus were not necessary. The exclusion of resonances with $J \geq \frac{3}{2}$ was also due to a lack of well established data above the energy of 1.9 GeV.

There have been other theoretical models that do include resonances with $J = \frac{5}{2}$, such as those described by Lamot [16] and Mizutani [17]. These two works discussed in depth the nature of the spin $\frac{5}{2}$ vertices as well as the prescription for the propagator in the s-channel. The u-channel contribution of spin $\frac{5}{2}$ has not been included in previous models.

As mentioned in Section (1.3), at experimental facilities, such as CEBAF at Jefferson Laboratory, enormous effort has been put into studies of the photoproduction of kaons from a proton target. High quality low energy data is now available below 1.9 GeV and can be used to obtain a better description of the reaction when compared to previous theoretical

models. The data for energies above 1.9 GeV motivates us to incorporate the well established spin $\frac{5}{2}$ resonances as well as higher-energy spin $\frac{1}{2}$ and $\frac{3}{2}$ resonances. This energy regime is particularly interesting since the latest version of the Particle Data Book [18] does not contain any well-established nucleon resonances at around 1900 MeV with $J = \frac{1}{2}, \frac{3}{2}$. There is a wide overlap of less well-establshed resonances around this energy. The model will incorporate two $J = \frac{3}{2}$ states, one P_{13} resonance at 1900 MeV and one D_{13} resonance at 2080 MeV. The latter has been shown to play an important role in the analysis of the data by Sarantsev [19] and has also been discussed as part of the missing resonance problem by Benhold and Mart [20, 21]. In addition, theoretical models, such as a relativistic quark model by Capstick and Roberts [22], predict multiple states around 1900 MeV, that couple strongly to the $K^+\Lambda$ channel. States in this group, such as a P_{13} state at 1950 MeV and a D_{13} at 1960 MeV could correspond to those taken from the Particle Data Book and incorporated in this study.

With the additional resonances, it should be possible to fit the cross section data [9] and polarization observables [10, 11] for this reaction more accurately. Better knowledge of the coupling constants involved in the reaction and the mechanism for the production of strangeness will also be available through this phenomenological approach. Furthermore, it should be possible to deduce the number of effective parameters in the fit by determining which resonances couple strongly to the $K^+\Lambda$ channel.

Chapter 2

The theory of quarks

Contents

This chapter provides a brief introduction to quark models, in particular the $SU(6) \otimes O(3)$ model. It also introduces the theory of QCD, and what motivated its origin. Quark models, make use of symmetries to study the spectrum of particles that have been shown to play an important role in the analyses of experimental data of pion and kaon production reactions. The symmetries that quark models introduce are not exact in nature, as can be seen from the mass splitting between the particles belonging to the $SU(3)$ flavor irreducible representation; nonetheless, quark models provide useful guidelines for the introduction of resonances into effective lagrangian models, such as spin-parity assignments.

2.1 The Quark Model

QCD is believed to be the correct theory of the strong interaction. It has had incredible succcess explaining the behavior of matter at high energies where the strong coupling constant can be taken close to zero and one is able to do perturbation theory to extract physical obervables. On the other hand, the confined nature of QCD in the low energy regime makes it difficult to do first principle calculations to extract observables.

Most of the nucleon resonance spectra observed in kaon and pion photoproduction experiments occur within this low energy regime, up to 3 GeV. One has to rely on different phenomenological models to explain the properties of the excited states of baryons and hyperons.

2.1.1 The early 1960's

In the early 1960's Gellman [23] and Zweig [24] introduced the theory of flavor $SU(3)$ symmetry. This theory assumed the strong interaction to be invariant under continuous global $SU(3)$ transformations. This model treated as fundamental particles three quarks with three different flavors: strange (s), up (u), and down (d) with their corresponding anti-particles.

$$u = \begin{pmatrix} 1 \\ 0 \\ 0 \end{pmatrix} d = \begin{pmatrix} 0 \\ 1 \\ 0 \end{pmatrix} s = \begin{pmatrix} 0 \\ 0 \\ 1 \end{pmatrix}. \tag{2.1}$$

The model properly explained the structure of the observed baryons as triplets of quarks and mesons as a quark anti-quark pair.

Quarks are fundamental particles obeying Fermi-Dirac statistics with spin $\frac{1}{2}$ and baryon number equal to $\frac{1}{3}$. This model was able to accurately assign the right combinations of quarks to the observed baryons and mesons by assigning the right quantum numbers to the quarks.

$$B = \begin{pmatrix} q_i \\ q_j \\ q_h \end{pmatrix} \tag{2.2}$$

$$M = \begin{pmatrix} q_i \\ \overline{q}_j \end{pmatrix}, \tag{2.3}$$

The theory grouped the u and d quarks in an isospin doublet due to their small difference in mass and assigned the heavier strange quark to an isospin singlet, Table (2.1). As

Flavor	Mass	Electric charge	Baryon number	Strangeness	Isospin I_z
up (u)	5 MeV	$\frac{2}{3}$	$\frac{1}{3}$	1	$\frac{1}{2}$
down (d)	10 MeV	$-\frac{1}{3}$	$\frac{1}{3}$	0	$-\frac{1}{2}$
strange (s)	200 MeV	$-\frac{1}{3}$	$\frac{1}{3}$	0	0

Table 2.1: Fundamental particles in the SU(3) model.

baryons and mesons are observed to have integer charge, fractional charges were assigned to the quarks. The strong interaction is observed to be isospin invariant with the $SU(2)$ (isospin) group as a subgroup of flavor $SU(3)$. This led to the realization that iso-symmetry had to be taken as a conserved subgroup of $SU(3)$ with the same diagonal operators as ordinary isospin, I_z and I^2. It followed then that the charge operator could be related to the z projection of isospin and the strange and baryon number operators related by the Gell-Mann-Nishijima formula [25].

$$Q = I_z + \frac{1}{2}(S + B). \tag{2.4}$$

Particles whose bound states are made of a quark-antiquark pairs are labeled mesons and have either total spin $S = 0$ or $S = 1$. When the relative angular momentum L between the quarks is 0, the quark antiquark pair combine to form an octet and a singlet in flavor $SU(3)$ with total angular momentum $J = L + S = 0$ for $S = 0$, and parity $P = (-1)^{L+1} = -1$ of the wavefunction.

$$\mathbf{3} \otimes \overline{\mathbf{3}} = \mathbf{8} \oplus \mathbf{1}. \tag{2.5}$$

A second ground state configuration is also possible for $L = 0$, but the two quarks have their spins aligned and are referred to as the ground state vector meson configuration. Both the pseudoscalar and vector ground state mesons are shown in Table (2.2).

Unlike mesons, baryons are bound states of three quarks. They combine to form a total spin system of $S = \frac{1}{2}$ or $S = \frac{3}{2}$

$$\mathbf{3} \otimes \mathbf{3} \otimes \mathbf{3} = \mathbf{10} \oplus \mathbf{8} \oplus \mathbf{8} \oplus \mathbf{1}. \tag{2.6}$$

The decomposition shown above is purely for particles. The antipartcles will form their own decuplet, octet and singlet respectively. The first $SU(3)$ multiplet corresponds to the ground state baryons with $L = 0$ and parity $P = (-1)^L = +1$ and is shown in Table (2.3) with the proton and neutron being members of this $J = \frac{1}{2}^+$ octet.

$S = 0$				
particle	mass (MeV)	quark content	strangeness	charge
π^+	140	$u\bar{d}$	0	+1
π^-	140	$d\bar{u}$	0	−1
π^0	135	$d\bar{d}$	0	0
K^+	494	$u\bar{s}$	+1	+1
K^-	494	$s\bar{u}$	−1	−1
K^0	498	$d\bar{s}$	+1	0
$\overline{K}^0$	498	$s\bar{d}$	-1	0
η	548	$u\bar{u}$	0	0
η'	958	$s\bar{s}$	0	0
$S = 1$				
ρ^+	770	$u\bar{d}$	0	+1
ρ^-	770	$d\bar{u}$	0	−1
ρ^0	770	$d\bar{d}$	0	0
K^{*+}	892	$u\bar{s}$	+1	+1
K^{*-}	892	$s\bar{u}$	−1	−1
K^{*0}	892	$d\bar{s}$	+1	0
$\overline{K}^{*0}$	892	$s\bar{d}$	−1	0
ω	784	$u\bar{u}$	0	0
ϕ	1019	$s\bar{s}$	0	0

Table 2.2: Ground state pesudoscalar and vector mesons within flavor SU(3) [26]

However, the model presented a major problem. The wavefunction of the quark system has to be antisymmetric, that is no two quarks can be in the same quantum state. The

$S = \frac{1}{2}$				
particle	mass (MeV)	quark content	strangeness	charge
P proton	938.3	uud	0	+1
N neutron	939.6	udd	0	0
Σ^-	1197.4	dds	−1	−1
Σ^0	1192.6	uds	−1	0
Σ^+	1189.4	uus	−1	+1
Ξ^-	1321	dss	−2	−1
Ξ^0	1315	uss	−2	0
Λ	1115.7	uds	−1	0

Table 2.3: Ground state baryon octet within flavor SU(3) [26]

discovery of the Δ^{++} particle in the 1950's did not appear to have the right wavefunction within flavor $SU(3)$. This particle was observed to have a totally symmetric wavefunction, which was forbidden by the Fermi-Dirac behavior of baryons.

2.1.2 Color and QCD

The theory of flavor $SU(3)$ was very successful in explaining the observed hadron spectrum, but it is not an exact symmetry of nature; the strange quark is heavier than its up and down partners. Furthermore, the $SU(3)$ flavor model predicted in many instances a symmetric wavefunction under the interchange of two quarks which violates Fermi-Dirac statistics. The reconciliation between the quark model and Fermi-Dirac statistics came with the introduction of a new quantum number by theorists such as Greenberg in 1964, and later supported by experiments at SLAC and MIT. They proposed that each quark would carry a hidden quantum number referred to as color charge and that each quark could come in one of three different colors: red, blue and green. Each quark was then represented by a color triplet.

$$q = R \cdot \begin{pmatrix} 1 \\ 0 \\ 0 \end{pmatrix} + B \cdot \begin{pmatrix} 0 \\ 1 \\ 0 \end{pmatrix} + G \cdot \begin{pmatrix} 0 \\ 0 \\ 1 \end{pmatrix}. \tag{2.7}$$

R, B, and G refer to the red, blue, and green basis coeffiecients. A pure red quark will have both B and $G = 0$.

This additional degree of freedom makes the wavefunction antisymmetric since no two quarks are allowed to have the same color. With this additional degree of freedom, a wavefunction of the form

$$|qqq >= (|spatial > |flavorSU(3) > \times |spin >)_S \times |color >_A \tag{2.8}$$

is assigned to each hadron. A refers to antisymmetric and S to symmetric under interchange of any two quarks. The resulting wavefunction is antisymmetric and hence obeys Fermi-Dirac statistics.

The theory of QCD, assigned each quark of a particular flavor to the fundamental representation of a local $SU(3)$ non-abelian gauge group in which the group operators (gluons) change a quark of one color to another color leaving the flavor unchanged. The discovery of asymptotic freedom in 1973 by Gross and Wilczek [27] led to the realization that QCD would be a good candidate for the strong interaction. Unlike flavor $SU(3)$, color $SU(3)$ is believed to be an exact theory of nature.

In addition to asymptotic freedom, non-abelian gauge theories experience confinement. The coupling constant between two quarks increases with their separation distance. This property of QCD gave the correct explanation as to why baryons and mesons are color singlet bound states of quarks. The lagrangian of QCD as given by Cheng [28] is

$$L_{QCD} = -\frac{1}{2} tr G_{\mu\nu} G^{\mu\nu} + \sum_{k=1}^{nf} \overline{q}_k (i\gamma^\mu D_\mu - m_k) q_k, \tag{2.9}$$

where $G^{\mu\nu}$ represents the QCD gauge field tensor. The non-abelian nature of QCD is inherent in the commutation relation satisfied by the gauge fields (gluons).

$$G_{\mu\nu} = \partial_\mu A_\nu - \partial_\nu A_\mu - ig[A_\mu, A_\nu]. \tag{2.10}$$

The occurrence of confinement at low energies represents a real problem for physicists today since it is still not clear as to how low energy QCD should be approached. One particular problem is the wide spectrum of hadrons with masses within this energy domain.

2.2 $SU(6) \otimes O(3)$ model

The octet model has been very successful in explaining the ground state spectrum of baryons as well as how the two irreducible representations (**8**) and (**10**) of flavor $SU(3)$ baryons couple to both ground state strange and nonstrange mesons. Furthermore, the symmetry relations within $SU(3)$ multiplets give predictions for mass mixing effects as well as the strengths of the coupling constants between baryons and mesons to the extent that this symmetry is realized in nature [3].

The fact that many baryons have been observed to have total angular momentum $J \geq \frac{3}{2}$ and negative parities has led many to believe that baryons belong to a higher symmetry group. Just as the constituent quark picture led to the octet model, models in which angular momemtum couple to spin generate the higher state spectrum of strange and non-strange baryons. A model in which flavor couples to spin is based on an $SU(6)$ symmetry group. The relative motion between the quarks can be treated through the rotational invariant group $O(3)$. This model has been extremely successful in explaining the spectrum configuration of both ground and excited state baryons. It has also predicted allowed transition amplitudes as well as mass mixing effects between states belonging to different irreducible representations of $SU(6) \otimes O(3)$ [4, 5, 6, 8, 22].

The widely accepted version of $SU(6) \otimes O(3)$ is one that only contains symmetric irreducible representations of the group. The antisymmetric total wavefunction for baryons is then obtained from the color antisymmetric part of the wavefunction as discussed in Section (2.1.2). The flavor-spin part of the wavefunction is obtained from the $SU(6)$ part

of the group, and the spatial part is obtained from an interaction Hamiltonian that describes the relative motion between quarks. This Hamiltonian can be well described by a three-dimensional harmonic oscillator potential such as the one employed by [4]

Within $SU(6) \otimes O(3)$, quarks can couple their spins to $S = \frac{1}{2}, \frac{3}{2}$. The flavor-spin coupling can be expressed mathematically by

$$\mathbf{6} \otimes \mathbf{6} \otimes \mathbf{6} = \mathbf{56_S} \oplus \mathbf{70_M} \oplus \mathbf{70_M} \oplus \mathbf{20_A}, \tag{2.11}$$

where S, M and A denote the symmmetric, mixed symmetric, and antisymmetric properties of the spin-flavor wavefunction under inter-change of any two quarks. The flavor-spin part of each of the $SU(6)$ multiplets is given by

$$\begin{aligned} \mathbf{56_S} &= (\mathbf{10}, \mathbf{4}) + (\mathbf{8}, \mathbf{2}) \\ \mathbf{70_M} &= (\mathbf{10}, \mathbf{2}) + (\mathbf{8}, \mathbf{4}) + (\mathbf{8}, \mathbf{2}) + (\mathbf{1}, \mathbf{2}) \\ \mathbf{20_A} &= (\mathbf{1}, \mathbf{4}) + (\mathbf{8}, \mathbf{2}). \end{aligned} \tag{2.12}$$

The assumption that the hamiltonian describing hadrons be invariant under $SU(6)$ transformations was mainly due to the dimensionality of the symmetric **56** multiplet which accounted for the 40 spin $\frac{3}{2}$ and 16 spin $\frac{1}{2}$ positive parity states that occurred within flavor $SU(3)$. The observation that the spectrum of nucleon resonances appeared as three-quark excitations into well defined bands was well described by the $O(3)$ rotaional invariance of the hamiltonian governing these particles [29]. The excitations can be explained by those that arise from a harmonic oscillator potential which involves both radial and angular momentum excitations between quarks. It is not yet clear as to which are the effective degrees of freedom that dominate the spatial interaction between quarks. One approach is to treat all three quarks independent and define two relative radial coordinates as well as motion with respect to the CM of mass. Another approach is to treat two quarks as an effective diquark particle and define two radial coordinates, one describing the diquark-quark excitation, and one the motion with respect to the center of mass.

This study includes strange and non-strange resonances with total angular momentum $J \leq \frac{5}{2}$. In the shell model described in [4], the composite structure of the hadron is due to a three quark system interacting via harmonic oscillator forces. The independent degrees of freedom are the relative motions between the quarks together with the center of mass motion. From such a dynamical model and the assumption that the total wavefunction representing the hadron must be symmetric when both spatial and spin-flavor wavefunctions are combined, one can arrange hadrons into multiplets of the unitary group $SU(6)$. $SU(6)$ symmetry mixes hadrons which couple their spins to $S = \frac{3}{2}$ and $S = \frac{1}{2}$. The harmonic oscillator shell model then incorporates the $O(3)$ symmetry of the hamiltonian and couples the orbital angular momentum to either spin. A hadron in its ground state belongs to the symmetric **56** multiplet and has total orbital angular momentum $L = 0$. When S and L combine, the total angular momentum J also couples to either $J = \frac{1}{2}$ or $J = \frac{3}{2}$. The case is different when the quarks are in an excited state such as the negative partity $L = 1^-$ state. Since this state corresponds to an antisymmetric spatial wavefunction, one can only arrange particles with $J = \frac{5}{2}, \frac{3}{2}, \frac{1}{2}$ to a mixed symmetry multiplet of $SU(6)$ such as the **70** multiplet. This multiplet can be decomposed into its $SU(3)$ and $SU(2)$ multiplets given by

$$\mathbf{70_M} = (\mathbf{10}, \mathbf{2}) + (\mathbf{8}, \mathbf{4}) + (\mathbf{8}, \mathbf{2}) + (\mathbf{1}, \mathbf{2}) \tag{2.13}$$

as in Eq. (2.12). In $SU(6)$, an $SU(3)$ octet of $S = \frac{3}{2}$ states mixes with a $SU(3)$ decuplet, octet and singlet of $S = \frac{1}{2}$. The mixing that occurs between $S = \frac{3}{2}$ and $S = \frac{1}{2}$ state has been studied extensively by [8] as well as their decays into the ground state of $SU(6)$, **56** $L = 0$ by pion emission. All the decays that occur from the first excited state into the ground state can be related through $SU(6)$ symmetry relations, but the high degree of mixing that occurs between states with higher angular momentum at energies around 2 GeV makes the task of calculating decay amplitudes more difficult.

What has been covered in this section are some of the essential ideas pertaining to quark models. Like flavor $SU(3)$, $SU(6)$ is not an exact symmetry of nature, and therefore cannot

give a cosncise description of the resonances that have been observed to contribute to the cross-section in both pion and kaon production. In addition, they seem to predict far more resonances [22] than the experimentally established ones given in Particle Data Tables [18]. Nonetheless, they provide with useful approximations on masses and decay amplitudes for states that may be included in phenomenological models that try to fit experimental data to study the contribution and behavior of resonances with higher angular momentum, such as the effective lagrangian employed in this study.

Chapter 3

Photoproduction of K^+

Contents

In this chapter we examine the overall mechanism for the photoproduction of a K^+ meson from a proton at rest in the laboratory frame using a real photon as probe. The kinematics in both the laboratory (LAB) frame and center of mass (CM) are discussed. We then look at the three possible mechanisms that involve the excitation of one intermediate state. Each of these depends on a particular invariant kinematical variable defined in the previous discussion.

Section (3.2) applies kinematics in the CM frame to calculate the cross-section for the inelastic scattering of two particles and its relationship to the reaction's amplitude. The polarization observables are then introduced to take into account the different quantum states of the particles and how they affect the cross-section. The details of the amplitude

and its derivation depend on the dynamics of the reaction and the specified mechanism for the production of a K^+. This is covered in the following chapter but its general relationship to Feynman diagrams is included in Section (3.2.3).

3.1 Photoproducion mechanism

3.1.1 Photons: Virtual and Real

Production of kaons from a proton target can take place using a real or a virtual photon. In this section we discuss the virtual probe and its advantages, as well as its differences, with the real probe. In the next section, the kinematics of the reaction with a real photon are discussed in depth.

The reaction induced by virtual photons is usually referred to as electroproduction. In electroproduction, a photon is produced by scattering an electron off the proton. When two charged particles interact, they do so by the electromagnetic interaction which is mediated by the quantum of light, photons.

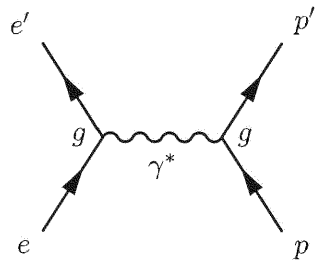

Figure 3.1: Electron-proton inelastic scattering: Virtual photon exchange

When photons are produced in this way, they must satisfy the Heisenberg uncertainty principle,

$$\Delta E \Delta t \geq \frac{\hbar}{2}. \tag{3.1}$$

The uncertainty principle allows for the production of energy if the time is short enough to satisfy the inequality in Eq. (3.1), but these photons fail to satisfy the on-shell condition for a particle with mass M and spatial momentum p.

$$E^2 = p^2 + M^2. \tag{3.2}$$

Unlike virtual photons, real photons have zero mass and hence obey the equation

$$E^2 = p^2. \tag{3.3}$$

In electrodynamics one finds that photons belong to a group of fields called gauge fields. This property of light requires the invariance of the electromagnetic (EM) field equations under a gauge transformation of the magnetic vector potential $\vec{A}$ and the scalar electric potential V. Recall from electromagnetism the wave equations that relate the potentials to the electromagnetic volume charge distribution ρ, and vector current $\vec{J}$.

$$\begin{aligned} -\frac{\rho}{\epsilon_0} &= \nabla^2 V + \frac{\partial \vec{\nabla} \cdot \vec{A}}{\partial t} = -\frac{\rho}{\epsilon_0} \\ -\mu_0 \vec{J} &= (\nabla^2 \vec{A} - \mu_0 \epsilon 2 \frac{\partial^2 \vec{A}}{\partial t^2}) - \vec{\nabla}(\vec{\nabla} \cdot \vec{A} + \mu_0 \epsilon_0 \frac{\partial V}{\partial t}). \end{aligned}$$

The freedom of gauge in the electromagentic potentials can be exploited to simplify the wave equations above. In particular, a choice of gauge may be made such that

$$\nabla \cdot \vec{A} + \frac{\partial V}{\partial t} = 0. \tag{3.4}$$

This gauge condition is known as the Lorentz gauge condition. It greatly simplifies the form of the wave equations.

In quantum electrodynamics (QED), which is the relativistic quantized theory of electrodynamics, the EM field is expressed by a polarization four vector ϵ.

$$V \rightarrow \epsilon_0 \tag{3.5}$$

$$\vec{A} \rightarrow \vec{\epsilon} \tag{3.6}$$

Furthermore, the momentum of the quantum of light can be expressed using the canonical relationship

$$p_u = -i\frac{\partial}{\partial x^u}. \tag{3.7}$$

In the Lorentz gauge, one has

$$p_\mu \cdot \epsilon^\mu = 0. \tag{3.8}$$

Eq. (3.3) can also be expressed in terms of a Lorentz four vector

$$p_\mu \cdot p^\mu = 0. \tag{3.9}$$

These last two equations, together with current conservation for real photons, ensure the orthogonality of the photon's direction of propagation with the polarization vector,

$$\vec{p} \cdot \vec{\epsilon} = 0. \tag{3.10}$$

Virtual photons do not satisfy Eqs. (3.8) and (3.9), and one can not use the tranverse property of light given in Eq. (3.10). However, using a virtual probe has its own advantages. Real photons are used mainly to extract the coupling strengths introduced in Section (1.4) by making use of an effective model in which the interacting particles are treated as mathematical points. By virtue of their masses, virtual photons acquire a longitudinal component which is a great tool if one wants to probe the internal structure of the proton. Experimentalists exploit both reactions since parameters easily found when using real photons can be fixed in electroproduction to accurately obtain several other parameters, such as electromagnetic form factors.

In the next section we discuss the general kinematics for the scattering of two particles. We then apply the results to the special case of a real photon scattering off a proton at rest in the LAB frame.

3.1.2 Reaction Kinematics

The field of nuclear and particle physics is a very complicated one in that the forces between particles are not yet very well understood. However, the field of classical relativistic mechanics is still applicable to describe the kinematics involved in reactions.

In classical relativistic mechanics, the total four momentum before and after the reaction must be conserved. This can be expressed simply by

$$P_i = P_f. \tag{3.11}$$

P_i is the total four momentum of the particles before the collision, and P_f the total four momentum after the collision. The total four momenta are defined as

$$P_i = (E_i, \vec{\mathbf{p}}_\mathbf{i}) \tag{3.12}$$

$$P_f = (E_f, \vec{\mathbf{p}}_\mathbf{f}). \tag{3.13}$$

With these definitions, conservation of energy and spatial momentum follow from Eq. (3.11).

In special relativity, one makes use of Lorentz transformations to go from one inertial reference frame to another. The two most widely used inertial frames in nuclear and particle physics calculations are the LAB frame and the CM frame. Four vectors span Minkowski space and thus their lengths do not change from frame to frame. Using this property one can write

$$P^2_{CM} = P^2_{LAB}. \tag{3.14}$$

The scattering of two particles can be depicted pictorially by Fig. (3.2) an the LAB frame and Fig. (3.3) in the CM frame.

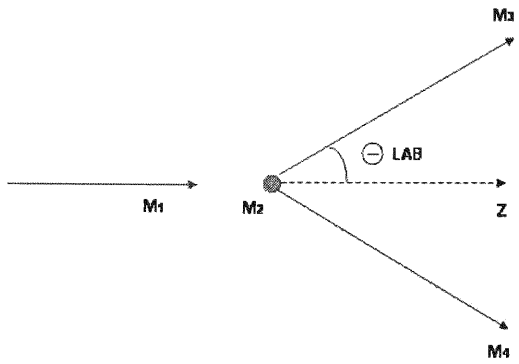

Figure 3.2: Scattering of two particles in the LAB frame

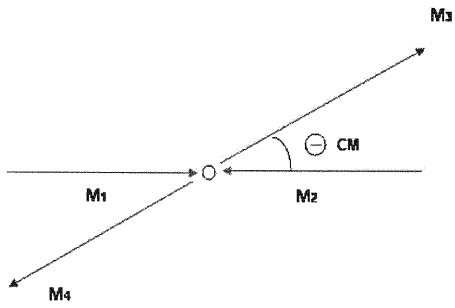

Figure 3.3: Scattering of two particles in the CM frame

In the LAB frame, a particle of mass m_1 with momentum $\vec{p_1}$ collides with a particle at rest of mass m_2. Their total four momentum is defined by

$$P_{LAB(i)} = (E_1 + m_2, \vec{\mathbf{p_1}}). \tag{3.15}$$

The CM frame is defined as the frame where the total spatial momentum of the colliding particles adds up to zero.

$$P_{CM(i)} = (E_1^{'} + E_2^{'}, \vec{0}). \tag{3.16}$$

The prime on the energies is used to differentiate between the energies of the particles in the two frames. The kinematics for the scattering reaction are expressed in a more compact way in the CM frame, since the total spatial momentum is zero. The total momentum squared in the CM frame is defined by

$$s = P_{CM(i)}^2 = (E_1^{'} + E_2^{'})^2, \tag{3.17}$$

and it is usually referred to as the squared energy of the center of mass. In the LAB frame, s can be expressed by

$$s = m_1^2 + m_2^2 + 2m_2E_1. \tag{3.18}$$

The invariant quantity $W = \sqrt{s}$ is fundamental in kaon photoproduction, since this is the energy for the production of the excited baryon that mediates the reaction in the s-channel. The excited state later decays into the final state particles m_3 and m_4. If the final state particles differ from the initial scattering bodies, as in this reaction, the reaction is said to be inelastic.

Since the four momentum is conserved, s can also be written using the final state particles. In the CM frame

$$P_{CM(i)}^2 = P_{CM(f)}^2 = s = (E_3^{'} + E_4^{'})^2. \tag{3.19}$$

In photoproduction m_1 is equal to zero. In the LAB frame, the proton is at rest with mass $m_2 = m_p$. The final state particle masses are labeled m_K for the kaon, and m_Λ for the lambda particle. Experimentalists use beams of photons to induce the reaction, and thus there exists a minimum energy which is necessary to induce the reaction and create the final particles at rest in the CM frame. This energy is referred to as the threshold energy

for the reaction. It can be obtained by using the following condition on Eq. (3.19) in the CM frame

$$(E_{\gamma}^{'} + E_{p}^{'})^2 \geq (m_K + m_\Lambda)^2. \tag{3.20}$$

For this reaction, the minimum CM energy squared is expressed by

$$s_{th} = (m_K + m_\Lambda)^2. \tag{3.21}$$

Since the proton is at rest in the LAB frame, the photon's threshold energy can be defined by solving for $E_1 = E_{\gamma(th)}$ in Eq. (3.17) with $m_1 = 0$. This yields

$$E_{\gamma(th)} = \frac{1}{2m_p}((m_K + m_\Lambda)^2 - m_p^2). \tag{3.22}$$

In this study, we look at three different mechanisms for the photoproduction of kaons, all of which include the exchange of one particle. The three different mechanisms are discussed in the following section.

3.1.3 Mechanism

In an isobaric approach, one makes use of Feynman diagrams to calculate the amplitude for the reaction

$$p + \gamma \rightarrow K^+ + \Lambda \tag{3.23}$$

The three possible mechanisms for the photoproduction of kaons correspond to the three Minkowski invariant quantities or Mandelstam variables s, u and t.

The Mandelstam variables are defines as follows:

$$s = (P_p + P_\gamma)^2 \tag{3.24}$$

$$u = (P_p - P_k)^2 \tag{3.25}$$

$$t = (P_\gamma - P_k)^2 \tag{3.26}$$

and which satisfy the following relationship:

$$s + u + t = M_p^2 + M_\Lambda^2 + M_k^2 \tag{3.27}$$

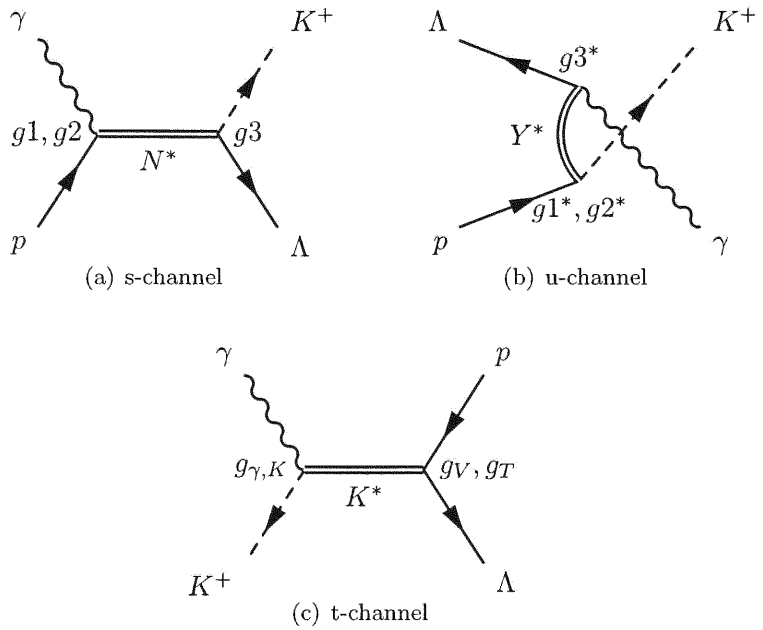

Figure 3.4: Contributions to the amplitude for the reaction $\gamma p \rightarrow K^+\Lambda$

Feynman diagrams corresponding to the three Mandelstam variables are depicted in Fig. (3.4). Although each diagram contributes to the reaction in a different way, they all affect the dynamics of the reaction. The s-channel diagram involves the invariant squared energy $s = (P_p + P_\gamma)^2$. The t and u-channel contributions affect the strength of the reaction at

forward and backward scattering angles, respectively. In the CM frame, solving for t and u in Eqs. (3.25) and (3.26) and using Fig. (3.3)

$$u = (E_p - E_K)^2 - \mathbf{p_p}^2 - \mathbf{p_K}^2 + 2 \cdot \mathbf{p_p} \cdot \mathbf{p_K} \cos(\Theta_{\mathbf{CM}}) \tag{3.28}$$

$$t = (E_\gamma - E_K)^2 - \mathbf{p_\gamma}^2 - \mathbf{p_K}^2 + 2 \cdot \mathbf{p_\gamma} \cdot \mathbf{p_K} \cos(\pi - \Theta_{\mathbf{CM}}). \tag{3.29}$$

Note that the t variable is large for forward angles, whereas u is large for backward angles so that the reaction's contributions can be expected to have a strong angular dependence.

The virtual particles exhanged in each diagram correspond to nucleon resonances in the s-channel, hyperon resonances in the u-channel, and kaon vector mesons in the t-channel. Born terms contributions are also included in the model for all three channels. The constraints, as well as the mechanisms to extract the individual channel contributions, will be discussed in Chapter 4. In the following section we discuss how observables are measured and how to make the connection with theoretical models.

3.2 Observables

3.2.1 Cross-sections

In experiments one usually uses detectors and different particle identification (PID) techniques to measure the likelihood of a certain outcome when two particles scatter. This likelihood is measured by the cross section and it is defined as

$$\sigma = \frac{N_{events}}{\rho_A l_A \rho_B l_B A}. \tag{3.30}$$

In Equation (3.30), ρ_x and l_x are the volume density and length of the bunches of particles that serve as the probe and target, A is the cross-sectional area of the incident beam, and N_{events} are the detected scattered events. It is related to the probability of detecting the scattered particles for a given flux of the initial particles.

Similarly, one can use quantum mechanics to define the probability of an event happening from some initial state. In quantum mechanics this can be expressed as

$$Probability = | < \psi_1\psi_2|\psi_A\psi_B > |^2 \tag{3.31}$$

ψ_i represent the final scattred state wavefunctions, and ψ_X represent the initial probe and target state wavefunctions. The states are constructed in the asymptotic limit where we can ignore any interaction between the initial or final states. Using a fourier transformation, one can construct each wavepacket from its momentum components by

$$|\psi >= \int \frac{d^3k}{(2\pi)^3}\frac{1}{\sqrt{2E_k}}\psi(k)|\mathbf{k} > . \tag{3.32}$$

To calculate the cross section one uses scattering theory, representing each particle by its corresponding wavepacket. This procedure is simplified by considering the initial states in the far past and the final states in the far future. In this way, there is no interaction between any of the states, and their wavefunctions can be constructed independently.

The formula to calculate two-body scattering cross sections is given by Peskin [30] in terms of the invariant matrix element, M, which contains all of the information concerning the interaction between the particles. In the center of mass frame (CM), the differential cross-section for the reaction $\gamma + p \rightarrow \Lambda + K^+$ is given by

$$(\frac{d\sigma}{d\Omega})_{CM} = \frac{1}{(2\pi)^2}\frac{m_p m_\Lambda |\mathbf{p_F}|}{4E_\gamma s}\frac{1}{4}\sum_{all_s pins}|M|^2, \tag{3.33}$$

where $\mathbf{p_F}$ is the outgoing three momentum in the CM frame and s is the squared CM energy. The differential cross-section given in Eq. (3.33) is an expression for the unpolarized cross section for the inelastic scattering of two particles. In kaon photoproduction from the proton, $p + \gamma \rightarrow K^+ + \Lambda$, the explicit factor of $\frac{1}{4}$ is from the average over the four spin projections of the incoming particles, two spin degrees of freedom for the proton and two polarization projections for a real photon. With this factor, the unpolarized cross section

is then given by a sum over the spin projections of all the particles, including for the study, both spin projections of the Λ. Cross sections are a very powerful tool used to test a theory since they can be directly related to experimental analyses. The following section makes use of the differential cross section and properties of the interacting particles to define polarization observables.

3.2.2 Polarization observables

Aside from an unpolarized cross section, experimentalists are equally interested in measuring the cross section when one or more of the interacting particles are polarized, that is, with their spin projection fixed to lie in definite directions. Furthermore, one is interested in the difference between the reaction's cross-section with a certain polarization configuration and the opposite configuration. These measured differences are referred to as polarization asymmetries.

In some cases, experimentalist have control over the polarization of the beam used to induce the reaction, and the target polarization. In the lab frame as depicted in Fig. (3.2), the direction of the beam or beam axis is given along the z-axis. If the beam consists of a real photon, its polarization can be either parallel or perpendicular to the scattering x-z plane (linearly polarized). The asymmetry measured between a parallel and perpendicularly polarized photon is given by the symbol Σ.

$$\Sigma = \frac{d\sigma^{||} - d\sigma^{\perp}}{d\sigma^{||} + d\sigma^{\perp}}. \tag{3.34}$$

If the photon beam has circular polarization, that is, if the helicity states are defined such that

$$\epsilon_1 = \frac{1}{\sqrt{2}}(\hat{x} + i\hat{y}),$$
$$\epsilon_2 = \frac{1}{\sqrt{2}}(\hat{x} - i\hat{y}), \tag{3.35}$$

then the asymmetry may be defined as

$$\Sigma = \frac{d\sigma^+ - d\sigma^-}{d\sigma^+ + d\sigma^-}, \tag{3.36}$$

where + refers to a helicity state in the ϵ_1 direction, and − to the ϵ_2 direction. In a similar way, single polarization observables may be defined for the outgoing hyperon. The hyperon asymmetry is given by

$$P = \frac{d\sigma^+ - d\sigma^-}{d\sigma^+ + d\sigma^-}. \tag{3.37}$$

The symbols + and − now refer to the polarization of the outgoing hyperon with respect to a defined quantization axis.

In most cases, it is interesting to measure the amount of polarization that is transferred from a polarized incoming particle to one of the outgoing particles. These types of asymmetries are referred to as double polarization asymmetries. The latest asymmetries measured by the CLAS collaboration [10] are C_x and C_z. The double polarization C_x measures the asymmetry that arises from a circularly polarized photon and a hyperon whose wavefunction is quantized along the $\hat{x}$ axis, that is whose spinors are rotated 90° from the original quantization axis ($\hat{z}$ axis). The double polarization C_x is given by

$$C_x = \frac{d\sigma^{+x^+} - d\sigma^{+x^-}}{d\sigma^{+x^+} + d\sigma^{+x^+}} \tag{3.38}$$

where the first superscript refers to the polarization of the photon, and the second to the polarization of the hyperon. Similarly, the double polarization C_z measures the asymme-

try that arises from a circularly polarized photon and a hyperon whose wavefunction is quantized along the $\hat{z}$ direction. C_z is given by

$$C_z = \frac{d\sigma^{+z^+} - d\sigma^{+z^-}}{d\sigma^{+z^+} + d\sigma^{+z^+}}. \tag{3.39}$$

The assymetries described above would be used together with the unpolarized differential cross-section data [9] to better constraint the behavior of the effective lagrangian model that will be employed to study the reaction $p + \gamma \rightarrow K^+ + \Lambda$ when fitted against experimental data. The study of polarization observables can yield insight into which resonances seem to be more significant for the description of the reaction of interest, in particular hyperon resonances.

3.2.3 Amplitudes from Feynman diagrams

Feynman diagrams are a powerful technique used to understand and relate an interacting theory of particles to experimental observation. A discussed in [30], one can calculate the amplitude of an interaction by summing over all connected, amputated Feynman diagrams. For an accurate description of the reaction of interest, it is essential to sum over all Feynman diagrams that correspond to the perturbative expansion of the effective dynamical theory. In an effective theory, suitable in the non-perturbative region of the strong interaction, the reaction's amplitude is studied in the tree level approximation, i.e. by calculating only the diagrams depicted in Fig. (3.4).

In field theory one usually derives the Feynman rules by first defining the vacuum to vaccum transition amplitude in the presence of external sources. The lagrangian for the reaction

$$p + \gamma \rightarrow K^+ + \Lambda \tag{3.40}$$

can be written in the form

$$L_{eff} = L_{free} + L_{interaction} + J_\mu A^\mu + \sum_{i=p,\Lambda} \eta_i \psi_i + \sum_{p,\Lambda} \psi_i \eta_i + \omega^\dagger k^+ + k^{+\dagger} \omega. \tag{3.41}$$

The vacuum to vacuum transition amplitude can be expressed by

$$W[J,\eta,\omega] \sim \int [d\psi]d[A_\mu][dK^+]e^{i\int d^4x(L_{free}+L_{int}+J_\mu A^\mu+\sum_{i=p,\Lambda}\overline{\eta}_i\psi_i+\sum_{p,\Lambda}\overline{\psi}_i\eta_i+\omega^\dagger k^+ + k^{+\dagger}\omega)} \tag{3.42}$$

with external sources J_μ for the photon field A_μ, η for the proton and Λ fields ψ and $\overline{\psi}$, and ω for the kaon field K^+. From this definition, quantities with physical significance, such as the amplitude M for Eq. (3.33) can be calculated. Feynman rules can readily be extracted by carrying out a perturbative expansion of the transition amplitude W and defining the Green's function

$$G^4(x_1,x_2,x_3,x_4) = \frac{\delta^4 lnW[J,\eta,\overline{\eta},\omega]}{(\delta J(x_1))(\delta\eta(x_2))(\delta\overline{\eta}(x_3))(\delta\omega(x_4))}. \tag{3.43}$$

Eq. (3.43) is proportional to the amplitude for the reaction between a photon and a fermion originating at x_1 and x_2 respectively and a fermion and scalar boson originating at x_3 and x_4. Green's functions of this form are best depicted by the following Feynman diagram

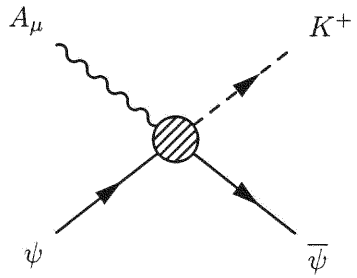

Figure 3.5: Feynman diagram for 4-point Green's function

The interaction piece of the effective lagrangian is essential in the calculation of the 4-point Green's function. The interaction lagrangian for all s and u-channels diagrams given in Fig. (3.4) will be introduced in Chapter 4. Since these are the diagrams to be considered as contributions to the cross section, the Feynman rules for such diagrams are stated here. The Feynman diagrams involve only one internal line which represents the virtual particle exchanged. The virtual particles considered in the study are both nucleon and hyperon

resonances with total angular momentum $J \leq \frac{5}{2}$. Internal lines are described by a two point Green's function with a momentum distributionn given by

$$\Delta(x-y) = \int \frac{d^4k}{(2\pi)^4} \Theta(k) e^{k\cdot(x-y)}. \tag{3.44}$$

The function $\Theta(k)$ will depend on the angular momentum exchanged and will be introduced in Chapter 4.

The interacting particles can be described by external lines whose states can be described as free particles with momentum p some time before or after the interaction. The fermion's wavefunction, a solution to the free Hamiltonian, can be expressed by a superposition of free waves of momentum p

$$\psi(x,t) = \int \frac{d^3p}{\sqrt{2E}} \sum_s u^s(p) e^{-ip\cdot x} \tag{3.45}$$

where $u^s(p)$ is a Dirac spinor, and the sum over s indicates a sum over the fermion's spin. Similarly the kaon free wavefunction can be expressed by

$$\phi(x) = \int \frac{d^3p}{\sqrt{2E}} e^{-ip\cdot x}. \tag{3.46}$$

Plane wave functions for photons can be obtained from

$$A_\mu = \int \frac{d^3p}{\sqrt{2E}} \sum_r \epsilon_\mu^r(p) e^{-ip\cdot x}, \tag{3.47}$$

where ϵ_μ^r indicates the polarization vector of the photon, and the sum over r indicates a sum over the photon's spin. A vertex can be expressed by the product of the interaction's strength with an integral over the Minkowski volume at the point of interaction. In this framework, the meson vertex is given by

$$(g_s) \int d^4x, \tag{3.48}$$

and the charge contribution to the photon vertex by

$$-ie\gamma^{\mu}\int d^4y. \tag{3.49}$$

Using the functional method, one can write the reaction's amplitude for these vertices to first order in the couping strength product as a vacuum-to-vacuum correlation function in which a photon and proton with momentum p_1 and p_2, respectively, are annihilated, and a K^+ and Λ with momentum p_3 and p_4 respectively are created from the vacuum as

$$g_s(-ie)\sum_{spins=s,r,t}\frac{e^{-i(k-p_3-p_4)y}}{(2\pi)^4(2\pi)^3(2\pi)^3}\frac{e^{-i(p_1+p_2-k)x}}{\sqrt{2E_12E_22E_32E_4}}\overline{u}(p_4)^s\Theta(k)\gamma^{\mu}\epsilon_{\mu}(p1)^r u^t(p_2) \tag{3.50}$$

Equation (3.50) requires an implicit integration over the four momentum k is as well as the integrals over the spatial momenta of the outgoing particles p_3 and p_4. The integrals over the two vertices x and y are evaluated using the properties of the Dirac delta function to yield

$$g_s(-ie)\sum_{spins=s,r,t}\frac{1}{(2\pi)^3(2\pi)^3}\frac{(2\pi)^4}{\sqrt{2E_12E_22E_32E_4}}\delta^4(k-p_3-p_4)\delta^4(p_1+p_2-k)\cdot$$
$$\overline{u}(p_4)^s\Theta(k)\gamma^{\mu}\epsilon_{\mu}(p_1)^r u^t(p_2) \tag{3.51}$$

Since momentum is conserved at both vertices, either delta function can be used to evaluate the integral over the four momentum k. After integrating and restoring the integrals over the outgoing particles, Eq. (3.51) can be expressed as

$$g_s(-ie)\sum_{spins=s,r,t}\frac{d^3p_3d^3p_4}{(2\pi)^3(2\pi)^3}\frac{(2\pi)^4}{\sqrt{2E_12E_22E_32E_4}}\delta^4(p_1+p_2-p_3-p_4)\cdot$$
$$\overline{u}(p_4)^s\Theta(k)\gamma^{\mu}\epsilon_{\mu}(p_1)^r u^t(p2) \tag{3.52}$$

The reaction amplitude pertaining to the reaction's dynamics can now be isolated and defined by

$$M = g_s(-ie)\overline{u}(p_4)^s\Theta(k)\gamma^{\mu}\epsilon_{\mu}(p_1)^r u^t(p_2), \tag{3.53}$$

with $k = p_1 + p_2 = p_3 + p_4$. The probability is now defined by $|M|^2$ and the differential cross section using Feynman diagrams can be expressed by

$$d\sigma = \frac{d^3p_3 d^3p_4}{(2\pi)^3(2\pi)^3} \frac{(2\pi)^4}{\sqrt{2E_1 2E_2 2E_3 2E_4}} \delta^4(p_1 + p_2 - p_3 - p_4) \sum_{spins=s,r,t} |M|^2. \tag{3.54}$$

The Dirac delta function in Eq. (3.54) reduces the integration down to two integrals. The differential cross section is then expressed by

$$(\frac{d\sigma}{d\Omega})_{CM} = \frac{1}{(2\pi)^2} \frac{m_p m_\Lambda |\mathbf{p_F}|}{4E_\gamma s} \frac{1}{4} \sum_{all_s pins} |M|^2, \tag{3.55}$$

Chapter 4

The isobar model

Contents

In this study, we look at an effective lagrangian model similar to the one used by Han [31] for the photoproduction of kaons from a proton target and Ramirez [32] for pion photoproduction. The model consists of an effective hadronic lagrangian in the three-level approximation, whose implementation started with the works of Thom [1] and Renard [2] over 30 years ago.

The model makes use of Feynman diagrammatic techniques, discussed in Section (3.2.3), to extract the interaction vertices at first order in perturbation theory, involving the excitation of one resonance.

4.1 Effective hadronic lagrangian

4.1.1 Introduction

In Section 3.1.2 the kinematics of the photoproduction of kaons were discussed as well as energy and momentum conservation at the point of interaction. The actual mechanism for the creation of a virtual particle in the s, u and t-channels and its contributions to the differential cross section are studied by means of an effective lagrangian. The particles involved in the reaction are regarded as structureless fermions and mesons.

In the isobar model, the interaction is defined at two points, one defining the photon vertex $N\gamma R$, and the other, the strong vertex $RK^{+}\Lambda$. The two vertices are connected by a propagator with half integral spin $J \leq \frac{5}{2}$. The spin $\frac{1}{2}$ propagator is given by a relativistic Breit-Wigner form. The higher spin propagators are given by projecting the desired spin from the spin $\frac{1}{2}$ propagator. There has been theoretical work regarding the form of these projection operators, mainly by Napsuiciale [33] and Shi-Zhong [34]. The latter paper works out formulae for an arbitrary $n+\frac{1}{2}$ spin propagator, which is of great interest if one wishes to incorporate any resonance above $J = \frac{5}{2}$. The propagators are derived based on the properties of the Rarita-Schwinger equation [33, 34] and are introduced on shell. It has been shown that off the mass shell, the Rarita-Schwinger form for the propagator for $J = \frac{3}{2}$ does not preserve gauge invariance [15]. An attempt by Mizutani [17] to restore gauge invariance was done by the incorporation of off-shell parameters in the propagator in both the strong and photon vertices in the s-channel for resonances with $J = \frac{3}{2}$. We do not incorporate these additional parameters since our main interest is in the effect of higher spin resonances.

Previous interaction lagrangians incorporated the vertices of nucleon resonances with $J \leq \frac{5}{2}$ and hyperon resonances with $J \leq \frac{3}{2}$. For the current model we extend the analysis to include all available nucleon and hyperon resonances with $J \leq \frac{5}{2}$ in both the s and u-channels respecting the invariance of the interaction lagrangian under the symmetry of point transformations. In our calculation of the amplitudes we make use of a pseudoscalar (PS)

coupling scheme rather than a pseudovector (PV) scheme at the $RK^+\Lambda$ vertex. Bennhold's work over 10 years ago shows no preference between the two schemes when only Born terms are included [35]; but it is possible that the use of the PV scheme would lead to a suppression of the Born couplings when excited state resonances are included, as well as a disagreement between the calculated couplings and the values predicted by SU(3) [36].

In our model, the hadron is treated as a point particle, hence ignoring any form factor associated with the internal structure of the hadron. Han [31] discusses the addition of form factors which have to be inserted in a gauge invariant manner since introduction by hand would spoil gauge invariance. As the photon energy increases, it is essential to introduce form factors. At low energies, it is of more importance to analyze the reaction with the inclusion of a larger set of resonances. The t-channel contribution to the cross-section comes from the exchange of two vector mesons, $K^*(892)$ and $K^1(1270)$ and a kaon born term as described by [15].

The model also incorporates the decay branching ratios for resonances in the s-channel. The decay widths are calculated for six different channels, where in each channel we make use of the vertex corresponding to the lowest possible angular momentum state of the decaying particles. Most of the resonances considered have well established branching ratios and total decay widths given in the Particle Data Book [18] obtained from previous partial wave analyses of experimental data [19]. We make use of these data to obtain the coupling constants for the different decay channels. For states whose existence is not well-established, the widths are incorporated as parameters that will vary with the fit.

The model employed in this study is fully relativistic. Furthermore, four different contributions, where lagrangians based on pion photoproduction [32] are used for the born terms and spin $\frac{1}{2}$ s and u-channel resonances, and lagrangians based on recent theoretical models for kaon photoproduction [31], are used for spin $\frac{3}{2}$ and $\frac{5}{2}$ resonances in the s and u-channels.

4.1.2 Born terms

The born term contributions to the amplitude correspond to the exchange of a proton in the s-channel and a Λ or Σ^0 in the u-channel. A lagrangian similar to the one employed in [32] based on a Yukawa lagrangian, Eq. (4.1), is used to extract the interaction vertices.

$$L = L_{Dirac} + L_{Klein-Gordon} - g_{p\lambda K^+}\overline{u}_\Lambda(\gamma_5\nu_{K^+})u_p \tag{4.1}$$

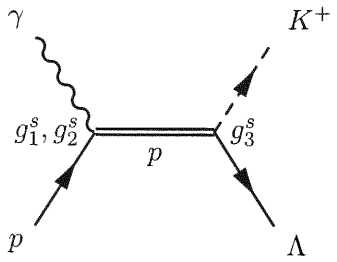

Figure 4.1: s-channel born term contribution to the amplitude for the reaction $\gamma p \rightarrow K^+\Lambda$

The s-channel born term includes two interaction vertices that can be derived from two interaction lagrangians. The photon interaction lagrangian is obtained from the dirac equation and is given by

$$L_{int}^{em} = -e\overline{u}_p\{\gamma^\mu A_\mu + \kappa_p(\partial_\mu A_\nu - \partial_\nu A_\mu)\frac{i}{2(4M_p)}[\gamma^\mu\gamma^\nu]\}u_p, \tag{4.2}$$

where A_μ is the electromagnetic field, κ_p is the anomalous magnetic moment of the proton, and u_p is the dirac spinor of the proton.

The strong vertex $p\Lambda K^+$ can be derived from the interaction lagrangian

$$L_{int}^{strong} = -ig_{pK^+\Lambda}\overline{u}_\Lambda\gamma_5(\nu_{K^+})u_p, \tag{4.3}$$

where $g_{p\Lambda K^+}$ refers to the strong coupling constant, ν_{K^+} to the kaon field, and u_Λ to the dirac spinor of the Λ.

Both vertices can be extracted by expressing the lagrangians above in momentum space and identifying the electromagnetic feld with the polarization four vector ϵ_μ. Using the canonical relationship

$$\partial_\mu = ip_\mu^\gamma \equiv ip_\mu, \tag{4.4}$$

the electromagnetic and strong vertices can be expressed by

$$-e\overline{u}_p\{\gamma^\mu\epsilon_\mu - \kappa_p(p_\mu\epsilon_\nu - p_\nu\epsilon_\mu)\frac{1}{2(4M_p)}[\gamma^\mu\gamma^\nu]\}u_p \tag{4.5}$$

$$-ig_{pK^+\Lambda}\overline{u}_\Lambda\gamma_5 u_p. \tag{4.6}$$

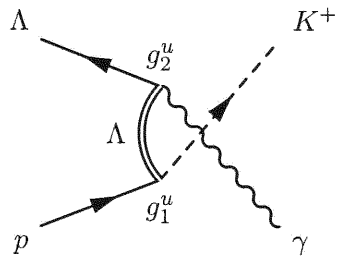

Figure 4.2: u-channel born term contribution to the amplitude for the reaction $\gamma p \rightarrow K^+\Lambda$

In the u-channel, the lagrangian is similarly defined for both vertices but excludes the static electromagnetic interaction term between the photon and the Λ. The only interaction which occurs is the magentic term from the quark's spin distribution. The photon vertex is defined by

$$L_{int}^{em} = -e\overline{u}_\Lambda\{\kappa_\Lambda(\partial_\mu A_\nu - \partial_\nu A_\mu)\frac{i}{2(4M_\Lambda)}[\gamma^\mu\gamma^\nu]\}u_\Lambda. \tag{4.7}$$

Similarly, the strong vertex is defined by

$$L_{int}^{strong} = -ig_{\Lambda K^+\Lambda}\overline{u}_\Lambda\gamma_5(\nu_{K^+})u_p, \tag{4.8}$$

equivalent to the strong vertex for the born term in the s-channel. The electromagnetic and strong vertices in the u-channel can also be expressed in momentum space. This leads to

$$-e\overline{u}_\Lambda\{\kappa_\Lambda(p_\mu\epsilon_\nu - p_\nu\epsilon_\mu)\frac{1}{2(4M_\Lambda)}[\gamma^\mu\gamma^\nu]\}u_\Lambda \tag{4.9}$$

$$-ig_{\Lambda K^+\Lambda}\overline{u}_\Lambda\gamma_5 u_p \tag{4.10}$$

Since both the proton and Λ are ground state particles with total quark angular momentum $L = 0$, they have positive parity, and thus, there are not negative parity contributions to the born terms in the reaction amplitude.

Since the born terms involve the exchange of a proton in the s-channel and a Λ or a Σ^0 in the u-channel, all of which are spin $\frac{1}{2}$ fermions, we make use of the Feynman propagator,

$$\Delta(x-y) = \int \frac{d^4p}{(2\pi)^4}\frac{\gamma^\mu p_\mu + M_{p,\Lambda,\Sigma^0}}{p^2 - M^2_{p,\Lambda,\Sigma^0}}. \tag{4.11}$$

For the s-channel, we can express the amplitude for the reaction as

$$M^s_{born} = ie\cdot g_{pK^+\Lambda}\cdot\overline{u}_\Lambda\gamma_5\frac{\gamma^\mu p_{p,\mu} + M_p}{p_p^2 - M_p^2}\{\gamma^\mu\epsilon_\mu - \kappa_p(p_\mu\epsilon_\nu - p_\nu\epsilon_\mu)\frac{1}{2(4M_p)}[\gamma^\mu\gamma^\nu]\}u_p. \tag{4.12}$$

Similarly, for the u-channel

$$M^u_{born} = -ie\cdot g_{pK^+\Lambda}\cdot\overline{u}_\Lambda\{\kappa_\Lambda(p_\mu\epsilon_\nu - p_\nu\epsilon_\mu)\frac{1}{2(4M_p)}[\gamma^\mu\gamma^\nu]\}\frac{\gamma^\mu p_{\Lambda,\mu} + M_\Lambda}{p_\Lambda^2 - M_\Lambda^2}\gamma_5 u_p, \tag{4.13}$$

where both expressions for M contain an implicit integral over the four momentum of the virtual exchanged particle (propagator).

Since the reaction involves a real photon, the equation above can be re-written using the anticommutation of the gamma matrices,

$$\{\gamma^\mu, \gamma^\nu\} = 2g^{\mu\nu} \tag{4.14}$$

and $\epsilon \cdot p = 0$ as stated in Eq. (3.8) to obtain

$$M^s_{born} = ie \cdot g_{pK^+\Lambda} \cdot \overline{u}_\Lambda \gamma_5 \frac{\gamma^\mu p_{p,\mu} + M_p}{p_p^2 - M_p^2} \{\gamma^\mu \epsilon_\mu - \frac{\kappa_p}{2M_p} \gamma^\nu \epsilon_\nu \gamma^\mu p_\mu\} u_p, \tag{4.15}$$

$$M^u_{born} = -ie \cdot g_{pK^+\Lambda} \cdot \overline{u}_\Lambda \{\frac{\kappa_\Lambda}{2M_\Lambda} \gamma^\nu \epsilon_\nu \gamma^\mu p_\mu\} \frac{\gamma^\mu p_{\Lambda,\mu} + M_\Lambda}{p_\Lambda^2 - M_\Lambda^2} \gamma_5 u_p. \tag{4.16}$$

A similar equation to Eq. (4.16) can be written for the intermediate Σ^0 born term with $M_\Lambda \rightarrow M_{\Sigma^0}$ and $p_\Lambda \rightarrow p_{\Sigma^0}$. Since the parameters in the model involve the products of the couplings at the photon and strong vertices, it is useful to define the following strength products:

$$G^1_{s-born} = e \cdot g_{pK^+\Lambda}, \tag{4.17}$$

$$G^2_{s-born} = e \cdot \kappa_p \cdot g_{pK^+\Lambda}, \tag{4.18}$$

for the s-channel, and

$$G^1_{u-born} = e \cdot \kappa_\Lambda \cdot g_{pK^+\Lambda}, \tag{4.19}$$

for the u-channel.

4.1.3 Spin $\frac{1}{2}$ Resonances

Contributions from resonances with total angular momentum $J = \frac{1}{2}$ correspond to the exchange of nucleon resonances with isospin $I = \frac{1}{2}$ in the s-channel, given in Table (4.1), and hyperon resonances in the u-channel, given in Table (4.2). The hyperon resonances correspond to excited states of the Λ with isospin $I = 0$ and excited states of the Σ^0 with isospin $I = 1$.

s-channel			
Mass (MeV)	Isospin I	J^p	PDG status
$N^*(1440)$	$\frac{1}{2}$	$\frac{1}{2}^+$	****
$N^*(1710)$	$\frac{1}{2}$	$\frac{1}{2}^+$	***
$N^*(1535)$	$\frac{1}{2}$	$\frac{1}{2}^-$	****
$N^*(1650)$	$\frac{1}{2}$	$\frac{1}{2}^-$	***

Table 4.1: Nucleon resonances with $J = \frac{1}{2}$

u-channel			
Mass (MeV)	Isospin I	J^p	PDG status
$\Lambda^*(1600)$	0	$\frac{1}{2}^+$	***
$\Lambda^*(1810)$	0	$\frac{1}{2}^+$	***
$\Lambda^*(1405)$	0	$\frac{1}{2}^-$	****
$\Lambda^*(1670)$	0	$\frac{1}{2}^-$	****
$\Sigma^*(1660)$	1	$\frac{1}{2}^+$	***
$\Sigma^*(1750)$	1	$\frac{1}{2}^-$	***

Table 4.2: Hyperon resonances with $J = \frac{1}{2}$

As discussed in Section (2.2), resonances with total angular momentum $J = \frac{1}{2}$ in both the s and u-channels appear with either positive or negative parities corresponding to the symmetry of the spin and angular wavefunctions arising from the relative excitation of the composite quarks. The parities of these excited states are also shown in Tables (4.1) and (4.2). Both the strong and electromagnetic vertices depend on the parity of the resonance exchanged.

As with the Born term, the lagrangian describing the s-channel resonance contributions consist of two vertices. For positive parity states, the photon interaction lagrangian is similar to the magnetic interaction of a ground state fermion with the electromagnetic field. The $J = \frac{1}{2}$ nucleon resonances arise from transitions of the proton into an excited state and therefore electromagentic currents contribute to the coupling only through the magnetic moments. The interaction piece of the lagrangian at the photon vertex can expressed by

$$L_s^{em} = -e\overline{u}_{N^*}\{\kappa_{N^*}(\partial_\mu A_\nu - \partial_\nu A_\mu)\frac{i}{2(4M_p)}[\gamma^\mu\gamma^\nu]\}u_p. \tag{4.20}$$

Where κ_{N^*} corresponds to the resonance's transition magnetic moment and $\overline{u}_{N^*}$ to its dirac spinor. Negative parity states can be obtained by multiplying the resonance spinor by γ_5:

$$L_s^{em} = -e\overline{u}_{N^*}\gamma_5\{\kappa_{N^*}(\partial_\mu A_\nu - \partial_\nu A_\mu)\frac{i}{2(4M_p)}[\gamma^\mu\gamma^\nu]\}u_p. \tag{4.21}$$

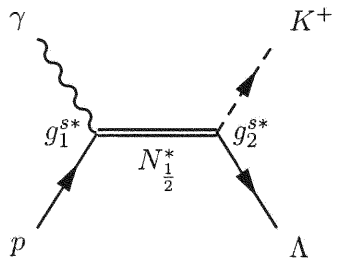

Figure 4.3: s-channel resonance contribution to the amplitude for the reaction $\gamma p \rightarrow K^+\Lambda$

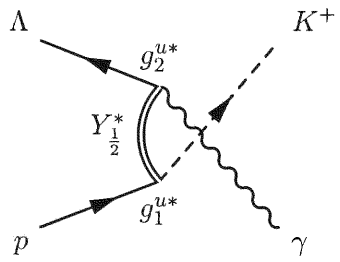

Figure 4.4: u-channel resonance contribution to the amplitude for the reaction $\gamma p \rightarrow K^+\Lambda$

The strong interaction lagrangian can be written in exactly the same way as for the born term but with the appropriate resonance coupling. For positive parity resonances it is given by

$$L_s^{strong} = -ig_{N^*K^+\Lambda}\overline{u}_\Lambda\gamma_5(\nu_{K^+})u_{N^*}, \tag{4.22}$$

and by

$$L_s^{strong} = -ig_{N^*K^+\Lambda}\overline{u}_\Lambda\gamma_5(\nu_{K^+})\gamma_5 u_{N^*} \tag{4.23}$$

for the negative parity states.

The u-channel interaction lagrangian for the $J = \frac{1}{2}$ hyperon resonances is defined to be identical to the u-channel born term, where to first order, only electromagnetic field currents contribute at the photon vertex. Defining the transition magnetic moment by $\kappa_{\Lambda^*,\Sigma^*}$, the electromagnetic and strong interaction lagrangians for positive parity u-channel resonances can be expressed by

$$\begin{aligned} L_u^{em} &= -e\overline{u}_\Lambda\{\kappa_{Y^*}(\partial_\mu A_\nu - \partial_\nu A_\mu)\frac{i}{2(4M_{Y^*})}[\gamma^\mu\gamma^\nu]\}u_{Y^*}, \\ L_u^{strong} &= -ig_{Y^*K^+p}u_{Y^*}\gamma_5(\nu_{K^+})u_p, \end{aligned} \tag{4.24}$$

and by

$$\begin{aligned} L_u^{em} &= -eu_\Lambda\gamma_5\{\kappa_{Y^*}(\partial_\mu A_\nu - \partial_\nu A_\mu)\frac{i}{2(4M_\Lambda)}[\gamma^\mu\gamma^\nu]\}u_{Y^*}, \\ L_u^{strong} &= -ig_{Y^*K^+p}u_{Y^*}\gamma_5(\nu_{K^+})\gamma_5 u_p, \end{aligned} \tag{4.25}$$

for negative parity resonances. Y^* has been used to denote either contribution from a Λ^* or a Σ^* resonance.

The propagator used for the $J = \frac{1}{2}$ resonances is also given by a relativistic Breit-Wigner propagator:

$$\Delta_{s,u}(x-y) = \int \frac{d^4p}{(2\pi)^4} D_{s,u}(p)(\gamma^\mu p_\mu + M_{s,u}), \tag{4.26}$$

where

$$D_s(p) = (p^2 - M_{N^*}^2 + iM_{N^*}\Gamma_{N^*})^{-1} \tag{4.27}$$

in the s-channel, and

$$D_u(p) = (p^2 - M_{Y^*}^2)^{-1} \tag{4.28}$$

in the u-channel. Note that a width Γ has not been incorporated in the u-channel propagator since the value of u, the four momentum squared transferred to the resonance, has a negative value, and therefore the resonance cannot decay. An overall discussion of the widths, as well as the dynamical model used to calculate resonance decay amplitudes, will be given in Section (4.3). The above lagrangians, expressed in momentum space as in Section (4.1.2), and the propagator given in Eq. (4.26) can be used to derive the amplitudes for resonances with $J = \frac{1}{2}$ in both the s and u-channels. The positive parity amplitudes are given by

$$\begin{aligned} M^s_{\frac{1}{2}+} &= -ie \cdot g_{N^*K^+\Lambda} D_s(p_{N^*}) \cdot \overline{u}_\Lambda \gamma_5 (\gamma^\mu p_{N^*,\mu} + M_{N^*}) \{ \frac{\kappa_{N^*}}{2M_p} \gamma^\nu \epsilon_\nu \gamma^\mu p_\mu \} u_p, \\ M^u_{\frac{1}{2}+} &= -ie \cdot g_{Y^*K^+p} D_u(p_{Y^*}) \cdot \overline{u}_\Lambda \{ \frac{\kappa_{Y^*}}{2M_\Lambda} \gamma^\nu \epsilon_\nu \gamma^\mu p_\mu \} (\gamma^\mu p_{Y^*,\mu} + M_{Y^*}) \gamma_5 u_p, \end{aligned} \tag{4.29}$$

and making use of the identity $(\gamma_5^2) = \mathbf{1}$, the negative parity states can be expressed by

$$\begin{aligned} M^s_{\frac{1}{2}-} &= -ie \cdot g_{N^*K^+\Lambda} D_s(p_{N^*}) \cdot \overline{u}_\Lambda (\gamma^\mu p_{N^*,\mu} + M_{N^*}) \{ \frac{\kappa_{N^*}}{2M_p} \gamma^\nu \epsilon_\nu \gamma^\mu p_\mu \} \gamma_5 u_p, \\ M^u_{\frac{1}{2}-} &= -ie \cdot g_{Y^*K^+p} D_u(p_{Y^*}) \cdot \overline{u}_\Lambda \gamma_5 \{ \frac{\kappa_\Lambda}{2M_{Y^*}} \gamma^\nu \epsilon_\nu \gamma^\mu p_\mu \} (\gamma^\mu p_{Y^*,\mu} + M_{Y^*}) u_p, \end{aligned} \tag{4.30}$$

The coupling strength products are defined by

$$F_s = e \cdot \kappa_{N^*} \cdot g_{N^*K^+\Lambda} \tag{4.31}$$

for nucleon resonances, and

$$F_u = e \cdot \kappa_{\Lambda \to Y^*} \cdot g_{Y^*K^+p} \tag{4.32}$$

for hyperon resonances, where $\kappa_{\Lambda \to Y^*}$ indicates the transition magnetic moment from a ground state Λ to an excited Λ^* or Σ^* excited state.

4.1.4 Spin $\frac{3}{2}$ Resonances

The treatment of higher spin resonances is of great relevance if one wishes to devise a model at the hadronic level that can accurately describe recent experimental data. The treatment of higher half-integral spin resonances began with the works of Pauli and Fierz [37] and was later studied by Rarita and Schwinger [38] in what is known today as the Rarita-Schwinger framework. The latter approach to spin $\frac{3}{2}$ particles has been used extensively in previous isobar models [14, 15, 17, 31, 32]. Within the Rarita-Schwinger framework one describes a spin $\frac{3}{2}$ particle as a Lorentz tensor of rank one with dirac spinor components

$$\psi^{\alpha}_{\mu}(x), \tag{4.33}$$

and imposes the following conditions on the wavefunction:

$$(\gamma_\nu p^\nu - m)\psi^\mu = 0, \tag{4.34}$$

$$\gamma_\mu \psi^\mu = 0, \tag{4.35}$$

$$p_\mu \psi^\mu = 0. \tag{4.36}$$

The conditions imposed on the wavefunction are generally used to eliminate the spin $\frac{1}{2}$ components of a spin $\frac{3}{2}$ free particle; they do not always hold when interactions are present, as shown in [39].

Given that lagrangians for this particles may not be unique, Eq. (4.35) ensures that one possible form of a free lagrangian,

$$\overline{\psi}_\mu(\gamma^\lambda\partial_\lambda + m)\psi^\mu - \frac{1}{3}\overline{\psi}_\mu(\gamma_\mu\partial_\nu + \gamma_\nu\partial_\mu)\psi^\nu + \frac{1}{3}\overline{\psi}_\mu\gamma^\mu(\gamma^\lambda\partial_\lambda - m)\gamma^\nu\psi_\nu, \tag{4.37}$$

as given by [38], remains invariant under point transformations of the form

$$\psi^\mu \rightarrow \psi'^\mu = \psi^\mu + \gamma^\mu\gamma^\nu\psi_\nu. \tag{4.38}$$

Since the total lagrangian must also be invariant under the point transformation, Eq. (4.37) constrains the form of an interaction lagrangian, which is highly relevant for this study. The form of the free lagrangian and all of its theoretical aspects also affect the form of the propagator for a higher spin resonance, but this will not be investigated here. However, the form of the propagator for resonances with total angular momentum $\frac{3}{2}$ has been studied extensively, and one particular expression has been derived by Zhong [34] based on the Rarita-Schwinger framework. For the $J = \frac{3}{2}$ case, the propagator is modified to include the total width for resonances in the s-channel. The propagator is given by

$$P^{\frac{3}{2}}_{\mu\nu} = \frac{\not{p}_R + M_R}{(p_R^2 - M_R^2 + iM_R\Gamma_R)}P_{\mu\nu}, \tag{4.39}$$

where $\Gamma_R = 0$ for resonances in the u-channel. The projection operator $P_{\mu\nu}$ is given by

$$P_{\mu\nu} = g_{\mu\nu} - \frac{1}{2}\gamma_\mu\gamma_\nu + \frac{1}{3}\frac{p_{R,\mu}\gamma_\nu - p_{R,\nu}\gamma_\mu}{M_R} - \frac{2}{3}\frac{p_{R,\mu}p_{R,\nu}}{M_R^2}. \tag{4.40}$$

As discussed by Benmerrouche [40], Eq. (4.39) has the correct inverse but off-the-mass-shell parameters must be added to the interaction vertices to account for the spin $\frac{1}{2}$ components of the wavefunction, which contribute to the propagation of the massive spin $\frac{3}{2}$ resonance when it is off its mass shell. In the present model, off-shell parameters are not implemented since more emphasis is given to the inclusion of particles with both greater angular momentum and greater mass. Furthermore, calculations performed by Mizutani [17],

have shown that these parameters have a relatively modest effect on observables. The most general lagrangian between spin $\frac{1}{2}$ and $\frac{3}{2}$ particles that excludes off-shell parameters is discussed by Han [31] and given by

$$L_{int} = \overline{u}_1^{\mu} \Theta_{\mu\nu} C^{\nu} u_2. \tag{4.41}$$

The form of C^{ν} dependes on whether the interaction is at the photon or strong vertex. The lagrangian will be invariant under Eq. (4.38) provided that $\gamma^{\mu}\Theta_{\mu\nu} = 0$. Thus one can define $\Theta_{\mu\nu}$ as

$$\Theta\mu\nu = g_{\mu\nu} - \frac{1}{4}\gamma_{\mu}\gamma\nu. \tag{4.42}$$

s-channel			
Mass (MeV)	Isospin I	J^p	PDG status
$N^*(1720)$	$\frac{1}{2}$	$\frac{3}{2}^+$	****
$N^*(1520)$	$\frac{1}{2}$	$\frac{3}{2}^-$	****
$N^*(1700)$	$\frac{1}{2}$	$\frac{3}{2}^-$	***

Table 4.3: Nucleon resonances with $J = \frac{3}{2}$

u-channel			
Mass (MeV)	Isospin I	J^p	PDG status
$\Lambda^*(1890)$	0	$\frac{3}{2}^+$	****
$\Lambda^*(1520)$	0	$\frac{3}{2}^-$	****
$\Lambda^*(1690)$	0	$\frac{3}{2}^-$	****
$\Sigma^*(1385)$	1	$\frac{3}{2}^+$	****
$\Sigma^*(1670)$	1	$\frac{3}{2}^-$	****
$\Sigma^*(1940)$	1	$\frac{3}{2}^-$	***

Table 4.4: Hyperon resonances with $J = \frac{3}{2}$

The $J = \frac{3}{2}$ resonances considered in this study are given in Table (4.3) for the s-channel, and Table (4.4) for the u-channel. In the s-channel, the interaction lagrangian at the photon vertex can be expressed by

$$L_s^{em} = -\frac{ie}{2M_p}\overline{u}^{\mu}_{N^*}\Theta_{\mu\nu}[g_1^s\gamma_\lambda + i\frac{g_2^s}{2M_p}\partial^\lambda]\gamma_5 u_p(\partial^\nu A^\lambda - \partial^\lambda A^\nu) \tag{4.43}$$

This form of the lagrangian includes the interaction due to electromagnetic currents with two possible Lorentz invariant interaction forms. In the u-channel, the electromagnetic interaction takes place between a hyperon and its excited state and can be expressed by the hermitian conjugate of Eq. (4.43) with the appropriate spinors,

$$L_u^{em} = -\frac{ie}{2M_\Lambda}(\partial^\nu A^\lambda - \partial^\lambda A^\nu)u_\Lambda\gamma_5[g_1^u\gamma_\lambda + i\frac{g_2^u}{2M_\Lambda}\partial^\lambda]\Theta_{\nu\mu}u^{\mu}_{Y^*}. \tag{4.44}$$

The strong interaction term in the lagrangian in the s-channel is given by

$$L_s^{strong} = \frac{g_3^s}{M_\pi}u_\Lambda(\partial^\mu\nu^\dagger_{K^+})\Theta_{\mu\nu}u^{\nu}_{N^*}, \tag{4.45}$$

where g_3^s represents the strong coupling constant, and the factor of $(M_\pi)^{-1}$ is added to make the coupling constant dimensionless. Similarly, the strong interaction lagrangian in the u-channel can be expressed by

$$L_u^{strong} = \frac{g_3^u}{M_\pi}\overline{u}^{\mu}_{Y^*}\Theta_{\mu\nu}(\partial^\nu\nu_{K^+})u_p. \tag{4.46}$$

The vertices for both interactions can be constructed, as in the spin $\frac{1}{2}$ case, in momentum space. Using Eq. (4.39) for the propagators and $p_\gamma \cdot p_\gamma = 0$ and $p_\gamma \cdot \epsilon = 0$ for real photons, the amplitude can be expressed by

$$\begin{aligned} M^s_{\frac{3}{2}+} &= -\frac{g_3^s}{M_\pi} D_s(p_{N^*}) \overline{u}_\Lambda (\not{p}_{N^*} + M_{N^*}) p_K^\mu P_{\mu\nu} \{ \frac{g_1^s}{M_p} (\epsilon^\nu \not{p}_\gamma - p_\gamma^\nu \not{\epsilon}) \\ &+ \frac{g_2^s}{(2M_p)^2} (\epsilon \cdot p_p p_\gamma^\nu - p_\gamma \cdot p_p \epsilon^\nu) \} \gamma_5 u_p \end{aligned} \tag{4.47}$$

in the s-channel, and

$$\begin{aligned} M^u_{\frac{3}{2}+} &= -\frac{g_3^u}{M_\pi} D_u(p_{Y^*}) \overline{u}_\Lambda \gamma_5 (\not{p}_{Y^*} + M_{Y^*}) \{ \frac{g_1^u}{M_\Lambda} (\epsilon^\mu \not{p}_\gamma - p_\gamma^\mu \not{\epsilon}) \\ &+ \frac{g_2^u}{(2M_\Lambda)^2} (\epsilon \cdot p_\Lambda p_\gamma^\nu - p_\gamma \cdot p_\Lambda \epsilon^\nu) \} P^{\mu\nu} p_K^\nu u_p \end{aligned} \tag{4.48}$$

in the u-channel for positive parity resonances. The notation $\not{p} = \gamma^\mu p_\mu$ has been used to simplify the expressions. For negative parity excited states, the following substitutions are made for for the resonance spinors in Eqs. (4.47) and (4.48):

$$\begin{aligned} u_{N^*,Y*} &\rightarrow \gamma_5 u_{N^*,Y*}, \\ \overline{u}_{N^*,Y*} &\rightarrow \overline{u}_{N^*,Y*} \gamma_5. \end{aligned} \tag{4.49}$$

These definitions yield the following amplitudes for negative parity states:

$$\begin{aligned} M^s_{\frac{3}{2}-} &= -\frac{g_3^s}{M_\pi} D_s(p_{N^*}) \overline{u}_\Lambda \gamma_5 (\not{p}_{N^*} + M_{N^*}) p_K^\mu P_{\mu\nu} \{ \frac{g_1^s}{M_p} (\epsilon^\nu \not{p}_\gamma - p_\gamma^\nu \not{\epsilon}) \\ &+ \frac{g_2^s}{(2M_p)^2} (\epsilon \cdot p_p p_\gamma^\nu - p_\gamma \cdot p_p \epsilon^\nu) \} u_p, \end{aligned} \tag{4.50}$$

$$\begin{aligned} M^u_{\frac{3}{2}-} &= -\frac{g_3^u}{M_\pi} D_u(p_{Y^*}) \overline{u}_\Lambda (\not{p}_{Y^*} + M_{Y^*}) \{ \frac{g_1^u}{M_\Lambda} (\epsilon^\mu \not{p}_\gamma - p_\gamma^\mu \not{\epsilon}) \\ &+ \frac{g_2^u}{(2M_\Lambda)^2} (\epsilon \cdot p_\Lambda p_\gamma^\nu - p_\gamma \cdot p_\Lambda \epsilon^\nu) \} P^{\mu\nu} p_K^\nu \gamma_5 u_p. \end{aligned} \tag{4.51}$$

Making use of the definitions,

$$F_1(p_{N^*,Y^*}) = \frac{eg_3g_1D(p_{N^*,Y^*})}{2M_{p,\Lambda}M_\pi},$$
$$F_2(p_{N^*,Y^*}) = \frac{eg_3g_2D(p_{N^*,Y^*})}{(2M_{p,\Lambda})^2M_\pi}, \tag{4.52}$$

and carrying out the contractions between the strong and photon vertices using the projection operator in Eq. (4.40) yields

$$\begin{aligned} M^s_{\frac{3}{2}+} &= -i\overline{u}_\Lambda(\not{p}_{N^*} + M_{N^*})[F_1(p_{N^*})\{(\not{R} + \frac{2}{3}\not{q}\not{p}_\gamma\not{\epsilon} \\ &- \frac{2}{3M_{N^*}}(p_K \cdot p_{N^*}\not{p}_\gamma\not{\epsilon} - \frac{1}{3M_{N^*}}\not{p}_K\not{t}\} \\ &+ F_2(p_{N^*})\{q \cdot t - \frac{1}{3}\not{p}_K\not{t} + \frac{1}{3M_{N^*}}p_{N^*} \cdot p_K\not{t}\}]\gamma_5 u_p \end{aligned} \tag{4.53}$$

for positive parity nucleon resonances, and

$$\begin{aligned} M^s_{\frac{3}{2}-} &= -i\overline{u}_\Lambda\gamma_5(\not{p}_{N^*} + M_{N^*})[F_1(p_{N^*})\{(\not{R} + \frac{2}{3}\not{q}\not{p}_\gamma\not{\epsilon} \\ &- \frac{2}{3M_{N^*}}(p_K \cdot p_{N^*}\not{p}_\gamma\not{\epsilon} - \frac{1}{3M_{N^*}}\not{p}_K\not{t}\} \\ &+ F_2(p_{N^*})\{q \cdot t - \frac{1}{3}\not{p}_K\not{t} + \frac{1}{3M_{N^*}}p_{N^*} \cdot p_K\not{t}\}]u_p \end{aligned} \tag{4.54}$$

for negative parity resonances, where

$$\begin{aligned} q^\mu &= p^\mu_K - p^\mu_\gamma, \\ t^\mu &= (\epsilon \cdot p_p)p^\mu_\gamma - (p_\gamma \cdot p_p)\epsilon^\mu, \\ R^\mu &= (q \cdot \epsilon)p^\mu_\gamma - (q \cdot p_\gamma)\epsilon^\mu - \frac{2}{3M_{(N^*)^2}}(p_K \cdot p_{N^*})t^\mu. \end{aligned} \tag{4.55}$$

Similarly, in the u-channel, the amplitudes can be expressed by

$$\begin{aligned} M^u_{\frac{3}{2}+} &= -\overline{u}_\Lambda \gamma_5 [\not{p}_{Y^*} \{F_2(p_{Y^*}) q\cdot t - \not{W} - \frac{2}{3M_{Y^*}} F_1(p_{Y^*}) p_K \cdot p_{Y^*} \not{\epsilon} \not{p}_\gamma \\ &- \frac{1}{3}\alpha \not{t} \not{p}_K - \frac{2}{3} F_1(p_{Y^*}) \not{\epsilon} \not{p}_\gamma \not{q}\} + M_{Y^*} \{\beta_1 q\cdot t + \not{Y} \\ &+ \frac{2}{3M_{Y^*}} p_K \cdot p_{Y^*} \not{\epsilon} \not{p}_\gamma + \beta_2 \not{t} \not{p}_K + \frac{2}{3} F_1(p_{Y^*}) \not{\epsilon} \not{p}_\gamma \not{q}\}] u_p, \end{aligned} \tag{4.56}$$

$$\begin{aligned} M^u_{\frac{3}{2}-} &= -\overline{u}_\Lambda [\not{p}_{Y^*} \{F_2(p_{Y^*}) q\cdot t - \not{W} - \frac{2}{3M_{Y^*}} F_1(p_{Y^*}) p_K \cdot p_{Y^*} \not{\epsilon} \not{p}_\gamma \\ &- \frac{1}{3}\alpha \not{t} \not{p}_K - \frac{2}{3} F_1(p_{Y^*}) \not{\epsilon} \not{p}_\gamma \not{q}\} + M_{Y^*} \{\beta_1 q\cdot t + \not{Y} \\ &+ \frac{2}{3M_{Y^*}} p_K \cdot p_{Y^*} \not{\epsilon} \not{p}_\gamma + \beta_2 \not{t} \not{p}_K + \frac{2}{3} F_1(p_{Y^*}) \not{\epsilon} \not{p}_\gamma \not{q}\}] \gamma_5 u_p, \end{aligned} \tag{4.57}$$

for positive and negative parity resonances respectively, where

$$\begin{aligned} t^\mu &= t^\mu_{s-channel}(M_p \to M_\Lambda), \\ R^\mu &= R^\mu_{s-channel}(M_{N^*} \to M_{Y^*}), \\ Y^\mu &= F_1(p_{Y^*}) R^\mu + \frac{1}{3M_{Y^*}} (\frac{2F_1(p_{Y^*})}{M_{Y^*}} - F_2(p_{Y^*})) p_K \cdot p_{Y^*} t^\mu, \\ W^\mu &= F_1(p_{Y^*}) R^\mu + \frac{1}{3M_{Y^*}} p_K \cdot p_{Y^*} t^\mu, \\ \alpha &= \frac{F_1(p_{Y^*})}{M_{Y^*}} + F_2(p_{Y^*}), \\ \beta_1 &= F_2(p_{Y^*}) - \frac{2F_1(p_{Y^*})}{M_{Y^*}}, \\ \beta_2 &= \frac{F_1(p_{Y^*})}{M_{Y^*}} + \frac{F_2(p_{Y^*})}{3}. \end{aligned} \tag{4.58}$$

Unlike spin $\frac{1}{2}$ resonances, higher angular momentum states involve two electromagnetic couplings. Since the parameters in the model involve coupling products as free parameters, the following dimensionless coupling products are defined in the s-channel by

$$\begin{aligned} G^s_1 &= g^s_1 \cdot g^s_3, \\ G^s_2 &= g^s_2 \cdot g^s_3. \end{aligned} \tag{4.59}$$

Similarly, in the u-channel, the coupling products can be expressed by

$$\begin{aligned} G_1^u &= g_1^u \cdot g_3^u, \\ G_2^u &= g_2^u \cdot g_3^u. \end{aligned} \tag{4.60}$$

4.1.5 Spin $\frac{5}{2}$ Resonances

Theoretical studies regarding the interaction of spin $\frac{5}{2}$ particles have become increasingly interesting in light of new and improved data on the photoproduction and electroproduction of strange particles, which suggests that there is a wide spectrum of higher angular momentum states that contribute to the reactions' amplitude. Furthermore, a number of these particles have attained three or four star status in the latest version of the PDG tables [18]. There has been wide theoretical discussion on wavefunctions, propagators, and interaction theories that pertains to these particles, which involves relativistic wave equations, extensions obtained from the Rarita-Schwinger framework discussed in the previous section. One work in particular, is the recent work by Nierdele [41]. In this framework, the spin $\frac{5}{2}$ wavefunction for a massive particle can be expressed by the direct product of a second rank Lorentz tensor with a Dirac spinor with components α,

$$\psi^{\alpha}_{\mu\nu}(x) \tag{4.61}$$

which satisfies the Dirac equation

$$(\gamma_\lambda p^\lambda - m)\psi^{\mu\nu} = 0 \tag{4.62}$$

and the condition

$$\gamma_\mu \gamma_\nu \psi^{\mu\nu} = 0 \tag{4.63}$$

for each of their Lorentz indices. Again, these conditions eliminate the smaller spin components of the wavefunction in the free lagrangian that describes the propagation of a spin $\frac{5}{2}$ particle, but they may not hold under the presence of interactions.

Half integral spin propagators are constructed in analogy to the Rarita-Schwinger propagators for a particle with half integral spin $\frac{3}{2}$; in particular, an expression for porpagators with arbitrary intergal spin $n+\frac{1}{2}$ has been derived by Zhong [34]. In the present study, the form of the spin $\frac{5}{2}$ propagator has been modified and introduced on shell to be consistent with the Benmerrouche [40] and Mizutani [17] treatment of the spin $\frac{3}{2}$ projection operator, which take into consideration the lower spin components that contribute to the propagation when the particle is off its mass shell. The propagator used can be expressed by

$$P^{\frac{5}{2}}_{\mu\nu\lambda\sigma} = \frac{\not{p}_R + M_R}{10(p_R^2 - M_R^2 + iM_R\Gamma_R)} P_{\mu\nu\lambda\sigma}, \tag{4.64}$$

where

$$\begin{aligned} P_{\mu\nu\lambda\sigma} &= 5P_{\mu\lambda}P_{\nu\sigma} - 2P_{\mu\nu}P_{\lambda\sigma} + 5P_{\mu\sigma}P_{\nu\lambda} + P_{\mu\rho}\gamma^\rho\gamma^\xi P_{\xi\lambda}P_{\nu\sigma} + P_{\nu\rho}\gamma^\rho\gamma^\xi P_{\xi\sigma}P_{\mu\lambda} \\ &+ P_{\mu\rho}\gamma^\rho\gamma^\xi P_{\xi\sigma}P_{\nu\lambda} + P_{\nu\rho}\gamma^\rho\gamma^\xi P_{\xi\lambda}P_{\mu\sigma}, \end{aligned} \tag{4.65}$$

and where

$$P_{\mu\nu} = g_{\mu\nu} - \frac{P_{R,\mu}P_{R,\nu}}{(M_R)^2} \tag{4.66}$$

is the desired form of the on-shell projection operator. Again the width Γ_R is set to zero in the u-channel.

The $J = \frac{5}{2}$ resonances considered in this study are given in Table (4.5) in the s-channel and Table (4.6) in the u-channel.

s-channel			
Mass (MeV)	Isospin I	J^p	PDG status
$N^*(1680)$	$\frac{1}{2}$	5^+_2	****
$N^*(1675)$	$\frac{1}{2}$	5^-_2	****

Table 4.5: Nucleon resonances with $J = \frac{5}{2}$

u-channel			
Mass (MeV)	Isospin I	J^p	PDG status
$\Lambda^*(1820)$	0	$\frac{5}{2}^+$	****
$\Lambda^*(2110)$	0	$\frac{5}{2}^+$	***
$\Lambda^*(1830)$	0	$\frac{5}{2}^-$	****
$\Sigma^*(1915)$	1	$\frac{5}{2}^+$	****
$\Sigma^*(1775)$	1	$\frac{5}{2}^-$	****

Table 4.6: Hyperon resonances with $J = \frac{5}{2}$

The lagrangian for the interaction between spin $\frac{1}{2}$ and $\frac{5}{2}$ particles, which does not contain off-shell parameters, has been discussed by Han [31] for the s-channel without explicit derivation of the vertices. The s-channel lagrangian is given by

$$L_s^{em} = \frac{e}{(2M_pM_\pi)} u^{\mu\nu}_{N^*} \Theta_{\mu\alpha}[g_1^s\gamma_\lambda + \frac{ig_2^s}{2M_p}\partial_\lambda]u_p\partial_\nu(\partial^\alpha A^\lambda - \partial^\lambda A^\alpha) \tag{4.67}$$

The expression for the u-channel can be obtained from the hermitian conjugate of Eq. (4.67) for positive parity resonances

$$L_u^{em} = \frac{e}{(2M_\Lambda M_\pi)}\partial_\nu(\partial^\alpha A^\lambda - \partial^\lambda A^\alpha)\overline{u}_\Lambda[g_1^u\bar{\gamma}_\lambda + \frac{ig_2^u}{2M_\Lambda}\bar{\partial}_\lambda]\Theta_{\alpha\mu}u^{\mu\nu}_{Y^*}. \tag{4.68}$$

The operators $\bar{\gamma}_\lambda$ and $\bar{\partial}_\lambda$ indicate that the operation is on the outgoing Λ spinor, $\bar{u}_\Lambda$. The strong interaction terms are expressed by

$$L_s^{strong} = i\frac{g_3^s}{(M_\pi)^2}\overline{u}_\Lambda\gamma_5\Theta_{\alpha\mu}u^{\mu\nu}_{N^*}(\partial^\nu\partial^\alpha\nu_K) \tag{4.69}$$

in the s-channel, and in the u-channel by

$$L_u^{strong} = i\frac{g_3^s}{(M_\pi)^2}\overline{u}^{\mu\nu}_{Y^*}\gamma_5\Theta_{\mu\alpha}u_p(\partial^\alpha\partial^\nu\nu_K) \tag{4.70}$$

The lagrangian for negative parity resonances are obtained by transforming the resonance spinors as in Eq. (4.49). The form of the interaction tensor is given by $\Theta_{\mu\nu} = g_{\mu\nu}$. This

form guarantees the point invariance of both the free and interaction lagrangians of a spin $\frac{5}{2}$ particle and may not be unique. From the above definitions of the lagrangian densities at both vertices in both the s and u-channels, and the form of the propagator given by Eq. (4.64), the vertices can be derived in momentum space. For positive parity nucleon resonances, the amplitude is given by

$$\begin{aligned} M^s_{\frac{5}{2}+} &= -i\frac{eg_3^s}{(M_\pi)^3}\frac{D_s(p_{N^*})}{10}\overline{u}_\Lambda\gamma_5 p_K^\mu p_K^\nu(\not{p}_{N^*}+M_{N^*})P_{\mu\nu\lambda\sigma}\{\frac{g_1^s}{2M_p}(\epsilon^\lambda p_\gamma^\sigma\not{p}_\gamma - p_\gamma^\lambda p_\gamma^\sigma\not{\epsilon}) \\ &+ \frac{g_2^s}{(2M_p)^2}(\epsilon\cdot p_p p_\gamma^\lambda p_\gamma^\sigma - p_\gamma\cdot p_p\epsilon^\lambda p_\gamma^\sigma)\}u_p, \end{aligned} \tag{4.71}$$

and for negative parity nucleon resonances, given by

$$\begin{aligned} M^s_{\frac{5}{2}-} &= -i\frac{eg_3^s}{(M_\pi)^3}\frac{D_s(p_{N^*})}{10}\overline{u}_\Lambda p_K^\mu p_K^\nu(\not{p}_{N^*}+M_{N^*})P_{\mu\nu\lambda\sigma}\{\frac{g_1^s}{2M_p}(\epsilon^\lambda p_\gamma^\sigma\not{p}_\gamma - p_\gamma^\lambda p_\gamma^\sigma\not{\epsilon}) \\ &+ \frac{g_2^s}{(2M_p)^2}(\epsilon\cdot p_p p_\gamma^\lambda p_\gamma^\sigma - p_\gamma\cdot p_p\epsilon^\lambda p_\gamma^\sigma)\}\gamma_5 u_p. \end{aligned} \tag{4.72}$$

After contracting both vertices, the amplitudes can be expressed by

$$\begin{aligned} M^s_{\frac{5}{2}+} &= \overline{u}_\Lambda\gamma_5(\not{p}_{N^*}+M_{N^*})\{F_1[10a-2b+2\not{p}_K\not{I}+2\not{p}_{N^*}\not{K}]\not{p}_\gamma \\ &- F_1[10a'-2b'+4\not{p}_K\not{J}+4\not{p}_{N^*}\not{N}]\not{\epsilon} \\ &+ F_2(\epsilon\cdot p_p)[10a'-2b'+4\not{p}_K\not{J}+4\not{p}_{N^*}\not{N}]\not{\epsilon} \\ &- F_2(p_\gamma\cdot p_p)[10a-2b+2\not{p}_K\not{I}+2\not{p}_{N^*}\not{K}]\}u_p, \end{aligned} \tag{4.73}$$

$$\begin{aligned} M^s_{\frac{5}{2}-} &= \overline{u}_\Lambda(\not{p}_{N^*}+M_{N^*})\{F_1[10a-2b+2\not{p}_K\not{I}+2\not{p}_{N^*}\not{K}]\not{p}_\gamma \\ &- F_1[10a'-2b'+4\not{p}_K\not{J}+4\not{p}_{N^*}\not{N}]\not{\epsilon} \\ &+ F_2(\epsilon\cdot p_p)[10a'-2b'+4\not{p}_K\not{J}+4\not{p}_{N^*}\not{N}]\not{\epsilon} \\ &- F_2(p_\gamma\cdot p_p)[10a-2b+2\not{p}_K\not{I}+2\not{p}_{N^*}\not{K}]\}\gamma_5 u_p. \end{aligned} \tag{4.74}$$

The four vectors are I^μ, J^μ, K^μ, and N^μ are linear combinations of ϵ^μ, p^μ_γ, and $p^\mu_{N^*}$ and are explicitly given in Appendix A along with the expressions for the Lorentz scalars a, a', b, and b'. F_1 and F_2 are defined as follows:

$$\begin{aligned} F_1 \equiv F_1(p_{N^*}) &= \frac{e g_1^s g_3^s D_s(p_{N^*})}{20 M_p M_\pi^3}, \\ F_2 \equiv F_2(p_{N^*}) &= \frac{e g_2^s g_3^s D_s(p_{N^*})}{40 M_p^2 M_\pi^3}. \end{aligned} \tag{4.75}$$

The u-channel contribution can be expressed by

$$\begin{aligned} M^u_{\frac{5}{2}+} &= -i\frac{e g_3^u}{(M_\pi)^3}\frac{D_u(p_{Y^*})}{10}\overline{u}_\Lambda P_{\mu\nu\lambda\sigma}\{\frac{g_1^u}{2M_\Lambda}(p^\mu \epsilon_\gamma^\nu \not{p}_\gamma - p_\gamma^\mu p_\gamma^\nu \not{\epsilon}) + \\ &+ \frac{g_2^u}{(2M_\Lambda)^2}(\epsilon \cdot p_\Lambda p_\gamma^\mu p_\gamma^\nu - p_\gamma \cdot p_\Lambda p_\gamma^\mu \epsilon^\nu)\}(\not{p}_{Y^*} + M_{Y^*}) p_K^\lambda p_K^\sigma \gamma_5 u_p, \end{aligned} \tag{4.76}$$

and

$$\begin{aligned} M^u_{\frac{5}{2}-} &= -i\frac{e g_3^u}{(M_\pi)^3}\frac{D_u(p_{Y^*})}{10}\overline{u}_\Lambda \gamma_5 P_{\mu\nu\lambda\sigma}\{\frac{g_1^u}{2M_\Lambda}(p^\mu \epsilon_\gamma^\nu \not{p}_\gamma - p_\gamma^\mu p_\gamma^\nu \not{\epsilon}) + \\ &+ \frac{g_2^u}{(2M_\Lambda)^2}(\epsilon \cdot p_\Lambda p_\gamma^\mu p_\gamma^\nu - p_\gamma \cdot p_\Lambda p_\gamma^\mu \epsilon^\nu)\}(\not{p}_{Y^*} + M_{Y^*}) p_K^\lambda p_K^\sigma u_p, \end{aligned} \tag{4.77}$$

for positive and negative parity, respectively. As with the s-channel contribution, the amplitudes can be re-expressed afte summing over repeated indices. This yields

$$\begin{aligned} M^u_{\frac{5}{2}+} = \overline{u}_\Lambda\{&\not{p}_\gamma(\not{p}_{Y^*} + M_{Y^*})F_1[10a - 2b + 2\not{I}\not{p}_K + 2\not{K}\not{p}_{Y^*}] - \\ &\not{\epsilon}(\not{p}_{Y^*} + M_{Y^*})F_1[10a' - 2b' + 4\not{J}\not{p}_K + 4\not{N}\not{p}_{Y^*}] \\ &+(\not{p}_{Y^*} + M_{Y^*})F_2(\epsilon \cdot p_\Lambda)[10a' - 2b' + 4\not{J}\not{p}_K + 4\not{N}\not{p}_{Y^*}] - \\ &(\not{p}_{Y^*} + M_{Y^*})F_2(p_\gamma \cdot p_\Lambda)[10a - 2b + 2\not{I}\not{p}_K + 2\not{K}\not{p}_{Y^*}]\}\gamma_5 u_p, \end{aligned} \tag{4.78}$$

$$
\begin{aligned}
M^u_{\frac{5}{2}-} = \overline{u}_\Lambda \gamma_5 \{ & \not{p}_\gamma (\not{p}_{Y^*} + M_{Y^*}) F_1 [10a - 2b + 2I\!\!\!/ \not{p}_K + 2K\!\!\!/ \not{p}_{Y^*}] - \\
& \not{\epsilon} (\not{p}_{Y^*} + M_{Y^*}) F_1 [10a' - 2b' + 4J\!\!\!/ \not{p}_K + 4N\!\!\!/ \not{p}_{Y^*}] \\
& + (\not{p}_{Y^*} + M_{Y^*}) F_2 (\epsilon \cdot p_\Lambda) [10a' - 2b' + 4J\!\!\!/ \not{p}_K + 4N\!\!\!/ \not{p}_{Y^*}] - \\
& (\not{p}_{Y^*} + M_{Y^*}) F_2 (p_\gamma \cdot p_\Lambda) [10a - 2b + 2I\!\!\!/ \not{p}_K + 2K\!\!\!/ \not{p}_{Y^*}] \} u_p
\end{aligned}
\tag{4.79}
$$

for positive and negative parities, respectively. The four vectors I^μ, J^μ, K^μ, and N^μ and the lorentz scalars a, a', b, and b' are defined as in the s-channel with $p_p \to p_\Lambda$, $M_p \to M_\Lambda$, and $p_{N^*} \to p_{Y^*}$, $M_{N^*} \to M_{Y^*}$. Explicit expressions are given in Appendix A. In the u-channel, F_1 and F_2 are defined as follows:

$$
\begin{aligned}
F_1 \equiv F_1(p_{Y^*}) &= \frac{e g_1^u g_3^u D_u(p_{Y^*})}{20 M_{p\Lambda} M_\pi^3}, \\
F_2 \equiv F_2(p_{Y^*}) &= \frac{e g_2^u g_3^u D_s(p_{Y^*})}{40 M_\Lambda^2 M_\pi^3}.
\end{aligned}
\tag{4.80}
$$

The parameters in the model are defined as the coupling products between the strong and photon vertices. In the s-channel, these are given by the dimensionless quantities

$$
\begin{aligned}
G_1^s &= g_1^s \cdot g_3^s, \\
G_2^s &= g_2^s \cdot g_3^s,
\end{aligned}
\tag{4.81}
$$

and

$$
\begin{aligned}
G_1^u &= g_1^u \cdot g_3^u, \\
G_2^u &= g_2^u \cdot g_3^u,
\end{aligned}
\tag{4.82}
$$

in the u-channel.

4.1.6 t-channel contribution

Contributions to the reaction's amplitude due to a t-channel born term, as well as two vector particles are included in the model. Their significance in the reaction is still not very well understood, but they seem to play an important role in replicating contributions of higher spin nucleon resonances, mostly spin $\frac{7}{2}$ particles [16]. We are thus interested in the dependence of the differential cross section and spin polarization observables on t-channel contributions and how they are affected when higher spin resonances, $J = \frac{5}{2}$ and higher energy resonances are added to the model.

The t-channel contributions are constructed with the same prescription as used in [15, 42], where

$$D(p_K) = \frac{1}{p_K^2 - M_K^2} \tag{4.83}$$

describes the propagation of the t-channel born term, K^+, and

$$D(p_{K^{**}}) = \frac{-g^{\mu\nu} + \frac{p^\mu_{K^{**}} p^\nu_{K^{**}}}{M^2_{K^{**}}}}{p^2_{K^{**}} - M^2_{K^{**}}}, \tag{4.84}$$

describes the propagation of the two vector particles, $K^{**} = K^1(1270)$, $K^*(892)$. The born term amplitude is proportional to the products of the electromagnetic vertex $KK\gamma$ and the strong vertex ΛKp defined in Section (4.1.2) and can be expressed by

$$M_K = e g_{\Lambda kp} \overline{u}_\Lambda \epsilon \cdot (2p_K - p_\gamma) D(p_K) \gamma_5 u_p, \tag{4.85}$$

where $g_{\Lambda Kp}$ corresponds to the s-channel born coupling constant. Again, a real photon condition,, $\epsilon^\mu p_{\mu\gamma} = 0$, can be used to reexpress the amplitude by

$$M_K = \frac{e g_{\Lambda kp}}{p_K^2 - M_K^2} \overline{u}_\Lambda \epsilon^\mu_\gamma p_{\mu,K} \gamma_5 u_p. \tag{4.86}$$

For the vector resonance terms, the hadronic vertex resembles that which couples two fermions and a photon. In particular, we can write the $\Lambda p K^{**}$ vertex as

$$\nu^{\mu}_{\Lambda p K^{**}} = \{g^V \gamma^\mu + \frac{g^T}{M_B + M_\Lambda} \gamma^\nu \gamma^\mu p_{K^{**},\nu}\}, \tag{4.87}$$

where the the coupling g^V indicates the strong vector couping, equivalent to the photon charge coupling; and g^T is the strong tensor coupling equivalent to the magentic coupling between a photon and a charged particle. A γ_5 factor should be included in Eq. (4.87) for positive parity resonances, such as for the $K^{**} = K^1(1270)$ resonance. The electromagetic interaction responsible for the excitation of the negative parity resonance K^* from a ground state kaon is given by

$$\frac{g_{\gamma K K^*}}{M_{sc}} \epsilon^{\mu\nu\rho\lambda} \epsilon_\nu p_{\gamma\rho} p_{K^*,\lambda}, \tag{4.88}$$

where $\epsilon^{\mu\nu\rho\lambda} = \pm 1$ for even or odd permutations of the indices respectively, and M_{sc} is a scaling mass that is set to 1000 MeV as in [15, 42]. For the excitation of the positive parity resonance K^1, the vertex is given by

$$\frac{g_{\gamma K K^1}}{M_{sc}} (\epsilon^\nu p_{K^1\nu} p^\mu_\gamma - p^\nu_\gamma p_{K^1\nu} \epsilon^\mu). \tag{4.89}$$

Using Eqs. (4.87) and (4.88) together with the propagator in Eq. (4.84) and the identities

$$i\epsilon_{\nu\rho\lambda\mu}\gamma_5\gamma^\mu = \gamma_\nu\gamma_\rho\gamma - g_{\nu\rho\lambda}\gamma_\lambda + g_{\nu\lambda}\gamma_\rho \tag{4.90}$$

and $\gamma_5\gamma_5 = \bar{1}$, the amplitude for the negative parity $K^*(892)$ can be expressed by

$$\begin{aligned} M_{K^*} = -iF(p_{K^*})\overline{u}_\Lambda \gamma_5 \{\frac{G^V_{K^*}}{M_{sc}} + \frac{G^T_{K^*}}{M_{sc}(M_B + M_\Lambda)} \not{p}_{K^*}\} \cdot \\ \{-\not{\epsilon}\not{p}_\gamma \not{p}_{K^*} - (\epsilon \cdot p_{K^*})\not{p}_\gamma + \frac{i\epsilon^{\nu\rho\lambda\mu}}{M^2_{K^*}} \epsilon_\nu p_{\gamma,\rho} p_{K^*,\lambda} p_{K^*,\mu}\} u_p, \end{aligned} \tag{4.91}$$

where $F(p_{K^*}) = (p^2_{K^{**}} - M^2_{K^{**}})^{-1}$, and the vector and tensor coupling products are used:

$$G^V_{K^*} = g_{\gamma KK^*} g^V_{K^*},$$
$$G^T_{K^*} = g_{\gamma KK^*} g^T_{K^*}. \tag{4.92}$$

Similarly, using Eqs. (4.87) and (4.89) together with the propagator in Eq. (4.84), the amplitude for the $K^1(1270)$ can be expressed by

$$M_{K^1} = F(p_{K^1}) u_\Lambda \{ \frac{G^V_{K^1}}{M_{sc}} [-(\epsilon \cdot p_{K^1}) \not{p}_\gamma + (p_\gamma \cdot p_{K^*}) \not{\epsilon}] + \frac{G^T_{K^1}}{M_{sc}(M_B + M_\Lambda)} [-(\epsilon \cdot p_{K^1}) \not{p}_\gamma + (p_\gamma \cdot p_{K^*}) \not{\epsilon}] \not{p}_{K^1} \} \gamma_5 u_p, \tag{4.93}$$

where the vector and tensor couplings products are defined by

$$G^V_{K^1} = g_{\gamma KK^1} g^V_{K^1},$$
$$G^T_{K^1} = g_{\gamma KK^1} g^T_{K^1}. \tag{4.94}$$

4.2 Amplitudes and Pauli reduction

Having defined the amplitudes for the different contributions to the reaction, the general structure of the complete reaction S-matrix for this model can be expressed by

$$T = \sum_k M^k_{born} + \sum_{ij} M^{ij}_{J=\frac{1}{2}} + \sum_{ij} M^{ij}_{J=\frac{3}{2}} + \sum_{ij} M^{ij}_{J=\frac{5}{2}} + \sum_k M^k_{t-channel}. \tag{4.95}$$

Where the sum over k in the first term indicates a sum over each channel's born terms, the sum over i and j indicate sums over all of the excited states in both the s and u-channels, and the last term's sum over k indicates a sum over the two t-channel resonances included in this study. Using Eq. (4.95), the reaction's amplitude can be expressed by

$$M = \overline{u}_\Lambda T u_p \tag{4.96}$$

for an incoming proton and outgoing Λ particle. The contributions to the amplitudes for particles with $J \leq \frac{5}{2}$ were derived in Section (4.1) and given as proportional to contractions of the form $\gamma_\mu p_1^\mu \gamma_\nu p_2^\nu ...$ for some four vectors p_μ^i. After carrying out these contractions the remaining Dirac matrix dependence allows the complete amplitude to be expressed as a sum of four terms

$$M = \overline{u}_\Lambda \sum_{s,u,t;N,Y,K} [\hat{A} + \hat{B}\gamma_5 + \hat{C}\gamma^0 + \hat{D}\gamma^0\gamma_5]u_p. \tag{4.97}$$

The $2X2$ operators $\hat{A}$, $\hat{B}$, $\hat{C}$, and $\hat{D}$ depend on the channel as well as on the angular momentum parity combination of each of the states contributing to the reaction's amplitude. Explicit expressions for these operators for different J^p states are given in Appendix B.

Uisng Equation (4.97), the amplitude for the reaction can be calculated for any given spin combinations of the initial and final baryon states with momenta p_I and p_F respectively. Eq. (4.97) can be reduced to an equivalent Pauli form, i.e. one involving two-component spinors for the initial and final states, which are eigenvectors of σ_z. The Pauli reduction begins by first expressing the two dirac spinors as

$$u(p_I) = N_I \chi \cdot \begin{pmatrix} \bar{1} \\ \vec{\sigma} \cdot \vec{\hat{p}}_I \end{pmatrix}, \tag{4.98}$$

and

$$u(p_F) = N_F \chi^\dagger \cdot \left(\bar{1}, -\vec{\sigma} \cdot \vec{\hat{p}}_I\right), \tag{4.99}$$

where N is a normalization factor given by

$$N = \sqrt{\frac{E+m}{2m}}, \tag{4.100}$$

$\bar{1}$ is the two by two unit matrix, and

$$\vec{\hat{p}} = \frac{\vec{p}}{E+m}. \tag{4.101}$$

The vectors χ are eigenvectors of σ_z:

$$\chi_+ = \begin{pmatrix} 1 \\ 0 \end{pmatrix}, \tag{4.102}$$

and

$$\chi_- = \begin{pmatrix} 0 \\ 1 \end{pmatrix} \tag{4.103}$$

for spin up and spin down respectively.

The term in Eq. (4.97) involving the operator $\hat{A}$ can be reduced to its Pauli form by using the definitions given in Eqs. (4.98) and (4.99).

$$\overline{u}(p_F)\hat{A}u(p_I) = (N_I N_F)\chi^\dagger[\hat{A} - (\vec{\sigma}\cdot\vec{\hat{p}}_F)\hat{A}(\vec{\sigma}\cdot\vec{\hat{p}}_I)]\chi. \tag{4.104}$$

Similarly, the expressions for the terms involving the operators $\hat{B}$, $\hat{C}$, and $\hat{D}$ are expressed by

$$\overline{u}(p_F)\hat{B}\gamma_5 u(p_I) = (N_I N_F)\chi^\dagger[\hat{B}(\vec{\sigma}\cdot\vec{\hat{p}}_F) - (\vec{\sigma}\cdot\vec{\hat{p}}_I)\hat{B}]\chi, \tag{4.105}$$

$$\overline{u}(p_F)\hat{C}\gamma^0 u(p_I) = (N_I N_F)\chi^\dagger[\hat{C} + (\vec{\sigma}\cdot\vec{\hat{p}}_F)\hat{C}(\vec{\sigma}\cdot\vec{\hat{p}}_I)]\chi, \tag{4.106}$$

$$\overline{u}(p_F)\hat{D}\gamma^0\gamma_5 u(p_I) = (N_I N_F)\chi^\dagger[\hat{D}(\vec{\sigma}\cdot\vec{\hat{p}}_F) + (\vec{\sigma}\cdot\vec{\hat{p}}_I)\hat{D}]\chi, \tag{4.107}$$

making use the following representations for the dirac matrices γ^0 and γ_5 with $2X2$ components:

$$\gamma^0 = \begin{pmatrix} \bar{1} & \bar{0} \\ \bar{0} & -\bar{1} \end{pmatrix}, \tag{4.108}$$

and

$$\gamma_5 = \begin{pmatrix} \bar{0} & \bar{1} \\ \bar{1} & \bar{0} \end{pmatrix}. \tag{4.109}$$

Using Eqs. (4.104)-(4.107) the reaction's amplitude can be now expressed in its Pauli form by

$$M = (N_I N_F)\chi_F^\dagger[(\hat{A}+\hat{C}) + (\hat{B}+\hat{D})\vec{\sigma}\cdot\vec{\hat{p}}_I + \vec{\sigma}\cdot\vec{\hat{p}}_F(\hat{D}-\hat{B}) + \vec{\sigma}\cdot\vec{\hat{p}}_F(\hat{C}-\hat{A})\vec{\sigma}\cdot\vec{\hat{p}}_F]\chi_I, \quad (4.110)$$

where now the initial and final spinors do not depend on momentum and energy. All of the dynamical information is stored in the operators; therefore, the amplitude can be calculated with respect to the original quantized axis $\hat{z}$ or with respect to any other axis by rotating the Pauli spinors appropriately without altering the form of the operators. In particular the amplitude is completely determined by using the χ_+ and χ_- defined with respect to any rotation matrix belonging to $SU(2)$.

4.3 Resonance Widths

To properly evaluate the contributions to the amplitudes from resonances in the s-channel, a model for the widths Γ has to be introduced. In this study, an effective lagrangian model is used to calculate the amplitudes for the reactions responsible for the resonance decay widths. The model makes use of the empirical on-shell total widths of the particles and employs experimental values for their branching ratios into two and three-body decay channels to calculate the coupling associated with each decay.

4.3.1 Decays into stable baryons

In this model, two-body decays are defined as decays of a resonance R with angular momentum $J \leq \frac{5}{2}$ into a stable nucleon or hyperon (Λ or Σ^0) paticle with angular momentum-parity $J = \frac{1}{2}^+$ and a pseudoscalar meson,

$$R \rightarrow \frac{1}{2}^+ + 0^-. \quad (4.111)$$

As mentioned in the introduction of Section (4.1), the on-shell values for the branching ratios to particular two-body channels are taken from the particle data tables [18]. These are shown in Table (4.7).

	Two body channels		
Resonance	$N\pi$	$N\eta$	ΛK
$N^*(1440)$	0.65		
$N^*(1710)$	0.15		
$N^*(1535)$	0.45	0.060	0.14
$N^*(1650)$	0.77	0.525	
$N^*(1720)$	0.15	0.06	0.07
$N^*(1520)$	0.60		
$N^*(1700)$	0.10		
$N^*(1680)$	0.60		
$N^*(1675)$	0.40		

Table 4.7: Branching ratios into two-body decay channels

Two-body decay channels are considered for all s-channel resonances included in the model. The vertices for decays of resonances with $J = \frac{1}{2}$ into a $\frac{1}{2}^+$ nucleon and a pseudoscalar meson are given by

$$M_{\frac{1}{2}+} = g\overline{u}_R\gamma_5 u_B \tag{4.112}$$

for resonances with positive parity, and

$$M_{\frac{1}{2}-} = g\overline{u}_R u_B \tag{4.113}$$

for resonances with negative parity. Here u_R is the spinor of the decaying resonance, and u_B of the $\frac{1}{2}^+$ decay product. The calculation is done in the resonance decay CM frame, where

$$\sqrt{s} = E_B + E_p \tag{4.114}$$

and

$$\vec{p}_B + \vec{p}_p = 0. \tag{4.115}$$

E_p and $\vec{p}_p$ correspond to the energy and spatial momentum of the outgoing pseudoscalar meson. In the CM frame, the spinors can be expressed by

$$\overline{u}_R = \sqrt{2s}\chi^\dagger(\bar{1},\bar{0}), \tag{4.116}$$

$$u_B = \sqrt{E_B + M_B}\begin{pmatrix} \bar{1} \\ \frac{1}{E_B+M_B}(\vec{\sigma}\cdot\vec{p}_B) \end{pmatrix}\chi. \tag{4.117}$$

To perform the calculation, the $\hat{z}$ axis is chosen to lie along the direction of the baryon's momentum $\vec{p}_B$. This coordinate system is appropriate for use of the helicity basis. In this basis, the baryon's spinor is quantized along the direction of its momentum, and it is given by χ_{m_B}, where $m_B = \pm 1$ labels spin parallel or antiparallel to $\vec{p}_B$. The spinor for a $J = \frac{1}{2}$ resonance must be expressed in this basis and is therefore written as a linear combination of Pauli spinors in the helicity basis, i.e.,

$$\chi^\dagger_{m_R}(R) = \sum_\lambda D^{\frac{1}{2}*}_{m_R\lambda}(-\theta,-\phi)\chi^\dagger_\lambda = \sum_\lambda D^{\frac{1}{2}}_{\lambda m_R}(\theta,\phi)\chi^\dagger_\lambda, \tag{4.118}$$

where $D^{\frac{1}{2}}_{\lambda m}$ are the $J = \frac{1}{2}$ rotation matrices and the angles θ and ϕ define the position of the helicity basis with respect to the coordinate system defined by the direction of the photon. Eqs. (4.116)-(4.118) and the othogonality relation between Pauli spinors,

$$\chi^\dagger_{m_R}(R)\cdot\chi_{m_B}(B) = D^{\frac{1}{2}}_{m_B m i_R}(\theta,\phi), \tag{4.119}$$

are used to evaluate the decay amplitudes. These are given by

$$M_{\frac{1}{2}+} = g\eta\cdot D^{\frac{1}{2}}_{m_B m_R}(\theta,\phi), \tag{4.120}$$

and

$$M_{\frac{1}{2}-} = g\eta\cdot(2m_B)\frac{p_B}{E_B+M_B}D^{\frac{1}{2}}_{m_B m_R}(\theta,\phi) \tag{4.121}$$

for positive and negative parities respectively, where

$$\eta = \sqrt{2s^{\frac{1}{2}}(E_B + M_B)}. \tag{4.122}$$

For decays involving resonances with $J = \frac{3}{2}$, it is first useful to express the resonance Dirac spinor as a direct product of a spin $\frac{1}{2}$ Dirac spinor and a vector. The coupling is carried out using $SU(2)$ spin Clebsch-Gordon coefficients. For a given spin $\frac{3}{2}$ particle, the wavefunction is defined by

$$u^{\mu}_{m_R} \equiv \sum_{m_1 m_2} < \frac{1}{2} m_1, 1 m_2 | \frac{3}{2} m_R > u_{m_1} \epsilon^{\mu}_{m_2}, \tag{4.123}$$

$$u^{\mu}_{m_R} \equiv \sum_{m_1 m_2} < \frac{1}{2} m_1, 1 m_2 | \frac{3}{2} m_R > u_{m_1} (\epsilon^{\mu}_{m_2})^*. \tag{4.124}$$

The indices m_1, m_2, and m_R label the spin projections of the individual paritcles, and ϵ^{μ} is the polarization of the spin 1 vector particle. For decays into spin $\frac{1}{2}$ baryons the following vertices are employed:

$$M_{\frac{3}{2}^+} = \frac{g}{M_K} u_{R,\mu} p_p^{\mu} u_B \tag{4.125}$$

for resonances with positive parity, and

$$M_{\frac{3}{2}^-} = \frac{g}{M_K} u_{R,\mu} p_p^{\mu} \gamma_5 u_B \tag{4.126}$$

for negative parity baryons. Using the wavefunctions for the spin $\frac{3}{2}$ particles given in Eqs. (4.123) and (4.124), the vertices can be expressed by

$$M_{\frac{3}{2}^+} = g \sum_{m_1 m_2} < \frac{1}{2} m_1, 1 m_2 | \frac{3}{2} m_R > u_{m_1} (\epsilon^{\mu}_{m_2})^* p_{p\mu} u_B, \tag{4.127}$$

$$M_{\frac{3}{2}^-} = g \sum_{m_1 m_2} < \frac{1}{2} m_1, 1 m_2 | \frac{3}{2} m_R > u_{m_1} (\epsilon^{\mu}_{m_2})^* p_{p\mu} \gamma_5 u_B. \tag{4.128}$$

The polarization four-vector of the spin 1 particle is rotated to lie along the z-axis defined by the direction of the baryon's spatial momentum, so that

$$(\epsilon^{\mu})^* p_{p\mu} = |\vec{p}_B| D^1_{0,m_2}(\theta,\phi), \tag{4.129}$$

where

$$\begin{aligned} \vec{\epsilon}(m_2 = \pm 1)^* &= \pm\frac{1}{\sqrt{2}}(\hat{x} - i\hat{y}), \\ \vec{\epsilon}(m_2 = 0)^* &= \hat{z} \end{aligned} \tag{4.130}$$

since $\vec{p}_B = -\vec{p}_p$ in the resonance's rest frame. Using Eqs. (4.118) and (4.122) and

$$\sum_{m_1 m_2} < \frac{1}{2} m_1, 1 m_2 | \frac{3}{2} m_R > D^1_{0,m_2}(\theta,\phi) D^{\frac{1}{2}}_{m_B m_1}(\theta,\phi) = \sum_{m_B} < \frac{1}{2} m_B, 1(m=0) | \frac{3}{2} m_B > D^{\frac{3}{2}}_{m_B m_R} \tag{4.131}$$

reduces the amplitudes to

$$M_{\frac{3}{2}+} = -\frac{g}{M_K}\sqrt{\frac{2}{3}} |\vec{p}_B| \eta D^{\frac{3}{2}}_{m_B m_R}(\theta,\phi), \tag{4.132}$$

$$M_{\frac{3}{2}-} = -\frac{g}{M_K}\frac{|\vec{p}_B|^2}{E_B + M_B}\eta(2m_B)\sqrt{\frac{2}{3}} \eta D^{\frac{3}{2}}_{m_B m_R}(\theta,\phi) \tag{4.133}$$

for positive and negative parities, respectively.

The construction of a resonance with spin $\frac{5}{2}$ is carried out by first defining the wavefunction

$$\overline{u}^{\mu\nu}_{m_R} = \sum_{m_1 m_2} < \frac{3}{2} m_1, 1 m_2 | \frac{5}{2} m_R > \overline{u}^{\mu}_{m_1} (\epsilon^{\nu}_{m_2})^*, \tag{4.134}$$

which can be further expressed as

$$\overline{u}^{\mu\nu}_{m_R} = \sum_{m_1 m_2} < \frac{3}{2} m_1, 1 m_2 | \frac{5}{2} m_R >< \frac{1}{2} m_3, 1 m_4 | \frac{3}{2} m_1 > \overline{u}_{m_3} (\epsilon^{\mu}_{m_4})^* (\epsilon^{\nu}_{m_2})^*. \tag{4.135}$$

The vertices for decays into a spin $\frac{1}{2}$ baryon and a pseudoscalar meson are then given by

$$\begin{aligned} M_{\frac{5}{2}+} &= \frac{ig}{(M_K)^2} \sum_{m_1 m_2 m_3 m_4} < \frac{3}{2} m_1, 1 m_2 | \frac{5}{2} m_R > < \frac{1}{2} m_3, 1 m_4 | \frac{3}{2} m_1 > \\ &\cdot \ \overline{u}_{m_3} (\epsilon^{\mu}_{m_4})^* (\epsilon^{\nu}_{m_2})^* \gamma_5 p_{p\mu} p_{p\nu} u_{m_B}, \\ M_{\frac{5}{2}-} &= \frac{ig}{(M_K)^2} \sum_{m_1 m_2 m_3 m_4} < \frac{3}{2} m_1, 1 m_2 | \frac{5}{2} m_R > < \frac{1}{2} m_3, 1 m_4 | \frac{3}{2} m_1 > \\ &\cdot \ \overline{u}_{m_3} (\epsilon^{\mu}_{m_4})^* (\epsilon^{\nu}_{m_2})^* p_{p\mu} p_{p\nu} u_{m_B} \end{aligned} \tag{4.136}$$

for positive and negative parity resonances, repectively. After evaluating the matrix elements, the decay amplitudes reduce to

$$M_{\frac{5}{2}+} = \frac{ig}{(M_K)^2} \frac{|\vec{p}_B|^3}{E_B + M_B} \cdot \eta \cdot \sqrt{\frac{2}{3}} (2 m_B) A(m_B) D^{\frac{5}{2}}_{m_B m_R}(\theta, \phi), \tag{4.137}$$

$$M_{\frac{5}{2}-} = \frac{ig}{(M_K)^2} |\vec{p}_B|^2 \cdot \eta \cdot \sqrt{\frac{2}{3}} A(m_B) D^{\frac{5}{2}}_{m_B m_R}(\theta, \phi), \tag{4.138}$$

where

$$A(m_B) = < \frac{3}{2} m_B, 1 m_0 | \frac{5}{2} m_B > . \tag{4.139}$$

To calculate the widths Γ for the decays of all resonances included in Table (4.7) into the $J = \frac{1}{2}^+ + 0^-$ channel, the following CM expression is used:

$$\Gamma = \frac{|\vec{p}_B|}{32 \pi^2 s} \int d\Omega \frac{1}{J_R + 1} \sum_{m_R m_B} |M|^2. \tag{4.140}$$

This expression can be simplified by noting that the amplitudes calculated for the decaying particles are proportional to a matrix representation of the rotation group of dimension J_R, which satisfy

$$\int d\Omega |D^{J_R}_{m_B m_R}(\theta, \phi)|^2 = \frac{4\pi}{2 J_R + 1}. \tag{4.141}$$

Using Eqs. (4.140)-(4.141) and using the following values

$$|2m_B|^2 = 1$$
$$|A(m_B)|^2 = \frac{3}{5}$$

for $m_B = \pm\frac{1}{2}$, and summing over the spin projections m_B yields

$$\Gamma(\tfrac{1}{2}^+ \to \tfrac{1}{2}^+ + 0^-) = \frac{g^2}{4\pi}\frac{|\vec{p}_B|^3}{Q^2}, \tag{4.142}$$
$$\Gamma(\tfrac{1}{2}^- \to \tfrac{1}{2}^+ + 0^-) = \frac{g^2}{4\pi}\frac{|\vec{p}_B|Q^2}{s}, \tag{4.143}$$
$$\Gamma(\tfrac{3}{2}^+ \to \tfrac{1}{2}^+ + 0^-) = \frac{1}{12\pi}\frac{g^2}{M_K^2}|\vec{p}_B|^3\frac{Q^2}{s}, \tag{4.144}$$
$$\Gamma(\tfrac{3}{2}^- \to \tfrac{1}{2}^+ + 0^-) = \frac{1}{12\pi}\frac{g^2}{M_K^2}\frac{|\vec{p}_B|^5}{Q^2}, \tag{4.145}$$
$$\Gamma(\tfrac{5}{2}^+ \to \tfrac{1}{2}^+ + 0^-) = \frac{1}{30\pi}\frac{g^2}{M_K^4}\frac{|\vec{p}_B|^7}{Q^2}, \tag{4.146}$$
$$\Gamma(\tfrac{5}{2}^- \to \tfrac{1}{2}^+ + 0^-) = \frac{1}{30\pi}\frac{g^2}{M_K^4}|\vec{p}_B|^5\frac{Q^2}{s}, \tag{4.147}$$

where $Q^2 = \sqrt{s}(E_B + M_B)$.

4.3.2 Decays into unstable baryons and mesons

In addition to two-body decays, this study incorporates three-body decay channels, where the widths are approximated by two-body decays into a stable hadron and another unstable hadron. Such decays are included for all s-channel resonances for which the avialable CM energy exceeds the decay threshold energy $\sqrt{s}$. On-shell branching ratios for these decay channels are given in Table (4.8). The amplitudes for decay of a $J = \frac{1}{2}$ resonance into the $\Delta\pi$ channel can be expressed by

$$M_{\frac{1}{2}^+} = -\frac{g}{M_K}u_{M_R}p_p^\mu u_{\mu,m_B},$$
$$M_{\frac{1}{2}^-} = -\frac{g}{M_K}\overline{u}_{M_R}p_p^\mu\gamma_5 u_{\mu,m_B}. \tag{4.148}$$

	Three body channels		
Resonance	σN	$\Delta\pi$	ρN
$N^*(1440)$	0.075	0.25	0.025
$N^*(1710)$	0.25	0.26	0.14
$N^*(1535)$			0.025
$N^*(1650)$		0.03	0.07
$N^*(1720)$			0.73
$N^*(1520)$		0.2	0.20
$N^*(1700)$		0.8	0.1
$N^*(1680)$	0.15	0.125	0.125
$N^*(1675)$		0.60	

Table 4.8: Branching ratios into three-body decay channels

Unlike decays of particles with $J = \frac{3}{2}$ into a spin $\frac{1}{2}$ baryon and a meson in the resonance rest frame, this vertex involves a moving spin $\frac{3}{2}$ particle, and thus Eqs. (4.129) and (4.130) cannot be used. The wavefunction of the Δ particle can be expressed by

$$u^{\mu}_{m_B} = \sum_{m_1 m_2} < \frac{1}{2} m_1, 1 m_2 | \frac{3}{2} m_B > u_{m_1} \epsilon^{\mu}_{m_2}. \tag{4.149}$$

To evaluate the inner products Eqs. (4.148) inner product between the polarization vector ϵ^{μ} and the mesons's four momentum, note first that

$$\epsilon_{\mu} p^{\mu}_{B} = 0 \tag{4.150}$$

in the rest frame of the moving baryon. Since this is a Lorentz invariant, it must be zero in the rest frame of the resonance. Therefore,

$$\epsilon_0 E_B - \vec{\epsilon} \cdot \vec{p}_B = 0, \tag{4.151}$$

and

$$\epsilon_{\mu} p^{\mu}_{p} = \epsilon_0 \sqrt{s} \tag{4.152}$$

since $\vec{p}_B = -\vec{p}_p$ and $\sqrt{s} = (E_B + E_P)$ in the rest frame of the resonance. Using these results, the amplitudes can be expressed by

$$\begin{aligned} M_{1\,2^+} &= -\frac{g}{M_K}\sqrt{s}\sum_{m_1 m_2} < \tfrac{1}{2} m_1, 1 m_2 | \tfrac{3}{2} m_B > \epsilon_0(m_2) u_{m_R} u_{m_1}, \\ M_{1\,2^-} &= -\frac{g}{M_K}\sqrt{s}\sum_{m_1 m_2} < \tfrac{1}{2} m_1, 1 m_2 | \tfrac{3}{2} m_B > \epsilon_0(m_2) u_{m_R} \gamma_5 u_{m_1}. \end{aligned} \tag{4.153}$$

The sums in Eq. (4.153) can be evaluated explicitly by noting that in the helicity basis, the time component of the massive spin 1 particle polarization is given by

$$\epsilon_0(m_2) = \frac{|\vec{p}_B|}{M_B}\delta_{m_2 0}. \tag{4.154}$$

Using the above equation and Eq. (4.119) the final expressions for the amplitudes for positive and negative parity $J = \frac{1}{2}$ resonances are given by

$$\begin{aligned} M_{1\,2^+} &= \sqrt{\frac{2}{3}}\eta\frac{|\vec{p}_B|}{M_B} D^{1}_{m_B m_R}(\theta,\phi) \\ M_{1\,2^-} &= \sqrt{\frac{2}{3}}\eta\frac{|\vec{p}_B|^2}{M_B\sqrt{E_B + M_B}} (2m_B) D^{1}_{m_B m_R}(\theta,\phi), \end{aligned} \tag{4.155}$$

where $m_B = \pm\frac{1}{2}$.

Decays of resonances with $J = \frac{3}{2}$ into a $\Delta\pi$ can be evaluated using the following vertices:

$$\begin{aligned} M_{3\,2^+} &= g u_{\mu, m_R} \gamma_5 u^{\mu}_{m_B}, \\ M_{3\,2^-} &= g u_{\mu, m_R} u^{\mu}_{m_B} \end{aligned} \tag{4.156}$$

for positive and negative parities, respectively. The calculation is done using the definitions in Section (4.3.1) for the wavefunctions belonging to resonances with $J = \frac{3}{2}$, and the

definition given in Eq. (4.149) for the Δ wavefunction, which yield

$$\begin{aligned} M_{\frac{3}{2}+} &= -g\frac{1}{3}\eta\frac{|\vec{p}_B|}{E_B+M_B}D^{\frac{3}{2}}_{m_B m_R}(\theta,\phi), \\ M_{\frac{3}{2}-} &= -g\eta D^{\frac{3}{2}}_{m_B m_R}(\theta,\phi). \end{aligned} \tag{4.157}$$

The amplitudes for $J=\frac{5}{2}$ resonances decaying into a Δ and a π are obtained from the following veritices:

$$\begin{aligned} M_{\frac{5}{2}+} &= -\frac{g}{M_K}\overline{u}_{\mu\nu m_R}p_p^{\nu}u_{\mu m_B}, \\ M_{\frac{5}{2}-} &= -\frac{g}{M_K}\overline{u}_{\mu\nu m_R}p_p^{\nu}\gamma_5 u_{\mu m_B}, \end{aligned} \tag{4.158}$$

for positive and negative parities, respectively. The calculation is carried out using the wavefunction in Eq. (4.135) for the resonance and Eq. (4.149) for the Δ particle. This yields

$$\begin{aligned} M_{\frac{5}{2}+} &= -g\frac{g}{M_K}A(m_B)D^{\frac{5}{2}}_{m_B m_R}(\theta,\phi), \\ M_{\frac{5}{2}-} &= -g\frac{g}{M_K}\frac{|\vec{p}_B|^2}{E_B+M_B}f(m_B)A(m_B)D^{\frac{5}{2}}_{m_B m_R}(\theta,\phi), \end{aligned} \tag{4.159}$$

with coefficients $A(m_B)=\sqrt{\frac{2}{5}}$ for $m_B=\pm\frac{3}{2}$ and $\sqrt{\frac{3}{5}}$ for $m_B=\pm\frac{1}{2}$ and $f(m_B)=\frac{2}{3}m_B$. Using Eqs. (4.140) and (4.141) the following expressions for the widths for decays of resonances with $J\leq\frac{5}{2}$ into the $\Delta\pi$ channel are obtained:

$$\Gamma(\frac{1}{2}^+\to\frac{3}{2}^++0^-) = \frac{2}{12\pi}\frac{g^2}{M_K^2}|\vec{p}_B|^3\frac{Q^2}{M_B^2}, \tag{4.160}$$

$$\Gamma(\frac{1}{2}^-\to\frac{3}{2}^++0^-) = \frac{2}{12\pi}\frac{g^2}{M_K^2}|\vec{p}_B|^5\frac{s}{Q^2M_B^2}, \tag{4.161}$$

$$\Gamma(\frac{3}{2}^+\to\frac{3}{2}^++0^-) = \frac{5}{36\pi}\frac{g^2}{M_K^2}|\vec{p}_B|^3\frac{1}{Q^2} \tag{4.162}$$

$$\Gamma(\frac{3}{2}^-\to\frac{3}{2}^++0^-) = \frac{g^2}{4\pi M_K^2}|\vec{p}_B|\frac{Q^2}{s}, \tag{4.163}$$

$$\Gamma(\frac{5}{2}^+ \to \frac{3}{2}^+ + 0^-) = \frac{1}{12\pi}\frac{g^2}{M_K^2}|\vec{p}_B|^3\frac{Q^2}{s}, \quad (4.164)$$

$$\Gamma(\frac{5}{2}^- \to \frac{3}{2}^+ + 0^-) = \frac{1}{12\pi}\frac{g^2}{M_K^2}|\vec{p}_B|^5\frac{7}{15Q^2}, \quad (4.165)$$

where $Q^2 = \sqrt{s}(E_B + M_B)$.

Vector decays, i.e., decays to a ρ meson and nucleon, are also incorporated into the model. The vertices associated with these decays are constructed in analogy to the photon vertices given in Sections (4.1) for the s-channel resonances. The polarization four-vector of the massive vector particle is constructed in the rest frame of the resonance with the $\hat{z}$ axis rotated to lie along the direction of the outgoing nucleon. In the helicity basis

$$\begin{aligned} \vec{\epsilon}_{m_V=0} &= \frac{E_V}{M_V}\hat{z}, \\ \vec{\epsilon}_{m_V=\pm 1} &= \frac{1}{\sqrt{2}}(\hat{x} \pm i\hat{y}) \end{aligned} \quad (4.166)$$

for the space components, and

$$\epsilon^0 = \frac{|\vec{p}_V|}{M_V}\delta_{m_V 0} \quad (4.167)$$

for the time component, where m_V indicate the spin projection along the rotated z-axis.

The decay widths for resonances with $J = \frac{1}{2}$ are given by

$$\Gamma(\frac{1}{2}^\pm \to 1^- + \frac{1}{2}^+) = \frac{1}{4\pi}|\vec{p}_B|^3\frac{E_B \pm M_B}{\sqrt{s}M_V}g_V^2\{(1 - \frac{E_V}{E_B \pm M_B})^2 + 2(\frac{M_V}{E_B \pm M_B})^2\}, \quad (4.168)$$

where M_V and M_B are the masses of the meson and baryon respectively. Since the decay couplings are fixed by empirical branching ratios, and are not varied in the fitting procedure, only the term proportional to the vector coupling g_V has been kept.

Similarly, the widths for spin $\frac{3}{2}$ resonances are given by

$$\Gamma(\frac{3}{2}^{\pm} \to 1^- + \frac{1}{2}^+) = \frac{1}{8\pi}\frac{g_1^2}{4M_B^2}|\vec{p}_B|^3 \frac{E_B \pm M_B}{\sqrt{s}M_V^2}\{\frac{2}{3}(\frac{E_V^2 + |\vec{p}_B|^2}{E_B \pm M_B})^2 + \frac{1}{3}(1 - \frac{E_V}{E_B \pm M_B})^2) + M_V^2(1 + \frac{E_V}{E_B \pm M_B})\}. \tag{4.169}$$

For positive parity spin $\frac{5}{2}$ resonances, the width is given by

$$\Gamma(\frac{5}{2}^+ \to 1^- + \frac{1}{2}^+) = \frac{1}{30\pi}\frac{|\vec{p}_B|^3 g_1^2}{4M_B^2 M_\pi^2}\frac{E_B + M_B}{\sqrt{s}} \cdot \{A^2 + 2B^2 + C^2\}, \tag{4.170}$$

where

$$\begin{aligned} A &= \sqrt{s} - M_B, \\ B &= \frac{|\vec{p}_B|^2}{E_B + M_B} - \frac{A}{2}, \\ C &= \frac{E_V A}{M_V} + \frac{|\vec{p}_B|^2(E_B - E_V + M_B)}{M_V(E_B + M_B)}. \end{aligned} \tag{4.171}$$

The negative parity resonance widths are given by

$$\Gamma(\frac{5}{2}^- \to 1^- + \frac{1}{2}^+) = \frac{1}{30\pi}\frac{|\vec{p}_B|^3 g_1^2}{4M_B^2 M_\pi^2}\frac{E_B + M_B}{\sqrt{s}} \cdot \{A^2 + 2B^2 + C^2\}, \tag{4.172}$$

where

$$\begin{aligned} A &= \frac{|\vec{p}_B|}{E_B + M_B}(\sqrt{s} + M_B), \\ B &= \frac{|\vec{p}_B|}{E_B + M_B}(1 - \frac{\sqrt{s} + M_B}{2}), \\ C &= \frac{|\vec{p}_B|}{M_V}\frac{(E_V^2 + |\vec{p}_B|^2)}{E_B + M_B}. \end{aligned} \tag{4.173}$$

The mass of the pion is used to make g_1 dimensionless. Note also that for the $J = \frac{3}{2}$ and $\frac{5}{2}$ resonances, only one coupling is introduced in the expressions for the widths. This is due to the fact that we are limited to on-shell partial width information, which can only be used to extract one coupling. The other couplings must be dropped from the calculation. To

account for the instability of the Δ particle and vector meson, a method developed in [42] is used. The method involves incorporating the width of the unstable decay product by introducing a Breit-Wigner distribution. The channel width is expressed as

$$\Gamma(s) = \frac{g_1^2}{4\pi} \int_{M_{th}}^{M_{max}} \Gamma(s,x) S(x) dx, \tag{4.174}$$

where $\Gamma(s,x)$ is the phase factor for decay of the resonance into an unstable decay product of mass x, and

$$S(x) = \frac{A}{2\pi} \frac{\Gamma_{pr}}{(x - M_c)^2 + \frac{1}{4}\Gamma_{pr}^2} \tag{4.175}$$

is the Breit-Wigner distribution with normalization parameter A. The integration limits are

$$\begin{aligned} M_{th} &= \sqrt{s_{th}} - M_{stable}, \\ M_{max} &= \sqrt{s} - M_{stable}, \end{aligned} \tag{4.176}$$

where $\sqrt{s_{th}}$ is the lowest possible CM energy to form the unstable baryon or vector meson, and M_s is the mass of the stable final state nucleon or pion.

The empirical on-shell branching ratios, together with the expressions derived in this section yield a dynamical model for the well-established s-channel resonances (three to four star status,) given in Tables (4.1), (4.3) and (4.5). The total widths for resonances of two star category are treated as parameters in the fit, as mentioned in Section (4.1.1).

4.4 Parameters and Fitting Procedure

Using the effective lagrangian model developed in this chapter, two main fits are obtained to the data provided by the CLAS collaboration [9, 10] for the photoproduction reaction $\gamma + p \rightarrow K^+ + \Lambda$. One fit is performed using the low energy data, that is, for CM energies below 2 GeV, and a second fit is obtained for CM energies up to 2.6 GeV. The low energy fit includes all the well-established s and u-channel resonances with $J \leq \frac{5}{2}$ given in [18].

This fit is mainly used to study the effect on the differential cross section when the fit is extended to include polarization data and to study the relative influences of the s and u-channel coupling constants. Table (4.9) lists all of the s and u-channel resonances used in the low energy fit along with their symmetry assignments, consistent with $SU(6)XO(3)$ quark models [5, 6, 8, 7]. The higher energy fit incorporates four resonances whose existence is not

Resonance	I	J^P	$SU(3)$
$N(1440)$	$\frac{1}{2}$	$\frac{1}{2}^+$	$^2 8$
$N(1520)$	$\frac{1}{2}$	$\frac{3}{2}^-$	$^2 8$
$N(1535)$	$\frac{1}{2}$	$\frac{1}{2}^-$	$^2 8$
$N(1650)$	$\frac{1}{2}$	$\frac{1}{2}^-$	$^4 8$
$N(1675)$	$\frac{1}{2}$	$\frac{5}{2}^-$	$^4 8$
$N(1680)$	$\frac{1}{2}$	$\frac{5}{2}^+$	$^2 8$
$N(1700)$	$\frac{1}{2}$	$\frac{3}{2}^-$	$^4 8$
$N(1710)$	$\frac{1}{2}$	$\frac{1}{2}^+$	$^2 8$
$N(1720)$	$\frac{1}{2}$	$\frac{3}{2}^+$	$^2 8$
$\Lambda(1405)$	0	$\frac{1}{2}^-$	$^2 1$
$\Lambda(1520)$	0	$\frac{3}{2}^-$	$^2 1$
$\Lambda(1600)$	0	$\frac{1}{2}^+$	$^2 8$
$\Lambda(1670)$	0	$\frac{1}{2}^-$	$^4 8$
$\Lambda(1690)$	0	$\frac{3}{2}^-$	$^2 8$
$\Lambda(1810)$	0	$\frac{1}{2}^+$	$^2 8$
$\Lambda(1820)$	0	$\frac{5}{2}^+$	$^2 8$
$\Lambda(1830)$	0	$\frac{5}{2}^-$	$^4 8$
$\Lambda(1890)$	0	$\frac{3}{2}^+$	$^2 8$
$\Lambda(2110)$	0	$\frac{5}{2}^+$	
$\Sigma(1385)$	1	$\frac{3}{2}^+$	$^4 10$
$\Sigma(1660)$	1	$\frac{1}{2}^+$	$^2 8$
$\Sigma(1670)$	1	$\frac{3}{2}^-$	$^2 8$
$\Sigma(1750)$	1	$\frac{1}{2}^-$	$^2 10$
$\Sigma(1775)$	1	$\frac{5}{2}^-$	$^4 8$
$\Sigma(1915)$	1	$\frac{5}{2}^+$	$^2 8$
$\Sigma(1940)$	1	$\frac{3}{2}^-$	$^4 8$

Table 4.9: Low energy well-established resonances

yet very well established in the particle data tables [18], but as mentioned in Section (1.4), have been predicted within quark models and used in previous analyses of photoproduction data. The additional resonances are implemented because the model cannot successfully

fit the complete data set when only the resonances listed in Table (4.9) are included. The additional two-star resonances used in the model are listed in Table (4.10).

Resonance	J^P
$N(1900)$	$\frac{3}{2}^+$
$N(2000)$	$\frac{5}{2}^+$
$N(2080)$	$\frac{3}{2}^-$
$N(2200)$	$\frac{5}{2}^-$

Table 4.10: Two star resonances implemented in high energy fit

In the low energy fit, the parameters fit to the experimental data are the coupling products at the electromagnetic and strong vertices. These products were defined in Section (4.1). Most of the Born term coupling products in the three channels are related to the leading Born coupling

$$g^L = e g_{pK\Lambda}. \tag{4.177}$$

In particular, one can express the born coupling products introduced in Section (4.1.2) and (4.1.6) for the s, u and t-channel born terms as

$$\begin{aligned}
G^1_{s-born} &= g^L, \\
G^2_{s-born} &= \kappa_p g^L, && (4.178)\\
G^{1\Lambda}_{u-born} &= \kappa_\Lambda g^L, && (4.179)\\
G^{1\Sigma}_{u-born} &= e\kappa_{\Sigma\Lambda} g_{pK\Sigma}, && (4.180)\\
G^1_{t-born} &= -g^L, && (4.181)
\end{aligned}$$

where κ_p and κ_Λ refer to the magnetic moments of the proton and Λ respectively. The magnetic moments for both the proton and Λ and the electric charge e are well established

units. Throughout the fitting procedure, these values are fixed to

$$\kappa_p = 2.793, \tag{4.182}$$

$$\kappa_\Lambda = -0.729, \tag{4.183}$$

$$e = 0.3029, \tag{4.184}$$

in dimensionless quantities. The coupling product for Σ exchange is fixed to the value 1.4579. The only coupling that has not been very well established is $g_{pK\Lambda}$. This coupling can be related to the coupling $g_{NN\pi}$ in unbroken $SU(3)$ symmetry by [3],

$$g_{Kp\Lambda} = -\frac{1}{\sqrt{3}}(3 - 2\alpha_D)g_{\pi NN}. \tag{4.185}$$

Given that $SU(3)$ symmetry is not fully realized in nature, other theoretical models, some of which are based on photon-kaon scattering and 20% $SU(3)$ symmetry breaking effects, predict a range of values between $-4.4 \leq \frac{g_{pK\Lambda}}{\sqrt{4\pi}} \leq -3.0$ [43]. Other phenomenological models for the reaction $p(\gamma K)\Lambda$ predict a value of $\frac{g_{pK\Lambda}}{\sqrt{4\pi}}$ between -4.30 and -2.90 [44]. In addition, QCD sum rule methods predict a value close to $\frac{g_{pK\Lambda}}{\sqrt{4\pi}} = -1.96$ [13]. Given that there is a range of values reported for $g_{pK\Lambda}$ in previous studies, $g_{pK\Lambda}$ is introduced as a parameter that is allowed to vary in the fitting procedure. It will be of interest to see how the values obtained for this parameter in the present fits compare with those obtained in previous experimetally driven photoproduction models and QCD inspired models.

The additional parameters of the fit are the coupling products at the electromagnetic and strong vertices. For resonances with total angular momentum $J = \frac{1}{2}$, these parameters are defined as

$$F_{N^*} = e\kappa_{p\to N^*} g_{N^*K\Lambda},$$

$$F_{\Lambda^*} = e\kappa_{\Lambda\to\Lambda^*} g_{\Lambda^*Kp}, \tag{4.186}$$

$$F_{\Sigma^*} = e\kappa_{\Lambda\to\Sigma^*} g_{\Sigma^*Kp}. \tag{4.187}$$

For resonances with total angular momentum $J = \frac{3}{2}$ and $\frac{5}{2}$, the definitions in Section (4.1.4),

$$\begin{aligned} G^1_{N^*} &= g_1^{pN^*} g_s^3, \\ G^2_{N^*} &= g_2^{pN^*} g_s^3, \\ G^1_{\Lambda^*} &= g_1^{\Lambda\Lambda^*} g^3_{u-\Lambda^*}, \\ G^2_{\Lambda^*} &= g_2^{\Lambda\Lambda^*} g^3_{u-\Lambda^*}, \\ G^1_{\Sigma^*} &= g_1^{\Lambda\Sigma^*} g^3_{u-\Sigma^*}, \\ G^2_{\Sigma^*} &= g_2^{\Lambda\Sigma^*} g^3_{u-\Sigma^*}, \end{aligned} \tag{4.188}$$

where $g_s^3 = g_{N^*K\Lambda}$ in the s-channel, and $g^3_{u\Lambda^*,\Sigma^*} = g_{\Lambda^*,\Sigma^*Kp}$ in the u-channel, are employed. The t-channel resonance vector and tensor couplings are given by

$$\begin{aligned} G^V &= g_{\gamma KK^*} g^V_{\Lambda K^* p}, \\ G^T &= g_{\gamma KK^*} g^T_{\Lambda K^* p}, \end{aligned} \tag{4.189}$$

for $K^* = K^*(892)$ or $K^1(1270)$, respectively

The first fit is performed using the low energy portion of the CLAS unpolarized differential cross section data [9] given by Eq. (3.55) in Section (3.2). Four different sets of starting parameters, labeled sets A, B, C and D were used. A non-linear Levenberg-Marquardt method was employed to obtain the set of parameters that minimizes the χ^2_ν defined by

$$\chi^2_\nu = \frac{1}{(N - n_{par})} \sum_i^N \frac{(Y^i_{model} - Y^i_{exp})^2}{(dY^i_{\rm exp} \cdot dY^i_{exp})^2}, \tag{4.190}$$

where ν labels the number of independent degrees of feedom in the fit. The variable Y_{model} is the observable calculated using the effective lagrangian model, and Y_{exp} is the experimentally measured observable with uncertainty dY. The fit to the unpolarized cross section yields a set of paramaters for each of the starting parameter sets defined above. These new parameters were then used as starting parameters for a low energy fit to both unpolarized

differential cross section data and the double polarization observables C_x and C_z [10]. For a right circularly polarized photon , these assymetries are given by

$$C_j = \frac{d\sigma^+ - d\sigma^-}{d\sigma^+ + d\sigma^-}, \tag{4.191}$$

where $\pm$ refers to the Λ spin projection parallel or antiparallel to the $j = \hat{z}$ or $j = \hat{x}$ axes.

To fit the whole energy range from 1.6 GeV to 2.6 GeV, the resonances in Table (4.10) were incorporated. Both the unpolarized differential cross-section and polarization observables were fit in two steps using the same procedure as for the low energy data. The new parameters used in the full energy fits include the total decay widths of the less well-established resonances in Table (4.10).

The best fit obtained from the four starting parameter sets was then used to study the sensitivity of the fits to each of the nucleon higher energy resonances. This was done by first fitting the differential cross-section and asymmetries keeping all parameters associated with the resonances in Table (4.9) fixed and varying only the ones in Table (4.10). This procedure provides information on how the low energy results are affected by the high energy resonances and how well the parameters obtained from the low energy fit describe the high energy data.

A second procedure is carried out to remove the high energy resonances from the model, one by one. This was performed to study the sensitivity of the χ^2_ν to individual resonances. This procedure can in principle give insight into how much the observables depend on each of the high energy resonances and whether or not a particular resonance is relevant to the description of the experimental data.

Using the best fit to all the cross section and double polarization data, a systematic study of the contribution of u-channel hyperon resonances was performed. In particular, we studied the sensitivity of the observables to the presence or absence of u-channel resonances that do not couple strongly to the initial or final state or whose coupling products seem

unphysically high. If the shape of the distribution does not change significantly when a particular hyperon resonance is removed, an attempt is made to refit without it. Lastly, we studied the angular dependence of the differential cross-section associated with the u and t-channel contributions.

Chapter 5

Results and Discussion

The version of the isobar model developed for this study of the reaction $\gamma + p \rightarrow K^+ + \Lambda$ was discussed in Chapter 4. In particular, contributions to the reaction's amplitude were given for s and u-channel resonances with total angular momentum $J \leq \frac{5}{2}$ with both positive and negative parities. In addition, two kaon resonances were also incorporated, the $K^*(892)$ and $K^1(1270)$ resonances. A model for the decay widths for six particular decay channels for nucleon s-channel resonances was also included in the model. The results of the fits performed to the unpolarized cross section data and double polarization observables, C_x and C_z, are presented in this section. This section is divided into two main parts. The first part analyzes the sensitivity of the coupling products to the addition of double polarization data to the fitting procedure, in particular, the sensitivity of leading coupling constant $g_{pK\Lambda}$. The second part analyzes the behavior of the coupling products to two different sets of starting parameters obtained from the low energy fits.

5.1 Low Energy Fits

In the low energy regime, two different fits are presented. The first fit is performed using just the unpolarized differential cross section data for four sets of initial parameters labeled models A, B, C, and D. The results for these fits are presented in table (5.1). These results consist of the sets of parameters for which the χ^2_ν function, Eq. (4.19), is at its minimum. The occurence of global versus local minima is always a concern when data sets are fit. This is not a trivial concern since many fitting routines are generally not robust enough to

find a true minimum among several local minima. We attempted to tackle this obstacle by varying the way in which the parameters were introduced into the fitting routine. In some cases, a solution was found by first varying the s-channel parameters while keeping all other parameters fixed. Using the output parameters for this particular solution as a new set of starting parameters, the u-channel parameters were then varied to obtain a new minimum. This procedure could be altered by permutating the order in which the different parameters were varied. We also tried a scheme in which the parameters corresponding to resonances with different angular momentum-parity combinations were successively varied. The results in table (5.1) represent the parameters giving the lowest possible χ^2_ν obtained with the Levenberg-Marquardt method, for each of the four different sets of starting parameters.

The angular dependence of the differential cross section is exhibited in Fig. (5.1) at four different energies. With the exception of fit D, the quality of the four fits are similar, which reflects the similar χ^2_ν obtained with the fits.

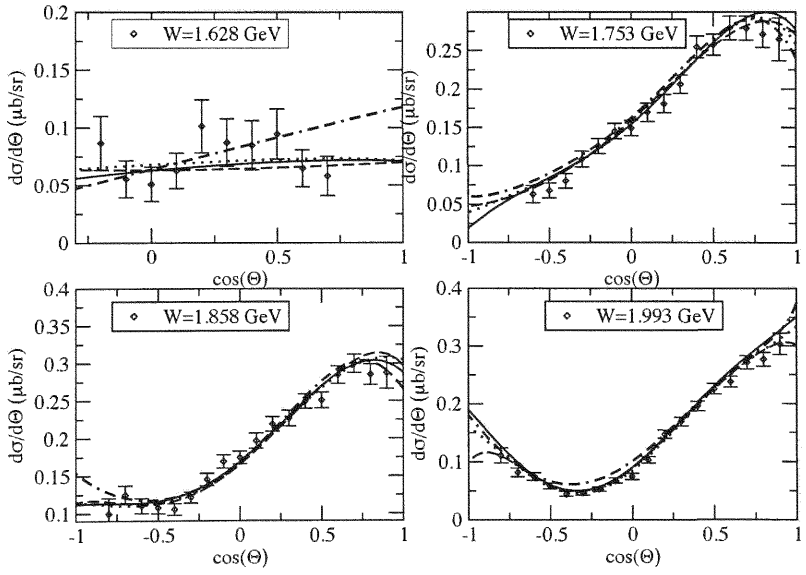

Figure 5.1: Differential cross section for the reaction $\gamma + p \rightarrow K^+ + \Lambda$ at four different total CM energies. The solid curves were obtained with fit A, the dotted curves with fit B, the dashed curves with fit C, and the dot-dashed curves with fit D.

	A		B		C		D	
				$\mathbf{F_{N^*}}$				
$N(1440)\frac{1}{2}^+$	-3.759		-3.859		-4.800		-10.411	
$N(1710)\frac{1}{2}^+$	0.080		0.054		0.185		0.233	
$N(1535)\frac{1}{2}^-$	-0.101		-0.026		-0.052		-0.533	
$N(1650)\frac{1}{2}^-$	-0.137		-0.199		-0.132		0.027	
				$\mathbf{G^1_{N^*}\ G^2_{N^*}}$				
$N(1720)\frac{3}{2}^+$	0.035	0.135	0.036	-0.016	-0.002	-0.111	0.009	0.222
$N(1520)\frac{3}{2}^-$	-1.453	-0.895	-1.794	-0.825	-0.482	-0.066	-0.593	0.143
$N(1700)\frac{3}{2}^-$	0.989	1.292	1.277	1.385	0.202	0.635	0.807	1.086
$N(1680)\frac{5}{2}^+$	0.096	0.072	0.108	0.067	0.048	0.017	0.108	0.124
$N(1675)\frac{5}{2}^-$	-0.011	-0.018	-0.015	-0.021	-0.007	-0.011	-0.013	0.018
				$\mathbf{F_{\Lambda^*}}$				
$\Lambda(1600)\frac{1}{2}^+$	-9.869		-1.108		-12.148		-5.349	
$\Lambda(1810)\frac{1}{2}^+$	0.559		3.447		-3.282		-1.299	
$\Lambda(1405)\frac{1}{2}^-$	-1.078		-1.700		1.815		-2.167	
$\Lambda(1670)\frac{1}{2}^-$	0.477		-3.859		-5.721		-1.017	
				$\mathbf{G^1_{\Lambda^*}\ G^2_{\Lambda^*}}$				
$\Lambda(1890)\frac{3}{2}^+$	2.070	-8.748	2.618	-9.868	0.215	0.102	0.063	-0.401
$\Lambda(1520)\frac{3}{2}^-$	0.505	0.963	-0.215	0.077	-0.022	0.258	0.047	-0.443
$\Lambda(1690)\frac{3}{2}^-$	9.289	-6.720	-0.466	-7.452	0.025	0.251	0.007	-0.432
$\Lambda(1820)\frac{5}{2}^+$	-0.003	0.002	-0.004	-0.004	-0.010	-0.030	0.002	0.005
$\Lambda(2110)\frac{5}{2}^+$	0.011	0.021	-0.007	0.000	-0.015	-0.021	-0.004	-0.019
$\Lambda(1830)\frac{5}{2}^-$	0.002	0.020	0.002	0.009	-0.005	0.022	-0.002	0.020
				$\mathbf{F_{\Sigma^*}}$				
$\Sigma(1660)\frac{1}{2}^+$	4.800		-6.248		5.671		3.790	
$\Sigma(1750)\frac{1}{2}^-$	3.107		10.950		6.703		-0.422	
				$\mathbf{G^1_{\Sigma^*}\ G^2_{\Sigma^*}}$				
$\Sigma(1385)\frac{3}{2}^+$	-0.410	6.481	-0.553	5.285	0.346	0.359	0.010	1.059
$\Sigma(1670)\frac{3}{2}^-$	-8.102	10.295	1.052	9.718	0.019	0.254	0.010	-0.433
$\Sigma(1940)\frac{3}{2}^-$	0.665	0.650	-0.022	-0.094	0.111	0.190	-0.002	-0.414
$\Sigma(1915)\frac{5}{2}^+$	0.002	0.008	-0.004	-0.003	-0.011	-0.027	0.000	-0.004
$\Sigma(1775)\frac{5}{2}^-$	0.003	0.012	0.002	0.007	-0.006	0.018	-0.002	-0.004
				$\mathbf{g_{pK\Lambda}}$				
	-3.410		-0.901		-4.503		-3.589	
	$\chi^2 = 1.436$		$\chi^2 = 1.262$		$\chi^2 = 1.450$		$\chi^2 = 1.861$	

Table 5.1: Low energy fit results: Unpolarized differential cross section fit.

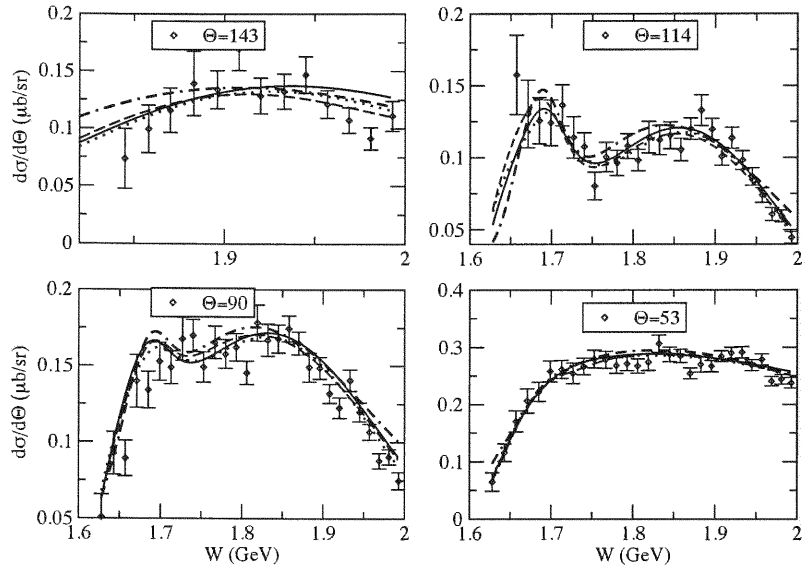

Figure 5.2: Differential cross section for the reaction $\gamma + p \rightarrow K^+ + \Lambda$ at four different Θ_{CM}. The solid curves were obtained with fit A, the dotted curves with fit B, the dashed curves with fit C, and the dot-dashed curves with fit D.

The poorer quality of fit D can be seen in the behavior of the fits at energies near threshold. While fits A, B and C appear to follow the shape of the data with the same degree of quality, fit D fails to do so near threshold, and it fails to describe the data at backward angles at all other energies. Fig. (5.2), which shows the behavior of the differential cross section as a function of energy, reinforces the fact that fit D fails to describe the data well at energies near threshold; in particular at 143°, fit D overestimates the differential cross section at all energies up to 1.9 GeV. A closer look at Table (5.1) reveals the similarities between the nucleon coupling products in fits A, B and C. This is to be expected, since the s-channel dominates the reaction amplitude; the u and t-channels provide smaller background contributions. While the s-channel parameters seem to converge to the same value from different starting parameters, the u-channel coupling products vary from fit to fit, thus depending on the different paths taken towards a χ^2_ν minima.

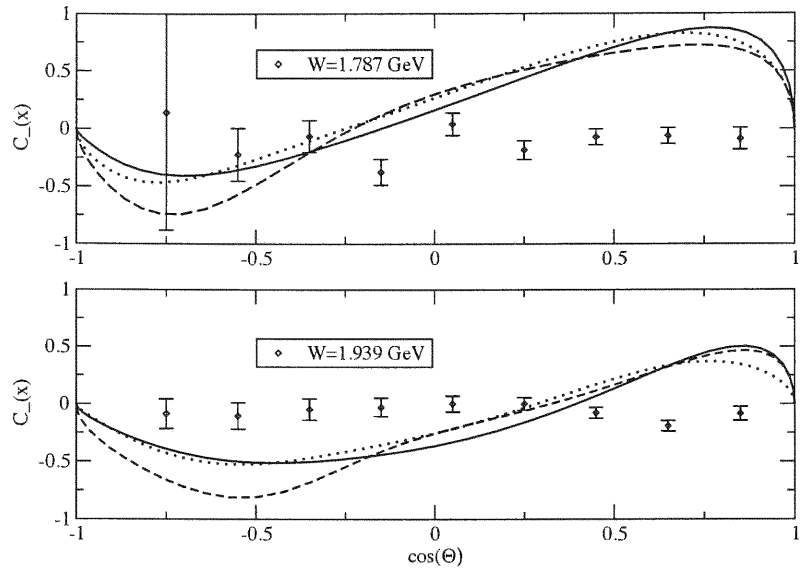

Figure 5.3: Double polarization observable C_x for the reaction $\gamma + p \rightarrow K^+ + \Lambda$ at CM energies $W = 1.787$ GeV and 1.939 GeV. The solid curves were obtained with fit A, the dotted curves with fit B, and the dashed curves with fit C.

Fig. (5.3) displays the double polarization observable C_x as a function of the CM angle for two different energies, while Fig. (5.4) displays C_z for the same two energies using the three models that seem to give reasonable fits to the unpolarized differential cross section. The models used to obtain the curves in Figs. (5.3) and (5.4), have not been fit to the polarization data. The disagreement with the data indicate that cross section data alone are not adequate enough to extract the coupling products which can entirely describe the reaction.

The second part of the low energy fitting procedure involves a fit to both cross section and polarization data using the same number of coupling product parameters as in the fit described above and using the values in Table (5.1) as starting parameters. These parameters are used as starting parameters since, with the exception of fit D, they yield qood fits to the cross section. Furthermore, there is no reason to believe that adding polarization data to the fit should cause a drastic change in the coupling products. The parameters obtained from this fit are given in table (5.2). Fits B and C have comparable

	A		B		C		D	
				$\mathbf{F_{N^*}}$				
$N(1440)\frac{1}{2}^+$	-2.316		-0.873		-1.123		-7.618	
$N(1710)\frac{1}{2}^+$	0.091		0.141		0.100		0.293	
$N(1535)\frac{1}{2}^-$	0.336		0.038		-0.010		-0.440	
$N(1650)\frac{1}{2}^-$	-0.072		-0.121		-0.083		-0.007	
				$\mathbf{G^1_{N^*}}$	$\mathbf{G^2_{N^*}}$			
$N(1720)\frac{3}{2}^+$	-0.067	-0.102	0.071	0.266	0.053	0.254	0.027	0.400
$N(1520)\frac{3}{2}^-$	-1.320	-0.916	0.288	-0.036	1.277	1.360	-0.814	0.100
$N(1700)\frac{3}{2}^-$	0.817	0.873	-0.130	-0.025	-0.396	-0.328	0.794	0.893
$N(1680)\frac{5}{2}^+$	0.092	0.092	-0.041	-0.065	-0.076	-0.098	0.110	0.123
$N(1675)\frac{5}{2}^-$	-0.012	-0.016	0.006	-0.010	0.009	0.004	-0.011	0.007
				$\mathbf{F_{\Lambda^*}}$				
$\Lambda(1600)\frac{1}{2}^+$	-8.704		-4.405		-14.211		-4.707	
$\Lambda(1810)\frac{1}{2}^+$	2.202		1.138		-5.277		-0.773	
$\Lambda(1405)\frac{1}{2}^-$	-0.769		-0.481		3.577		-2.058	
$\Lambda(1670)\frac{1}{2}^-$	1.093		-3.359		-5.792		-0.887	
				$\mathbf{G^1_{\Lambda^*}}$	$\mathbf{G^2_{\Lambda^*}}$			
$\Lambda(1890)\frac{3}{2}^+$	1.930	-8.039	2.862	-11.054	1.401	-3.262	0.100	-0.222
$\Lambda(1520)\frac{3}{2}^-$	0.354	0.510	-0.602	0.790	-0.115	0.214	0.017	-0.594
$\Lambda(1690)\frac{3}{2}^-$	9.082	-7.250	-0.562	-7.175	-0.028	0.535	-0.098	-0.572
$\Lambda(1820)\frac{5}{2}^+$	-0.007	0.001	-0.015	-0.054	-0.016	-0.022	0.007	0.000
$\Lambda(2110)\frac{5}{2}^+$	0.045	0.062	-0.016	0.031	-0.020	-0.039	-0.014	-0.029
$\Lambda(1830)\frac{5}{2}^-$	0.011	-0.005	-0.016	0.032	-0.019	0.064	-0.003	0.007
				$\mathbf{F_{\Sigma^*}}$				
$\Sigma(1660)\frac{1}{2}^+$	6.138		-9.198		3.643		4.338	
$\Sigma(1750)\frac{1}{2}^-$	3.797		11.254		6.170		-0.286	
				$\mathbf{G^1_{\Sigma^*}}$	$\mathbf{G^2_{\Sigma^*}}$			
$\Sigma(1385)\frac{3}{2}^+$	-0.171	6.101	-1.225	6.002	-0.695	2.178	0.046	1.105
$\Sigma(1670)\frac{3}{2}^-$	-8.300	9.774	0.925	10.049	-0.043	0.537	-0.085	-0.574
$\Sigma(1940)\frac{3}{2}^-$	0.281	0.012	0.163	-0.522	0.094	0.547	-0.231	-0.535
$\Sigma(1915)\frac{5}{2}^+$	0.011	0.023	-0.015	-0.025	-0.017	-0.031	0.000	-0.011
$\Sigma(1775)\frac{5}{2}^-$	0.014	0.000	-0.002	0.016	-0.007	0.005	-0.003	-0.013
				$\mathbf{g_{pK\Lambda}}$				
	1.994		2.460		-1.380		-0.558	
	$\chi^2 = 2.192$		$\chi^2 = 1.447$		$\chi^2 = 1.500$		$\chi^2 = 2.059$	

Table 5.2: Low energy fit results: Unpolarized differential cross section and double polarization asymmetries C_x and C_z fit.

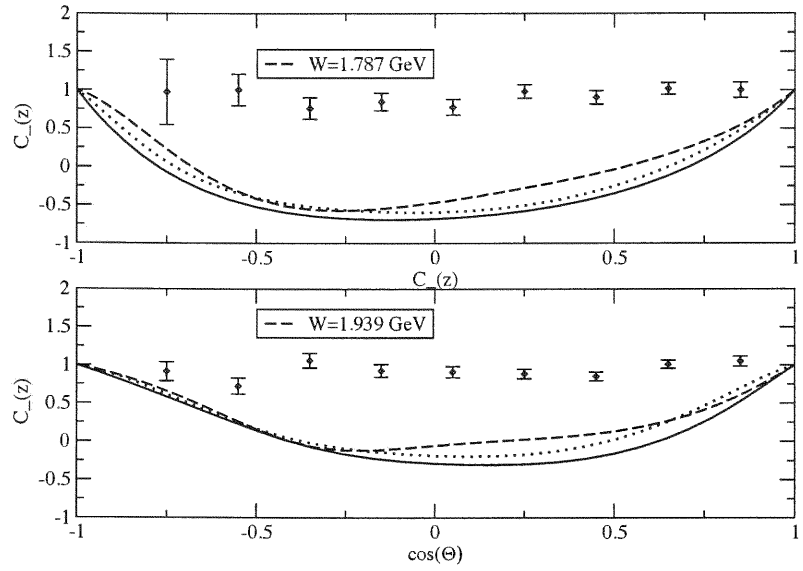

Figure 5.4: Double polarization observable C_z for the reaction $\gamma + p \rightarrow K^+ + \Lambda$ at CM energies $W = 1.787$ GeV and 1.939 GeV. The solid curves were obtained with fit A, the dotted curves with fit B, and the dashed curves with fit C.

χ^2_ν as can be seen by comparing the two fits in Fig. (5.5) at energies near threshold. It is clear from Figs. (5.5) and (5.6) that fit C yields a better description of the data than fit B. In particular, the energy distribution in Fig. (5.6) at 90° clearly shows that the parameters in fit B overestimate the data, while fit C seems to agree well at both forward and backward angles. The situation is different at more forward angles, such as 53°, where fits A, C, and D have comparable quality. It appears that the coupling parameters are more sensitive to cross sectional data at angles greater than 90°. Fits A and D do not yield good representations of the data at low energies and back angles, as is evident from their higher χ^2_ν.

Carefully comparing the parameters in Tables (5.1) and (5.2) for fit C, reveals a well ordered change in the parameters after polarization data is incorporated into the fit. Of particular interest is the fact that after inclusion of polarization data, all s-channel spin $\frac{1}{2}$ resonance parameters decreased in magnitude, with the exception of the $N^*(1535)$, while the u-channel spin $\frac{1}{2}$ coupling products increased, with the exception of both spin $\frac{1}{2}$ Σ resonances, $\Sigma^*(1660)$ and $\Sigma^*(1750)$. Fits A, B, and D did not exhibit this behavior. In

addition, it is worth noting that the behavior of the fitting parameters for resonances with angular momentum greater than $\frac{3}{2}$ showed no significant change in magnitude when polarization data were included for all four sets. This might be be due to the fact that these parameters are not very sensitive to the observables included in the fitting procedure. The fluctuations appeared to be random, but rather small. The following section addresses this issue, where cross-section and polarization data for energies up to 2.6 GeV will be included in the fits.

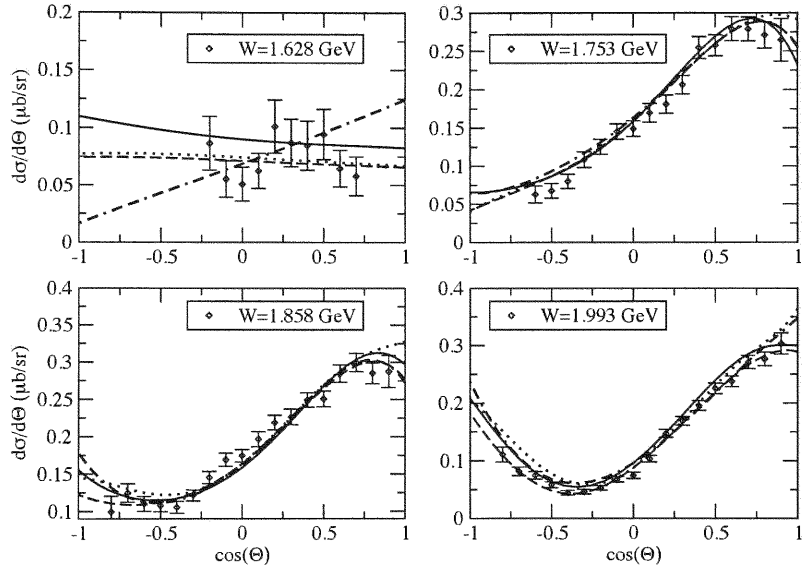

Figure 5.5: Differential cross section for the reaction $\gamma + p \rightarrow K^+ + \Lambda$ at four different total CM energies. The solid curves were obtained with fit A, the dotted curves with fit B, the dashed curves with fit C, and the dot-dashed curves with fit D.

It thus appears that polarization data have laid down certain constraints on the behavior of the coupling parameters and discriminate between different fits. This is shown by the angular distributions of the double polarization C_x and C_z depicted in Figs. (5.7) and (5.8) respectively for energies 1.787 GeV and 1.939 GeV. Again, fits B, and C fit C_x and C_z well at forward angles, in particular near threshold at 1.787 GeV and even better near 2 GeV. At back angles, fit C seems to be preferred over fit B, especially at $W = 1.939$ GeV, where fit B underestimates C_x for all back angles. Another interesting observation is that

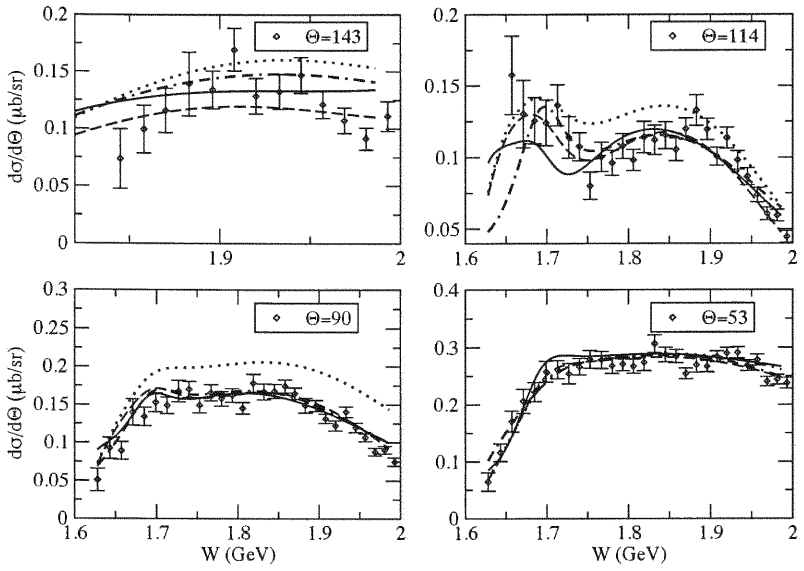

Figure 5.6: Differential cross section for the reaction $\gamma + p \rightarrow K^+ + \Lambda$ at four different total CM energies. The solid curves were obtained with fit A, the dotted curves with fit B, the dashed curves with fit C, and the dot-dashed curves with fit D.

at energies near 2.0 GeV, all fits seem to do well. It is at low energies that the fits become distinguishable with one fit preferred over the other, as shown by the shape of the curves in Figs. (5.5) and (5.6) for the cross section, and Figs. (5.7) and (5.8) for the asymmetries. It seems that at energies near 2 GeV, there exist many different combinations of parameters that could lead to a low χ^2_ν. In particular, It may well be that the addition of high energy resonances may improve some of the low energy fits more than others. The similarities between the four sets of fits in the 2 GeV region are also evident from Figs. (5.9) and (5.10), which depict both C_x and C_z as a function of the CM energy for backward and forward angles.

At first glance, one would be inclined to disregard any parameter sets for which the Born coupling parameter $g_{pK\Lambda}$ is positive at the χ^2_ν minimum. The value has not yet been definately determined, but as discussed in Section (4.4), various studies seem to agree on its sign. Since fit B seemed to be of comparable quality to fit C, a second fitting procedure was conducted for fit B, as well as for fit A. In particular, a physical constraint was included in the fitting procedure.

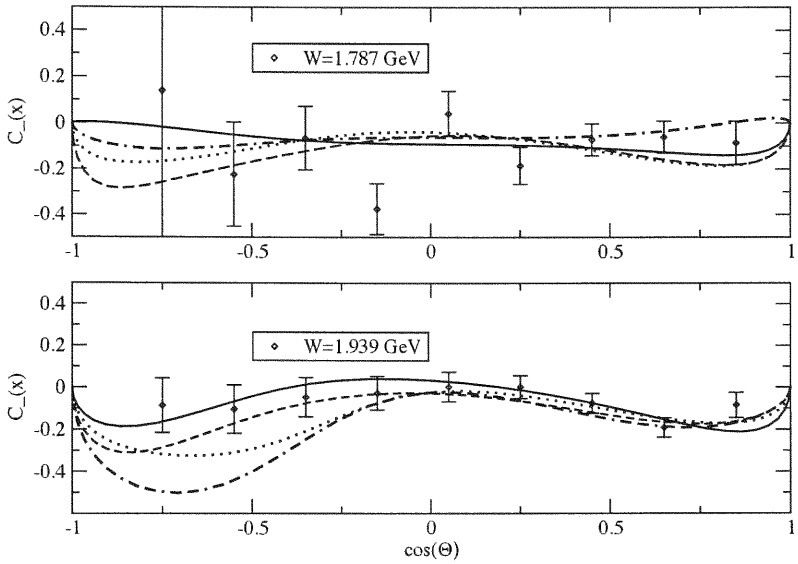

Figure 5.7: Double polarizations observables C_x for the reaction $\gamma + p \rightarrow K^+ + \Lambda$ at two different CM energies. The solid curves were obtained with fit A, the dotted curves with fit B, the dashed curves with fit C, and the dot-dashed curves with fit D.

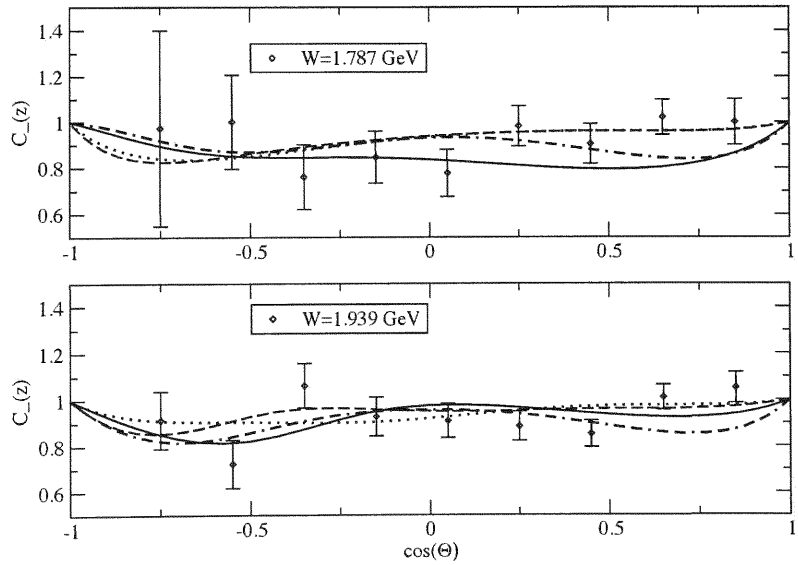

Figure 5.8: Double polarization observable C_z for the reaction $\gamma + p \rightarrow K^+ + \Lambda$ at two different CM energies. The solid curves were obtained with fit A, the dotted curves with fit B, the dashed curves with fit C, and the dot-dashed curves with fit D.

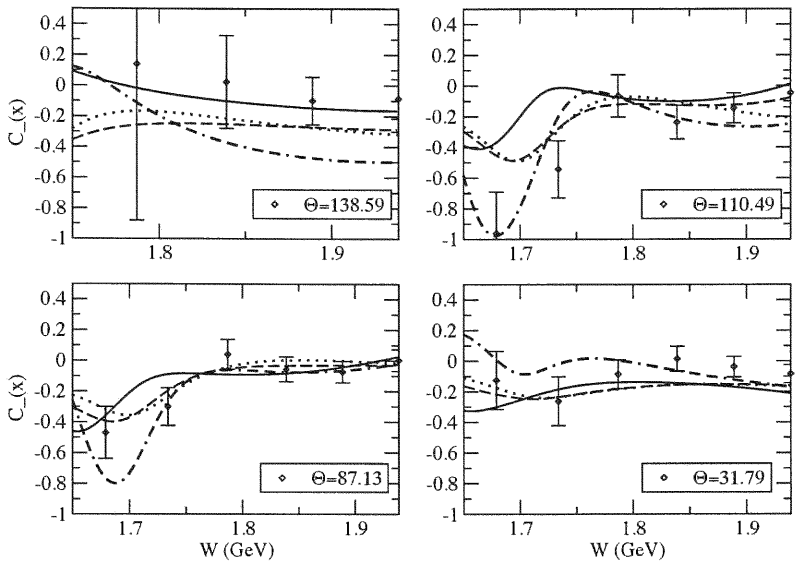

Figure 5.9: Double polarization observable C_x for the reaction $\gamma + p \rightarrow K^+ + \Lambda$ for four CM scattering angles, Θ_{CM}. The solid curves were obtained with fit A, the dotted curves with fit B, the dashed curves with fit C, and the dot-dashed curves with fit D.

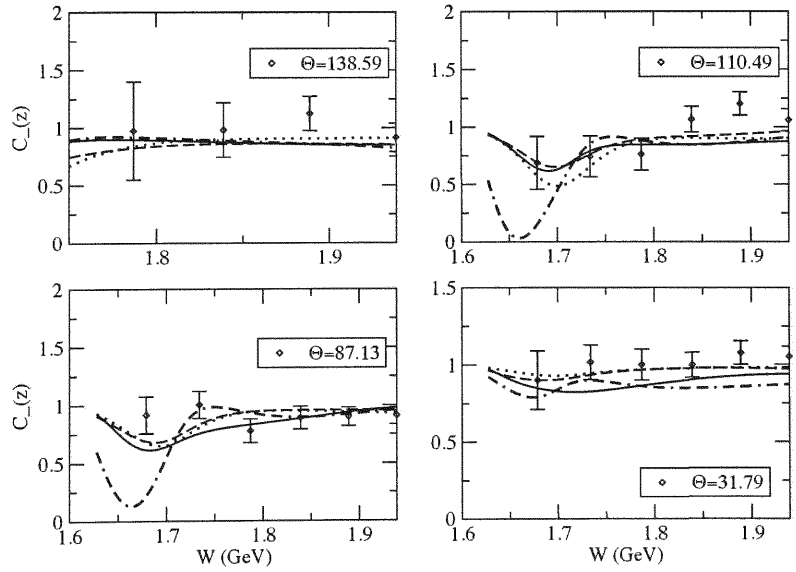

Figure 5.10: Double polarization observable C_z for the reaction $\gamma + p \rightarrow K^+ + \Lambda$ for four CM scattering angles, Θ_{CM}. The solid curves were obtained with fit A, the dotted curves with fit B, the dashed curves with fit C, and the dot-dashed curves with fit D.

The variation sampled different topological regions of the fitting function to search for a new minima for which $g_{pK\Lambda}$ is negative. The parameters given in Table (5.1) were used as strating parameteres for these fits, since they correspond to minima different from those obtained from the parameters in Table (5.2) for which $g_{pK\Lambda}$ are larger than zero. The resulting fits did not yield a lower χ^2_ν than those for which the resulting value of $g_{pK\Lambda}$ was positive. In particular, constraining the value of the Born coupling in the fits yielded a χ^2_ν of 12.05 for set A, and 2.889 for set B. Furthermore, the values of the Born couplings resulting from these two fits were very close to zero. Clearly, reasonable values of χ^2_ν are not comparable with the negative values of $g_{pK\Lambda}$ in these two fits.

Fit C appears to yield a set of parameters that better describe the experimental data, but one needs to examine the uncertainties in the fit parameters, particularly in the u-channel, before drawing any conclusions concerning the quality of the fit. In order to understand the contributions of the u-channel resonances to the fit, a series of fits was conducted, using as starting parameters the set C parameters in Table (5.1), in which different sets of u-channel parameters were successively varied. The incorporation of u-channel resonances in a controlled manner was used to study the effects of these resonances on the observables as well as reveal any correlations between s and u-channel parameters. Table (5.3) lists the values of the s-channel parameters and their uncertainties obtained for fixed values of the u-channel parameters. Figure (5.11) depicts the unpolarized differential cross section as a function of the CM scattering angle at four different energies, and Figs. (5.12) and (5.13) depict C_x and C_z at four scattering CM angles. The dashed lines indicate the uncertainty of the fit which is associated with the uncertainties in the parameters. The uncertainty in the fit can be expressed by

$$\sigma^2_{y(x_1,x_2)} = \sum_{i,j} \left(\frac{\partial y(x_1,x_2)\partial y(x_1,x_2)}{\partial a_i \partial a_j}\right)\sigma^2_{a_i a_j}, \tag{5.1}$$

where y indicates the observable at energy x_1 and scattering angle x_2 respectively, and $\sigma_{a_i a_j}$ represents the variance for $i = j$ and covariance for $i \neq j$ in the fit parameters.

	F_{N^*}	
$N(1440)\frac{1}{2}^+$	-2.267 ± 0.036	
$N(1710)\frac{1}{2}^+$	0.153 ± 0.016	
$N(1535)\frac{1}{2}^-$	0.053 ± 0.045	
$N(1650)\frac{1}{2}^-$	-0.145 ± 0.012	
	$G^1_{N^*}$	$G^2_{N^*}$
$N(1720)\frac{3}{2}^+$	0.078 ± 0.007	0.164 ± 0.023
$N(1520)\frac{3}{2}^-$	0.872 ± 0.192	1.550 ± 0.239
$N(1700)\frac{3}{2}^-$	-0.088 ± 0.039	-0.188 ± 0.061
$N(1680)\frac{5}{2}^+$	-0.034 ± 0.004	-0.072 ± 0.005
$N(1675)\frac{5}{2}^-$	0.004 ± 0.001	0.000 ± 0.001
	$G^V_{K^*}$	$G^T_{K^*}$
$K^*(892)$	-1.609 ± 0.075	3.044 ± 0.202
$K^1(1270)$	-1.562 ± 0.157	7.034 ± 0.321
	$g_{pK\Lambda}$	
	-3.803	
	$\chi^2 = 2.091$	

Table 5.3: Low energy fit results: s and t-channel parameters with u-channel parameters fixed starting with set C in Table (5.1).

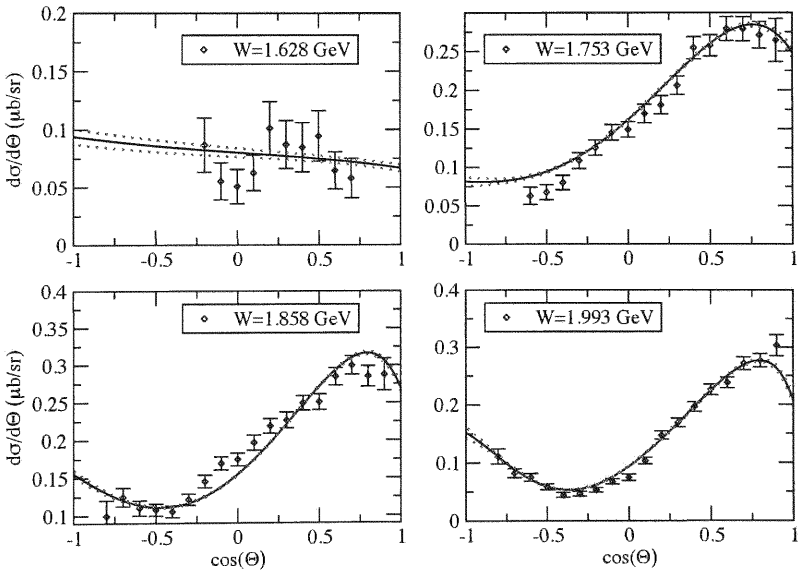

Figure 5.11: Unpolarized differential cross section for the reaction $\gamma + p \rightarrow K^+ + \Lambda$ at four CM energies. The solid curves were obtained using the parameters in Table (5.3). The dotted curves represent the uncertainty in the fit.

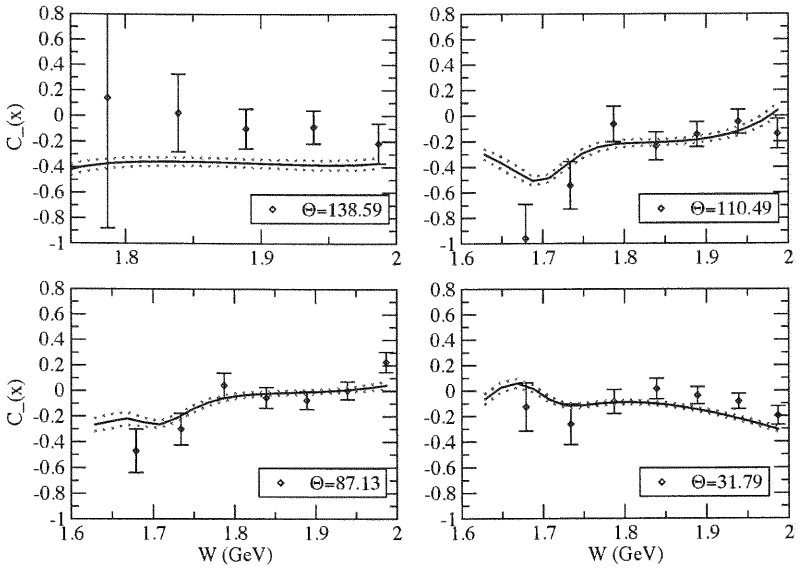

Figure 5.12: Aymmetry C_x for the reaction $\gamma + p \rightarrow K^+ + \Lambda$ at four scattering angles, Θ_{CM}. The solid curves were obtained using the parameters in Table (5.3). The dotted curves represent the uncertainty in the fit.

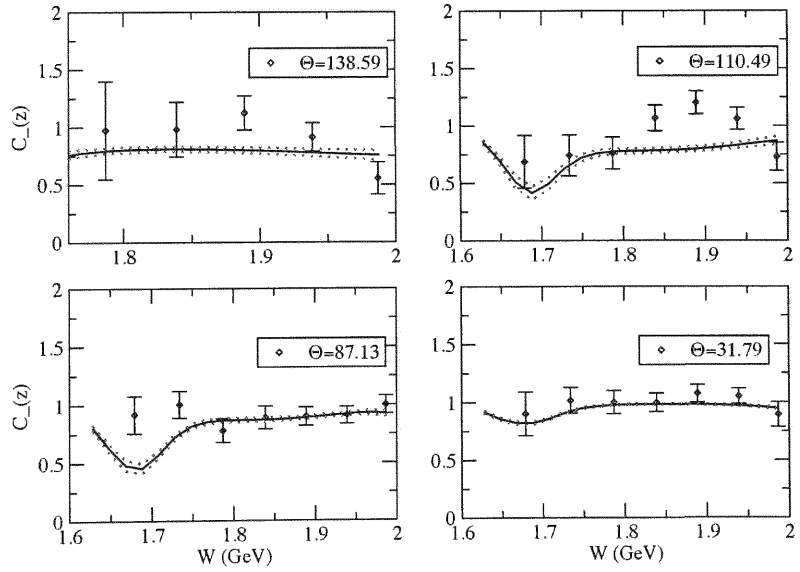

Figure 5.13: Aymmetry C_z for the reaction $\gamma + p \rightarrow K^+ + \Lambda$ at four scattering angles, Θ_{CM}. The solid curves were obtained were obtained using the parameters in Table (5.3). The dotted curves represent the uncertainty in the fit.

Figures (5.5) and (5.11) were obtained from fits performed using the same set of starting parameters, those given in Table (5.1). As seen in Fig. (5.11), fixing the u-channel parameters yielded a cross section of comparable quality to the fit obtained with all u-cahnnel parameters varied, although the χ^2_ν obtained is somewhat larger. Furthermore, the uncertainties associated with the fit when only s-channel parameters are varied were relatively small; that is, the fit seemed to be well determined by the data. The polarization observables did not seem to be affected when the u-channel parameters were fixed. In particular, this can be seen by comparing Figs. (5.9) and (5.12). It is evident that fixing the values of the u-channel parameters affects the fits for C_x at back angles, but the uncertainty band appears to extend just enough to yield a good quality fit at energies above 1.7 GeV, with the exception of the energy distribution at $\Theta_{CM} = 138.59$.

Using Table (5.3) as starting parameters for the s-channel, a fit was performed in which the $J = \frac{1}{2}$ u-channel parameters were allowed to vary. The resulting s-channel coupling strengths with their uncertainties are given in Table (5.4). Direct comparison of Tables

	F_{N^*}	
$N(1440)\frac{1}{2}^+$	-2.500 ± 0.601	
$N(1710)\frac{1}{2}^+$	0.164 ± 0.019	
$N(1535)\frac{1}{2}^-$	0.092 ± 0.055	
$N(1650)\frac{1}{2}^-$	-0.157 ± 0.012	
	$G^1_{N^*}$	$G^2_{N^*}$
$N(1720)\frac{3}{2}^+$	0.066 ± 0.010	0.170 ± 0.024
$N(1520)\frac{3}{2}^-$	1.003 ± 0.253	1.832 ± 0.306
$N(1700)\frac{3}{2}^-$	-0.169 ± 0.055	-0.363 ± 0.077
$N(1680)\frac{5}{2}^+$	-0.044 ± 0.008	-0.081 ± 0.012
$N(1675)\frac{5}{2}^-$	0.003 ± 0.002	-0.001 ± 0.003
	$G^V_{K^*}$	$G^T_{K^*}$
$K^*(892)$	-1.530 ± 0.361	3.224 ± 0.510
$K^1(1270)$	-1.086 ± 0.904	7.267 ± 0.900
	$g_{pK\Lambda}$	
	-3.450 ± 0.372	
	$\chi^2 = 2.010$	

Table 5.4: Low energy fit results: s and t-channel parameters from fits that include variations of $J = \frac{1}{2}$ u-channel parameters

(5.3) and (5.4) reveals small fluctuations in the s-channel parameters. In addition, the Born coupling strength decreases with the inclusion of the $J = \frac{1}{2}$ u-channel resonances. At

this point, an interesting remark must be made. The variation of spin $\frac{1}{2}$ u-channel resonance parameters does in fact decrease the χ^2_ν of the fit, but the uncertainties associated with these resonances are extremely high. These parameters are given in Table (5.5). Large uncertainties clearly show that the parameters are not unique and that they mainly depend on the starting parameters that define the path towards a χ^2_ν minimization. Figure (5.14)

	F_{Λ^*}
$\Lambda(1600)\frac{1}{2}^+$	-12.381 ± 682.63
$\Lambda(1810)\frac{1}{2}^+$	-2.933 ± 371.05
$\Lambda(1405)\frac{1}{2}^-$	1.795 ± 23.86
$\Lambda(1670)\frac{1}{2}^-$	-5.533 ± 183.08
	F_{Σ^*}
$\Sigma(1660)\frac{1}{2}^+$	$5.602 \pm -$
$\Sigma(1750)\frac{1}{2}^+$	6.967 ± 164.36

Table 5.5: $J = \frac{1}{2}$ u-channel parameters and uncertainties

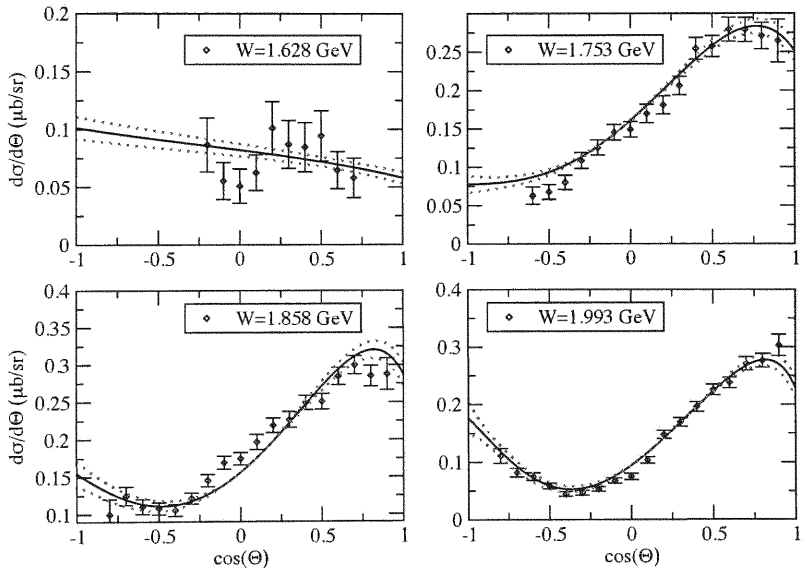

Figure 5.14: Unpolarized differential cross section for the reaction $\gamma + p \rightarrow K^+ + \Lambda$ at four CM energies. The solid curves were obtained using the paramteters in Tables (5.4) and (5.5). The dotted curves represent the uncertainty on the fit due to uncertainties in the parameters.

depicts the differential cross section obtained from the parameters in Tables (5.4) and (5.5). There is no clear difference in the qualities of the fits as compared with those in Fig. (5.11), again indicating that the differential cross section seems not to be affected by variation of

the spin $\frac{1}{2}$ u-channel contributions. Figures (5.15) and (5.16) depict the C_x and C_z polarization observables obtained from the parameters in Tables (5.4) and (5.5). Varying the spin $\frac{1}{2}$ u-channel resonances yields a better fit to both asymmetries at back angles. It is interesting to note that the high uncertainties in the spin $\frac{1}{2}$ u-channel parameters does not give rise to large uncertainties in the fit. This is due to the high degree of correlation between the parameters in the fit. The large uncertainties in the u-channel parameters indicate that the model is not highly sensitive to spin $\frac{1}{2}$ u-channel resonances, and thus, it is unlikely that the corresponding couplings can be significantly constrained by the photoproduction data.

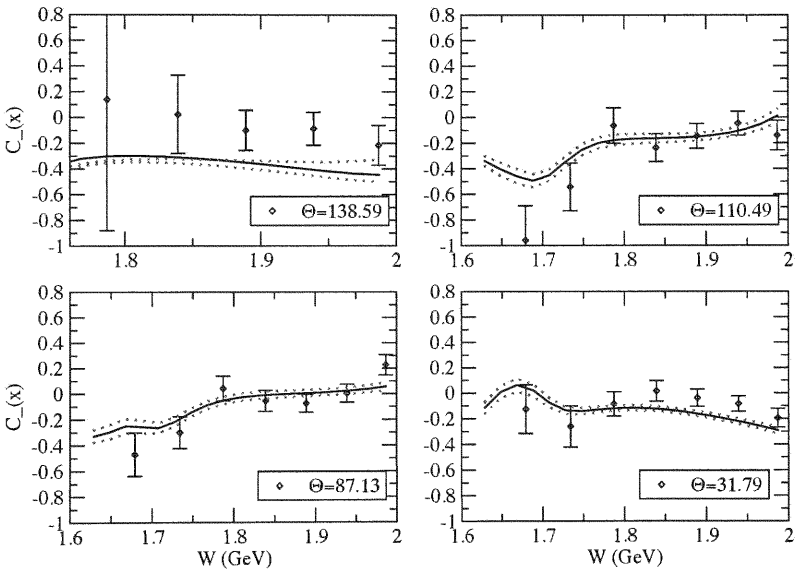

Figure 5.15: Aymmetry C_x for the reaction $\gamma + p \rightarrow K^+ + \Lambda$ at four scattering angles, Θ_{CM}. The solid curves were obtained using the parameters in Tables (5.4) and (5.5). The dotted curves represent the uncertainty in the fit.

Parameters associated with u-channel spin $\frac{3}{2}$ and $\frac{5}{2}$ resonances were also varied in the fitting procedure. These parameters behaved in the same manner as those associated with the spin $\frac{1}{2}$ u-channel resonances, that is, the parameters obtained had large uncertainties. This indicates that the model is also not very sensitive to $J = \frac{3}{2}$ and $J = \frac{5}{2}$ u-channel parameters. The higher angular momentum u-channel parameters appear also to be highly

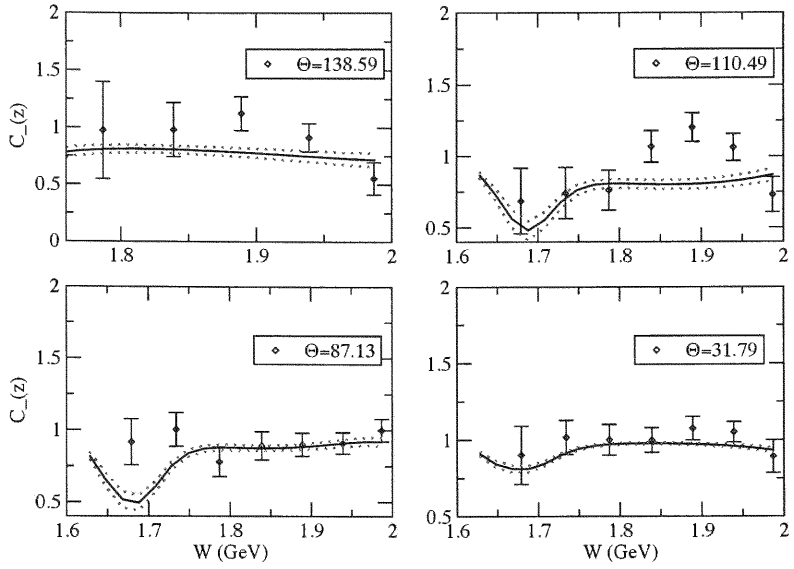

Figure 5.16: Aymmetry C_z for the reaction $\gamma + p \rightarrow K^+ + \Lambda$ at four scattering angles, Θ_{CM}. The solid curves were obtained using the parameters in Tables (5.4) and (5.5). The dotted curves represent the uncertainty on the fit due to uncertainties in the parameters.

correlated with all other parameters, which resulted in extremely low uncertainties in the fits. In particular, varying the parameters associated with spin $\frac{3}{2}$ and $\frac{5}{2}$ u-channel resonances did not cause large effects on the s and t-channel parameters, but played a major role in significanly increasing the uncertainties associated with the s and t-channel parameters, given in Table (5.6). Furthermore, the value of the born coupling obtained by varying all u-channel parameters was smaller in magnitude when compared to the born couplings in Tables (5.3) and (5.4).

In light of the large uncertainties associated with the u-channel parameters, we were motivated to eliminate those resonances with very large uncertainties and refit the cross section and polarization observables without significantly increasing the χ^2_ν. The particular u-channel resonances eliminated in this fitting procedure, which yielded the lowest χ^2_ν, are listed in Table (5.7).

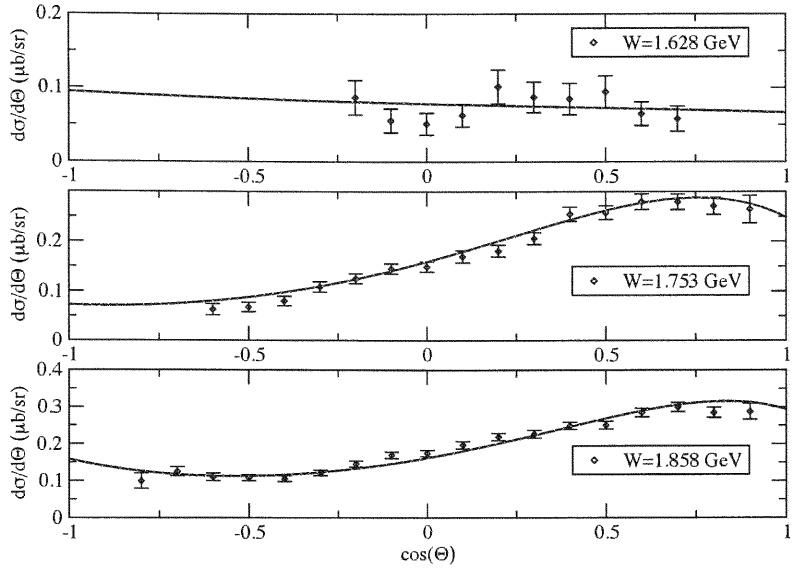

Figure 5.17: Unpolarized differential cross section for the reaction $\gamma + p \rightarrow K^+ + \Lambda$ at four CM energies. The solid curves were obtained using the s-channel parameters in Table (5.6). The dotted curves represent the uncertainty in the fit.

	$\mathbf{F_{N^*}}$	
$N(1440)\frac{1}{2}^+$	-2.400 ± 0.742	
$N(1710)\frac{1}{2}^+$	0.171 ± 0.026	
$N(1535)\frac{1}{2}^-$	0.080 ± 0.076	
$N(1650)\frac{1}{2}^-$	-0.136 ± 0.023	
	$\mathbf{G^1_{N^*}}$	$\mathbf{G^2_{N^*}}$
$N(1720)\frac{3}{2}^+$	0.056 ± 0.013	0.169 ± 0.055
$N(1520)\frac{3}{2}^-$	1.296 ± 0.331	1.787 ± 0.423
$N(1700)\frac{3}{2}^-$	-0.288 ± 0.119	-0.369 ± 0.136
$N(1680)\frac{5}{2}^+$	-0.053 ± 0.013	-0.100 ± 0.016
$N(1675)\frac{5}{2}^-$	0.0036 ± 0.003	0.000 ± 0.005
	$\mathbf{G^V_{K^*}}$	$\mathbf{G^T_{K^*}}$
$K^*(892)$	-1.236 ± 1.535	2.408 ± 1.408
$K^1(1270)$	-0.287 ± 5.256	6.824 ± 7.076
	$\mathbf{g_{pK\Lambda}}$	
	-2.664 ± 1.562	
	$\chi^2 = 1.870$	

Table 5.6: Low energy fit results: s and t-channel parameters from fits that include variations of $J = \frac{1}{2}$ and $J = \frac{3}{2}$ u-channel parameters

u-channel		
Mass (MeV)	Isospin I	J^p
$\Lambda^*(1600)$	0	$\frac{1}{2}^+$
$\Lambda^*(1810)$	0	$\frac{1}{2}^+$
$\Lambda^*(1520)$	0	$\frac{3}{2}^-$
$\Lambda^*(1690)$	0	$\frac{5}{2}^-$
$\Sigma^*(1660)$	1	$\frac{1}{2}^+$
$\Sigma^*(1750)$	1	$\frac{1}{2}^-$
$\Sigma^*(1670)$	1	$\frac{3}{2}^-$
$\Sigma^*(1940)$	1	$\frac{3}{2}^-$

Table 5.7: u-channel resonances eliminated in the new low energy fit

The χ^2_ν of this fit was 2.004 as compared to 1.500 given by the fit in Table (5.2) incorporating all u-channel parameters. The angular distribution shown in Fig. (5.18) is of comparable quality to that shown in Fig. (5.5). Furthermore, the CM energy distributions shown in Fig. (5.20) exhibit the same behavior of the cross section at energies near 1.9 GeV and $\Theta_{CM} = 114°$ as in Fig. (5.6). The polarization data seem to be well described within the uncertainties except again at forward angles where the fit falls short in the neighborhood of 1.9 GeV, as shown in Fig. (5.19).

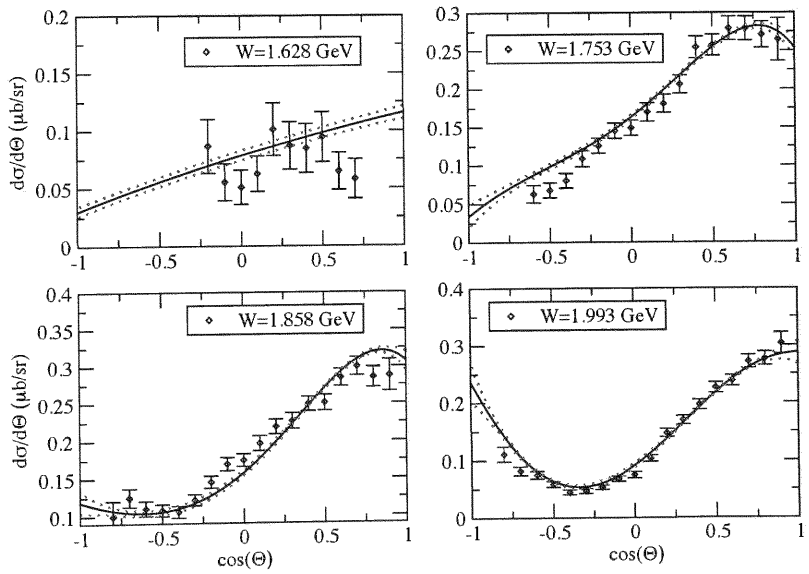

Figure 5.18: Unpolarized differential cross section for the reaction $\gamma + p \rightarrow K^+ + \Lambda$ at four CM energies. The solid curves were obtained using the parameters listed in Tables (5.8) and (5.9). The dotted curves represent the uncertainty in the fit.

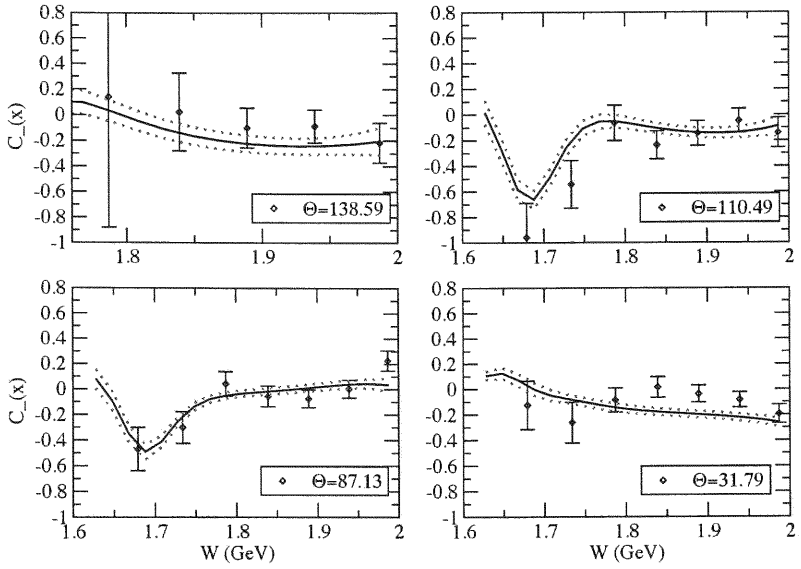

Figure 5.19: CM energy distrbution for the observable C_x. The solid curves were obtained using the parameters listed in Tables (5.8) and (5.9). The dotted curves represent the uncertainty in the fit.

The s and t-channel parameters are listed in Table (5.8) and the remaining u-channel parameters in Table (5.9). Reducing the number of u-channel parameters did not significantly affect the quality of the fits, despite the larger χ^2_ν, but the uncertainties associated with the remaining u-channel coupling strengths are considerably smaller than those obtained in Table (5.5). The s and t-channel parameters were not significantly affected by reducing the number of u-channel resonances incorporated in the fit; in particular, values for the $J = \frac{1}{2}$ parameters were always shifted by amounts within their uncertainties as obtained in fits that incorporated all the u-channel parameters, such as those given in Tables (5.2) and (5.6).

This careful analysis of the set C parameters enabled us to determine the degree of sensitivity that the model has to s and t-channel parameters. The study also revealed the effect that u-channel parameters have on both the s and t-channel coupling strengths. It was noted that variation of the parameters associated with the u-channel resonances did not cause significant variations in the s and t-channel coupling strengths, but their inclusion did

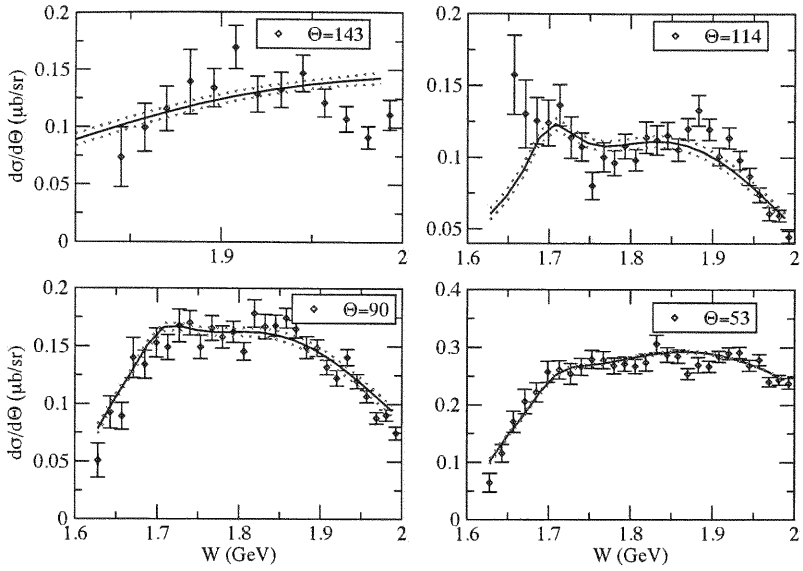

Figure 5.20: Unpolarized differential cross section for the reaction $\gamma + p \rightarrow K^+ + \Lambda$ at four CM scattering angles Θ_{CM}. The solid curves were obtained using the parameters listed in Tables (5.8) and (5.9). The dotted curves represent the uncertainty in the fit.

	$\mathbf{F_{N^*}}$	
$N(1440)\frac{1}{2}^+$	-3.100 ± 0.552	
$N(1710)\frac{1}{2}^+$	0.079 ± 0.029	
$N(1535)\frac{1}{2}^-$	-0.340 ± 0.110	
$N(1650)\frac{1}{2}^-$	-0.028 ± 0.025	
	$\mathbf{G^1_{N^*}}$	$\mathbf{G^2_{N^*}}$
$N(1720)\frac{3}{2}^+$	0.031 ± 0.017	0.170 ± 0.037
$N(1520)\frac{3}{2}^-$	-1.521 ± 0.203	-0.795 ± 0.428
$N(1700)\frac{3}{2}^-$	0.768 ± 0.102	0.855 ± 0.143
$N(1680)\frac{5}{2}^+$	0.086 ± 0.010	0.071 ± 0.012
$N(1675)\frac{5}{2}^-$	-0.010 ± 0.002	-0.022 ± 0.006
	$\mathbf{G^V_{K^*}}$	$\mathbf{G^T_{K^*}}$
$K^*(892)$	0.450 ± 0.978	-2.396 ± 2.101
$K^1(1270)$	-0.527 ± 1.535	3.823 ± 7.286
	$\mathbf{g_{pK\Lambda}}$	
	-0.667 ± 1.437	
	$\chi^2 = 2.004$	

Table 5.8: s and t-channel parameters obtained from a fit which excluded parameters associated with the u-channel resonances in Table (5.7).

	F_{Λ^*}	
$\Lambda(1405)\frac{1}{2}^-$	1.787 ± 25.356	
$\Lambda(1670)\frac{1}{2}^-$	-6.880 ± 32.879	
	$G^1_{\Lambda^*}$	$G^2_{\Lambda^*}$
$\Lambda(1890)\frac{3}{2}^+$	-0.048 ± 3.345	-1.175 ± 26.610
$\Lambda(1820)\frac{5}{2}^+$	0.016 ± 2.276	-0.022 ± 8.855
$\Lambda(2110)\frac{5}{2}^+$	-0.011 ± 1.852	0.035 ± 6.340
$\Lambda(1830)\frac{5}{2}^-$	0.003 ± 0.643	-0.014 ± 3.671
	$G^1_{\Sigma^*}$	$G^2_{\Sigma^*}$
$\Sigma(1385)\frac{3}{2}^+$	-0.093 ± 2.262	2.166 ± 17.562
$\Sigma(1915)\frac{5}{2}^+$	0.0052 ± 4.036	0.001 ± 15.009
$\Sigma(1775)\frac{5}{2}^-$	-0.000 ± 0.608	-0.012 ± 3.516

Table 5.9: u-channel parameters obtained from a fit which excluded parameters associated with the u-channel resonances in Table (5.7).

increase the magnitude of the s and t-channel parameter uncertainties. It was also noted that even though spin $\frac{1}{2}$ u-channel parameters are not unique within this isobar approach, due to large uncertainties in their values, they are highly correlated to the other parameters in the model. This behavior was also evident for higher angular momentum u-channel states. Lastly, it should be noted that s-channel spin $\frac{5}{2}$ resonances appear to couple very weakly to the $K\Lambda$ channel at the energies considered here. This result is obvious in all four fits A, B, C, and D. It is possible that fits to higher energy data may require stronger coupling to the $K\Lambda$ channel for these resonances, and thus they should be included in higher energy fits.

5.2 High Energy Fits

The behavior of the model at high energies was studied using the low energy parameters obtained from the best fit to the low energy data and four less well-established resonances, which appear with a two star status in the Particle Data Tables [18]. As discussed in the introduction, two spin $\frac{3}{2}$ resonances are included in these fits, which are shown to play an important role in the description of the data in the 1.9 GeV energy region. The negative parity $D_{13}(2080)$ has been discussed in connection with the missing resonance problem by Benhold and Mart [20, 21] and seems to play an important role in the analysis perfomed by Sarantsev [19]. The positive parity $P_{13}(1900)$ has been predicted by relativistic quark

models [22]. It is not yet clear which structure has a dominant contribution in this energy region. In addition, two spin $\frac{5}{2}$ resonances are included, a positve parity state at 2000 MeV and a negative parity state at 2200 MeV, also predicted by relativistic quark models [22].

Figure (5.21) depicts the unpolarized differential cross section as a function of the CM energy at $\Theta_{CM} = 90°$ using only the low energy parameters given in Tables (5.8) and (5.9). It is evident from Fig. (5.21) that parameters obtained from fits to low energies cannot accurately describe the behavior of the reaction at energies beyond 2 GeV. In particular, the model underestimates the cross section at energies around 1.9 GeV, and diverges beyond 2.1 GeV. The divergent behavior is clearly an effect due to the absence of high energy data in the fits used to obatain the parameters listed in Tables (5.8) and (5.9), as well as the absence of higher mass resonances.

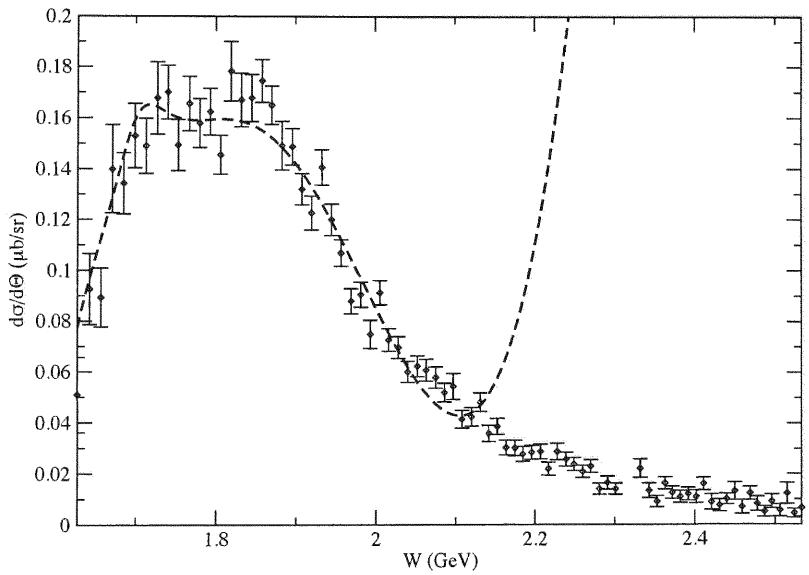

Figure 5.21: Unpolarized differential cross section for the reaction $\gamma + p \rightarrow K^+ + \Lambda$ at $\Theta_{CM} = 90°$. The dashed curves were obtained using the parameters listed in Tables (5.8) and (5.9)

An attempt to fit the cross section using as starting parameters the values listed in Tables (5.8) and (5.9) was also carried out. The parameters obtained from this fit are listed in Tables (5.10) and (5.11). The coupling products of the resonances with masses above 1.6 GeV increased in magnitude when compared to the values listed in Table (5.8), while those associated with the $N^*(1405)$ and $N^*(1535)$ decreased. It appears that the inlcusion of higher energy into the fitting procedure affects resonances with heavier masses, since they lie closer to the energy range in consideration. In particular, incorporating higher energy data into the fitting procedure did not significantly affect the strength of the s-channel resonances introduced in the previous section, where most of the time the parameters lsited in Table (5.11) lied within the uncertainties associated with the resonance couplings listed in Table (5.8). This result and the higher value of the χ^2_ν associated with this fit, suggests that higher energy resonances are to be incorporated into the model for a better description of the experimental data. In addition, the coupling products associated with the u-channel resonances listed in Table (5.12) did not significantly changed in magnitude whereas parameter fluctuations appear to follow no distinctive trend. However, these fluctuations were well within the uncertainties associated with the values listed in Table (5.9).

	$\mathbf{F_{N^*}}$	
$N(1440)\frac{1}{2}^+$	-2.595	
$N(1710)\frac{1}{2}^+$	-0.170	
$N(1535)\frac{1}{2}^-$	-0.139	
$N(1650)\frac{1}{2}^-$	-0.040	
	$\mathbf{G^1_{N^*}}$	$\mathbf{G^2_{N^*}}$
$N(1720)\frac{3}{2}^+$	0.026	-0.366
$N(1520)\frac{3}{2}^-$	-1.285	-1.804
$N(1700)\frac{3}{2}^-$	0.590	0.866
$N(1680)\frac{5}{2}^+$	0.032	0.042
$N(1675)\frac{5}{2}^-$	-0.005	0.005
	$\mathbf{G^V_{K^*}}$	$\mathbf{G^T_{K^*}}$
$K^*(892)$	0.617	2.122
$K^1(1270)$	0.389	-2.774
	$\mathbf{g_{pK\Lambda}}$	
	-0.885	
	$\chi^2 = 30.35$	

Table 5.10: s-channel parameters obtained from fit to all data, excluding high energy resonances.

	$\mathbf{F_{\Lambda^*}}$	
$\Lambda(1405)\frac{1}{2}^-$	2.373	
$\Lambda(1670)\frac{1}{2}^-$	−6.328	
	$\mathbf{G^1_{\Lambda^*}}$	$\mathbf{G^2_{\Lambda^*}}$
$\Lambda(1890)\frac{3}{2}^+$	−0.323	−1.948
$\Lambda(1820)\frac{5}{2}^+$	0.013	−0.027
$\Lambda(2110)\frac{5}{2}^+$	−0.013	0.038
$\Lambda(1830)\frac{5}{2}^-$	0.000	−0.002
	$\mathbf{G^1_{\Sigma^*}}$	$\mathbf{G^2_{\Sigma^*}}$
$\Sigma(1385)\frac{3}{2}^+$	−0.033	1.575
$\Sigma(1915)\frac{5}{2}^+$	0.002	−0.001
$\Sigma(1775)\frac{5}{2}^-$	−0.003	0.000

Table 5.11: u-channel parameters obtained from fit to all data, excluding high energy resonances.

Figure (5.22) depicts the total CM energy distribution at three different Θ_{CM}. It is clear from all three energy distributions that the fit does not do well in the 1.9 energy region. In particular, at back angles the fits understimates this region, while it is consistent with the data at all other energy regions. At forward angles, the situation is somewhat different, since it is at energies below 1.9 where the fit understimates the data, while it is overstimated above 1.9 GeV. The starting parameters used for this fit are listed in Tables (5.8) and (5.9). The random behavior of the s-channel parameters in this fit can then be attributed to the abscence of a resonance with mass near the 1.9 GeV energy region. The fitting procedure is trying to compensate the lack of this state, by varying the other parameters in order to obtain a low χ^2_ν, underestimating the structure of the observable in this energy region. An attempt to include polarization data in the fitting procedure described above significantly raised the value of the χ^2_ν. Plots obtained could not be in any way comparable to experimental data. With this is mind, it becomes evident that excluding higher energy resonances in the model lead to fits that are highly inconsistent with experimental data, when energies above 2.0 GeV are incorporated.

The first set of fits incorporated all the s, u, and t-channel resonances introduced in the previous section and the four less well-established resonances earlier in this section. The u-channel resonances eliminated in the last low energy fits, given in Table (5.7), were included in this high energy fit to study their contributions at higher energies as well as

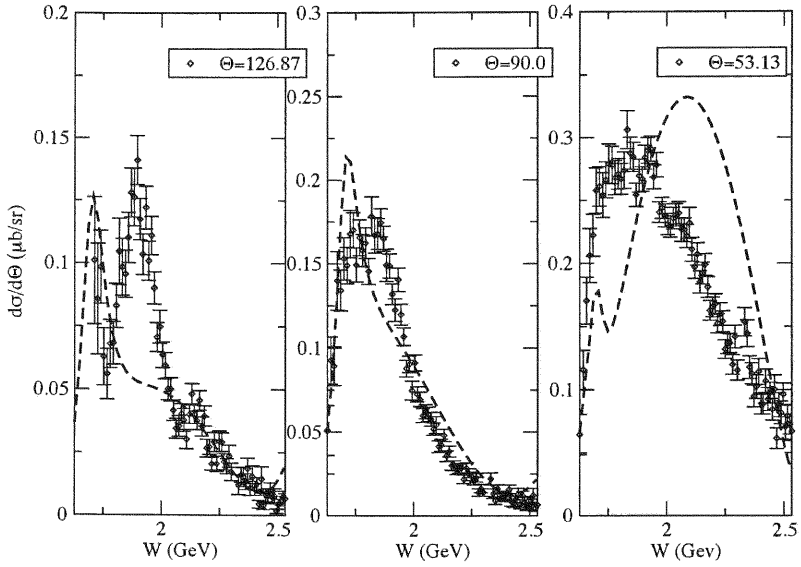

Figure 5.22: Unpolarized differential cross section for the reaction $\gamma + p \rightarrow K^+ + \Lambda$ at three scattering angles, Θ_{CM}. The dashed lines were obtained using the parameters listed in Table (5.10) and (5.11).

the uncertainties associated with them. The parameters associated with s and t channel resonances and their uncertainties are given in Table (5.12). The parameters associated with u-channel resonances are given in Table (5.13), where only negative parity spin $\frac{1}{2}$, positive parity spin $\frac{3}{2}$, and both positive and negative parity spin $\frac{5}{2}$ resonances are shown. The uncertainties associated with the remaining u-channel resonances were in some cases a factor of three larger than the uncertainties associated with the parameters given in Table (5.13).

Comparing the low energy fit parameters given in Table (5.6) with the fit described above clearly reveals how well the s and t-channel parameters are fixed in both fitting procedures. Values for the parameters corresponding to states with total angular momentum $J = \frac{1}{2}$ and the born term remained fairly consistent in both low and high energy fits. Both coupling products increased for the positive parity $J = \frac{3}{2}$ state and decreased for negative parity $J = \frac{3}{2}$ states, with the exception of the $N^*(1520)$ state, which obtained a negative coupling in the high energy fit. Furthermore, the couplings of $J = \frac{5}{2}$ states to the $K\Lambda$ channel are far weaker than those obtained from lower energy fits.

	$\mathbf{F_{N^*}}$		
$N(1440)\frac{1}{2}^+$	-3.317 ± 0.329		
$N(1710)\frac{1}{2}^+$	0.058 ± 0.024		
$N(1535)\frac{1}{2}^-$	0.088 ± 0.091		
$N(1650)\frac{1}{2}^-$	-0.159 ± 0.029		
	$\mathbf{G^1_{N^*}}$	$\mathbf{G^2_{N^*}}$	
$N(1720)\frac{3}{2}^+$	0.180 ± 0.006	0.373 ± 0.015	
$N(1520)\frac{3}{2}^-$	-0.228 ± 0.091	-0.290 ± 0.206	
$N(1700)\frac{3}{2}^-$	-0.039 ± 0.063	-0.218 ± 0.100	
$N(1680)\frac{5}{2}^+$	-0.004 ± 0.002	-0.004 ± 0.001	
$N(1675)\frac{5}{2}^-$	-0.003 ± 0.001	-0.013 ± 0.002	
Higher Energy Resonances			
	$\mathbf{G^1_{N^*}}$	$\mathbf{G^2_{N^*}}$	$\mathbf{\Gamma_{N^*}}$ (MeV)
$N(1900)\frac{3}{2}^+$	-0.013 ± 0.002	0.080 ± 0.008	152.7 ± 8.0
$N(2080)\frac{3}{2}^-$	-0.022 ± 0.021	0.020 ± 0.031	493.5 ± 142.1
$N(2000)\frac{5}{2}^+$	0.000 ± 0.0004	-0.000 ± 0.0003	59.7 ± 14.4
$N(2200)\frac{5}{2}^-$	0.001 ± 0.0001	0.002 ± 0.0004	415.2 ± 51.0
	$\mathbf{G^V_{K^*}}$	$\mathbf{G^T_{K^*}}$	
$K^*(892)$	-1.052 ± 0.233	3.217 ± 0.334	
$K^1(1270)$	-3.947 ± 0.641	5.931 ± 1.805	
	$\mathbf{g_{pK\Lambda}}$		
	-2.458 ± 0.542		
	$\chi^2 = 2.865$		

Table 5.12: Preliminary high energy fit: s and t-channel paramters.

	$\mathbf{F_{\Lambda^*}}$	
$\Lambda(1405)\frac{1}{2}^-$	-4.147 ± 19.84	
$\Lambda(1670)\frac{1}{2}^-$	-2.799 ± 160.030	
	$\mathbf{G^1_{\Lambda^*}}$	$\mathbf{G^2_{\Lambda^*}}$
$\Lambda(1890)\frac{3}{2}^+$	1.638 ± 1.147	0.767 ± 4.926
$\Lambda(1820)\frac{5}{2}^+$	-0.002 ± 0.463	-0.003 ± 1.512
$\Lambda(2110)\frac{5}{2}^+$	0.002 ± 0.377	0.021 ± 1.037
$\Lambda(1830)\frac{5}{2}^-$	0.023 ± 0.084	-0.001 ± 4.926
	$\mathbf{F_{\Sigma^*}}$	
$\Sigma(1750)\frac{1}{2}^-$	9.302 ± 146.444	
	$\mathbf{G^1_{\Sigma^*}}$	$\mathbf{G^2_{\Sigma^*}}$
$\Sigma(1385)\frac{3}{2}^+$	-0.791 ± 0.605	1.571 ± 1.960
$\Sigma(1915)\frac{5}{2}^+$	0.005 ± 0.827	-0.021 ± 2.520
$\Sigma(1775)\frac{5}{2}^-$	-0.019 ± 0.079	0.023 ± 0.305

Table 5.13: Preliminary high energy fit: Selected u-channel parameters

In addition, the t-channel resonance parameters corresponding to the $K^1(1270)$ and $K^*(892)$ states obtained in the high energy fits have values well within the uncertainties associated with the t-channel parameters given in Table (5.6). A remarkable result exhibited in this preliminary fit concerns the behavior of the model at energies beyond 1.9 GeV, which appears to be completely dominated by the positve parity $N^*(1900)$ resonance and the negative parity $N^*(2080)$ state. The two additional spin $\frac{5}{2}$ resonances included in the high energy fit couple weakly to the $K\Lambda$ channel as can be seen by their coupling strengths in Table (5.12). The total decay widths obtained in the fit for the $N^*(1900)$ and $N^*(2080)$ states were $152.7^{\pm 7.95}$ MeV and $493.5^{\pm 142.1}$ MeV respectively. The u-channel parameters in the high energy fit exhibited the same behavior observed in the low energy regime when all u-channel parameters were allowed to vary. The uncertainties associated with these coupling strengths are unacceptably large, which suggests that the many different sets of u-channel parameters would generate fits to the experimental data with similar χ^2_ν values.

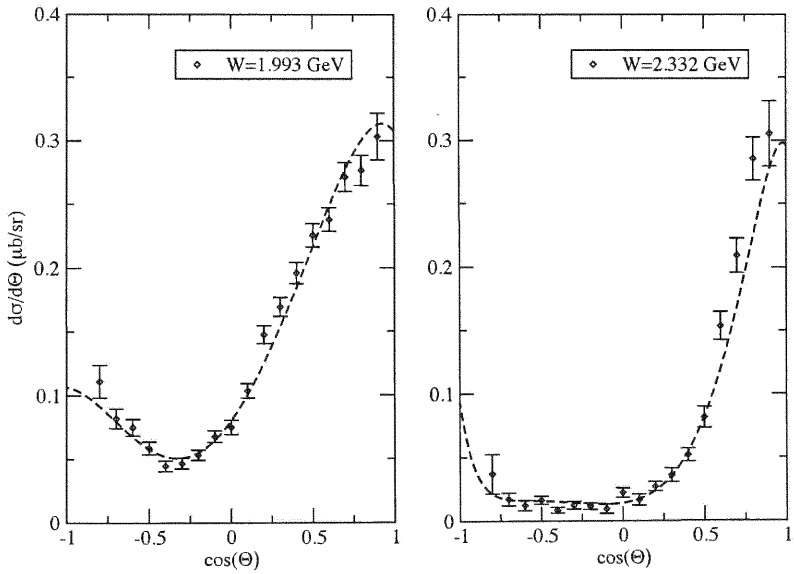

Figure 5.23: Unpolarized differential cross section for the reaction $\gamma + p \rightarrow K^+ + \Lambda$ at two CM energies. The dashed curves were obtained by varying all u-channel resonances and incorporaing four higher energy resonances.

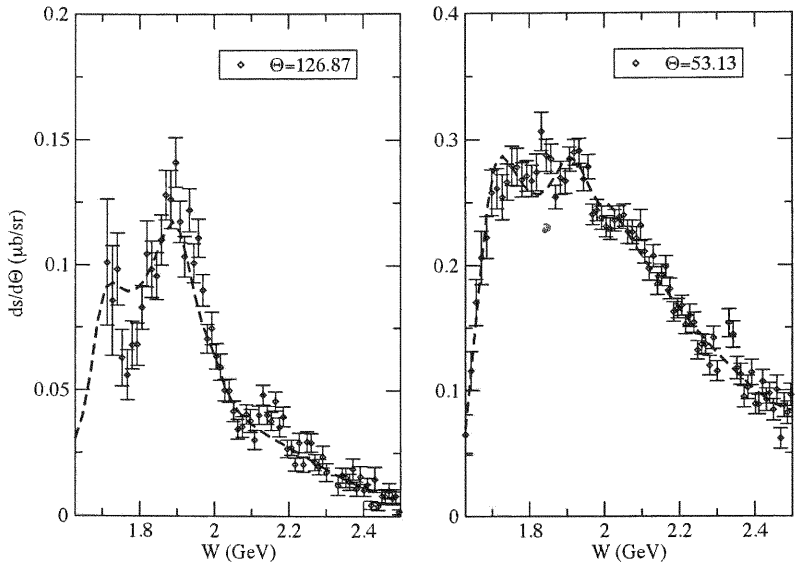

Figure 5.24: Unpolarized differential cross section for the reaction $\gamma + p \rightarrow K^+ + \Lambda$ at two scattering angles Θ_{CM}. The dashed curves were obtained by varying all u-channel resonances parameters, and incorporaing four higher energy resonances.

Figures (5.23) and (5.24) depict the unpolarized differential cross section as as function of the CM scattering angle and the total CM energy, respectively. The uncertainties associated with these fits are not depicted in the figures, since they tend to be very large at back angles, and are essentially zero at forward angles. Furthermore, the uncertainties associated with the energy distribution at $\Theta_{CM} = 53.13°$ are very small at all energies, but are large throughout the whole energy range at $\Theta_{CM} = 126°$. The model seems to describe the data well with a few exceptions. At 2.332 GeV, the fit does fall short of experimental data at angles between zero and 60 degrees, and at 126°, the model overestimates the data between 1.7 and 1.8 GeV. This behavior is also evident in the low energy fits, as seen in Figure (5.6) at 114°. The asymmetry C_z is depicted in Figure (5.25) at $\Theta_{CM} = 100.49°$ and $\Theta_{CM} = 31.79°$. The fit to the energy distribution at $\Theta_{CM} = 31.79°$ does very well for all energies. At $\Theta_{CM} = 110.49°$ the fit fails to properly describe the energy region above 1.9 GeV. The uncertainty band associated with this fit was not included in the figure, mainly because it is so large at energies above 1.9 GeV.

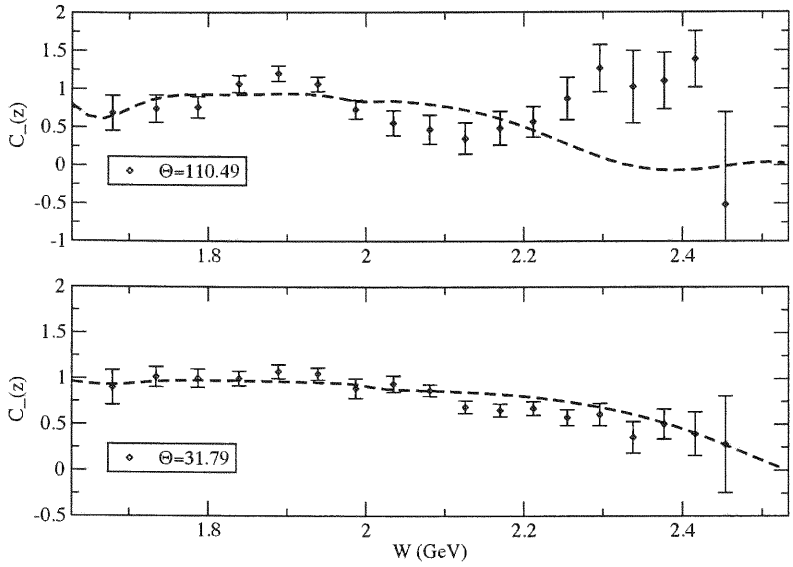

Figure 5.25: Asymmetry C_z as a function of the total CM energy at two CM scattering angles Θ_{CM}. The dashed curves were obtained by varying all u-channel resonance parameters and incorporating four high energy resonances.

The large values and uncertainties associated with certain u-channel parameters motivated a similar fitting procedure to the one performed in the low-energy regime. A series of fits was conducted to effectively eliminate the u-channel parameters with large uncertainties without significantly increasing the χ^2_ν. The lowest χ^2_ν value was obtained by eliminating from the high energy fits the resonances listed in Table (5.14), which unlike Table (5.7), does not include the negative parity $\Sigma^0(1750)$ state. The s and t-channel parameters of the resulting fit, which includes the four less well-established higher energy resonances are given in Table (5.15) together with their uncertainties. The u-channel parameters obtained in this fit are given in Table (5.16). Comparing Tables (5.12) and (5.15) again reveals the stability of the s-channel parameters in fits which exclude the u-channel resonances given in Table (5.14). In fact all parameters for $J = \frac{1}{2}$ resonances showed a slight increase in magnitude and no change in sign. The states with total angular momentum $J = \frac{3}{2}$ slightly decreased in magnitude with the exception of the negative parity $N^*(1700)$ state. Eliminating u-channel parameters from the fit did not affect the magnitudes of the s-channel $J = \frac{5}{2}$ states, which seem to always couple weakly to the $K\Lambda$ channel at these energies. The u-channel parameters included in this fit had uncertainties significantly smaller than those

u-channel		
Mass (MeV)	Isospin I	J^p
$\Lambda^*(1600)$	0	$\frac{1}{2}^+$
$\Lambda^*(1810)$	0	$\frac{1}{2}^+$
$\Lambda^*(1520)$	0	$\frac{3}{2}^-$
$\Lambda^*(1690)$	0	$\frac{5}{2}^-$
$\Sigma^*(1660)$	1	$\frac{1}{2}^+$
$\Sigma^*(1670)$	1	$\frac{3}{2}^-$
$\Sigma^*(1940)$	1	$\frac{3}{2}^-$

Table 5.14: u-channel resonances eliminated in the new high energy fit

	$\mathbf{F_{N^*}}$		
$N(1440)\frac{1}{2}^+$	-2.805 ± 0.333		
$N(1710)\frac{1}{2}^+$	0.126 ± 0.022		
$N(1535)\frac{1}{2}^-$	0.304 ± 0.037		
$N(1650)\frac{1}{2}^-$	-0.254 ± 0.011		
	$\mathbf{G^1_{N^*}}$	$\mathbf{G^2_{N^*}}$	
$N(1720)\frac{3}{2}^+$	0.147 ± 0.005	0.316 ± 0.014	
$N(1520)\frac{3}{2}^-$	-0.257 ± 0.087	0.063 ± 0.133	
$N(1700)\frac{3}{2}^-$	0.120 ± 0.066	-0.028 ± 0.073	
$N(1680)\frac{5}{2}^+$	0.000 ± 0.002	-0.017 ± 0.002	
$N(1675)\frac{5}{2}^-$	-0.003 ± 0.0003	-0.014 ± 0.001	
Higher Energy Resonances			
	$\mathbf{G^1_{N^*}}$	$\mathbf{G^2_{N^*}}$	$\mathbf{\Gamma_{N^*}}$ (MeV)
$N(1900)\frac{3}{2}^+$	0.024 ± 0.002	-0.035 ± 0.005	191.7 ± 8.8
$N(2080)\frac{3}{2}^-$	0.011 ± 0.003	0.001 ± 0.003	94.4 ± 44.6
$N(2000)\frac{5}{2}^+$	0.003 ± 0.0005	0.001 ± 0.0004	105.6 ± 13.2
$N(2200)\frac{5}{2}^-$	0.0001 ± 0.00003	0.001 ± 0.0001	184.0 ± 33.9
	$\mathbf{G^V_{K^*}}$	$\mathbf{G^T_{K^*}}$	
$K^*(892)$	-1.934 ± 0.065	0.963 ± 0.087	
$K^1(1270)$	0.639 ± 0.230	4.059 ± 0.843	
	$\mathbf{g_{pK\Lambda}}$		
	-0.245 ± 0.338		
	$\chi^2 = 2.907$		

Table 5.15: s and t-channel high energy fit parameters.

	F_{Λ^*}	
$\Lambda(1405)\frac{1}{2}^-$	-4.359 ± 7.431	
$\Lambda(1670)\frac{1}{2}^-$	-0.939 ± 46.778	
	$G^1_{\Lambda^*}$	$G^2_{\Lambda^*}$
$\Lambda(1890)\frac{3}{2}^+$	1.771 ± 0.264	2.299 ± 1.951
$\Lambda(1820)\frac{5}{2}^+$	0.010 ± 0.045	0.014 ± 0.400
$\Lambda(2110)\frac{5}{2}^+$	0.031 ± 0.034	0.012 ± 0.282
$\Lambda(1830)\frac{5}{2}^-$	0.040 ± 0.023	0.151 ± 0.165
	F_{Σ^*}	
$\Sigma(1750)\frac{1}{2}^-$	9.21 ± 40.419	
	$G^1_{\Sigma^*}$	$G^2_{\Sigma^*}$
$\Sigma(1385)\frac{3}{2}^+$	-0.675 ± 0.164	-2.471 ± 1.213
$\Sigma(1915)\frac{5}{2}^+$	-0.036 ± 0.077	-0.021 ± 0.674
$\Sigma(1775)\frac{5}{2}^-$	-0.031 ± 0.022	-0.154 ± 0.158

Table 5.16: u-channel high energy fit parameters.

given in Table (5.13). Two resonances in the u-channel continue to exhibit large uncertainties, the $\Lambda^*(1670)$ and the $\Sigma^*(1750)$. The latter state, unlike in lower energy fits, led to high values of χ^2_ν if excluded from the fit. In addition, the born coupling was significantly smaller, but this behavior was also present in the low energy analysis, where a smaller born coupling parameter was obtained after fitting the data without the resonances listed in Table (5.7). Removing u-channel resonances from the fit did not greatly affect the magnitudes of the parameters associated with the two spin $\frac{3}{2}$ high energy resonances, but in most cases inverts the signs of the coupling products. The decay width of the $N^*(1900)$ slightly increases to $191.7^{\pm 8.8}$ MeV and that for the $N^*(2080)$ decreases to $94.4^{\pm 44.6}$ MeV when compared to the previous high energy fit. Judging from the uncertainties in both the coupling products and total decay widths, the model appears to be more sensitive to the positive parity $N^*(1900)$ state. As with the other spin $\frac{5}{2}$ s-channel states, the newly incorporated $N^*(2000)$ and $N^*(2200)$ have negligible couplings to the reaction's final states at these energies. As in the low energy fits, eliminating the u-channel resonances in Table (5.12) does not affect the quality of the fits. This fitting procedure did lead to a decrease in the fit uncertainties at back angles and yielded uncertainty bands almost completaly symmetric about the fit's curve. Eliminating the resonances in Table (5.12) does not significantly affect the fit to the angular distribution at $W = 2.332$ GeV as seen in fig. (5.26). As in Fig. (5.23), for which all resonances are incorporated in the fit, the cross section is underestimated at forward

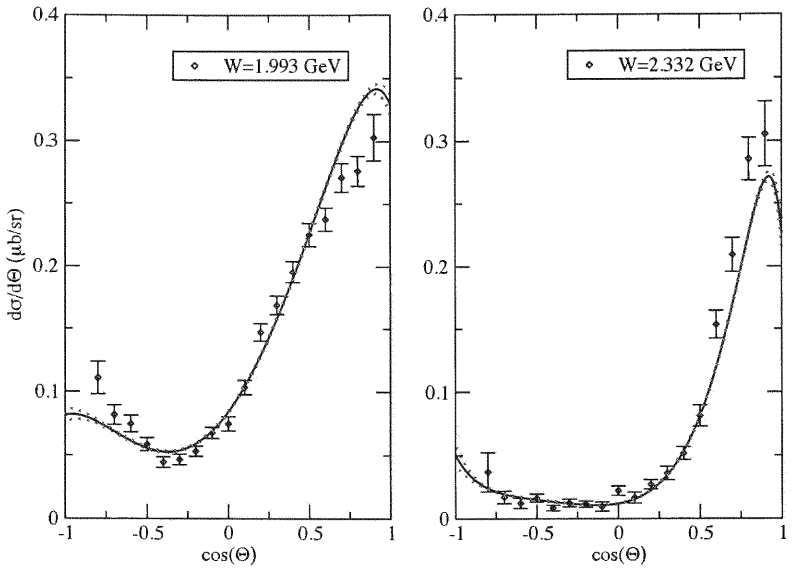

Figure 5.26: Unpolarized differential cross section for the reaction $\gamma + p \rightarrow K^+ + \Lambda$ at two CM energies. The dashed curves were obtained using the parameters listed in Table (5.15) and (5.16). The dotted curves represent the uncertainty in the fit.

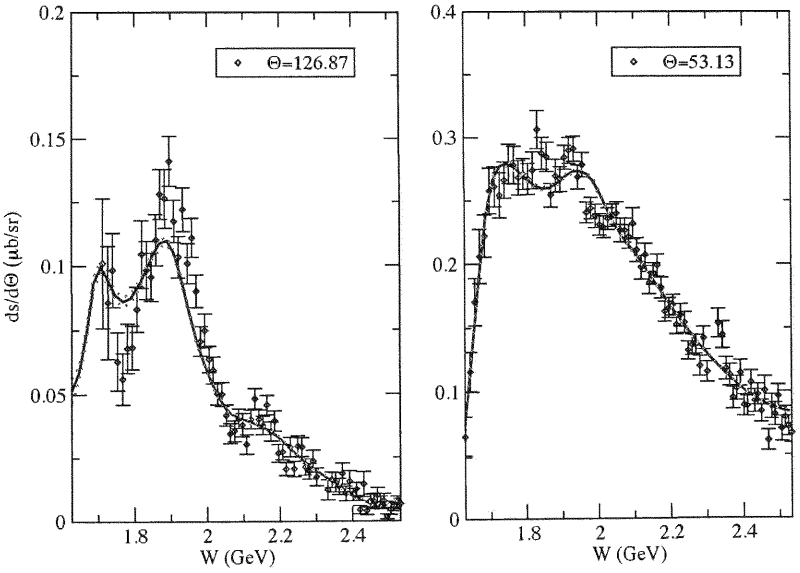

Figure 5.27: Unpolarized differential cross section for the reaction $\gamma + p \rightarrow K^+ + \Lambda$ at two scattering angles, Θ_{CM}. The dashed curves using the parameters listed in Tables (5.15) and (5.16). The dotted curves represent the uncertainty in the fit.

angles. In both Figs. (5.26) and (5.27) it can be seen that the fits do not describe the data very well at low energies for CM angles greater than 120°. This is also evident in the low energy fits described in the previous section.

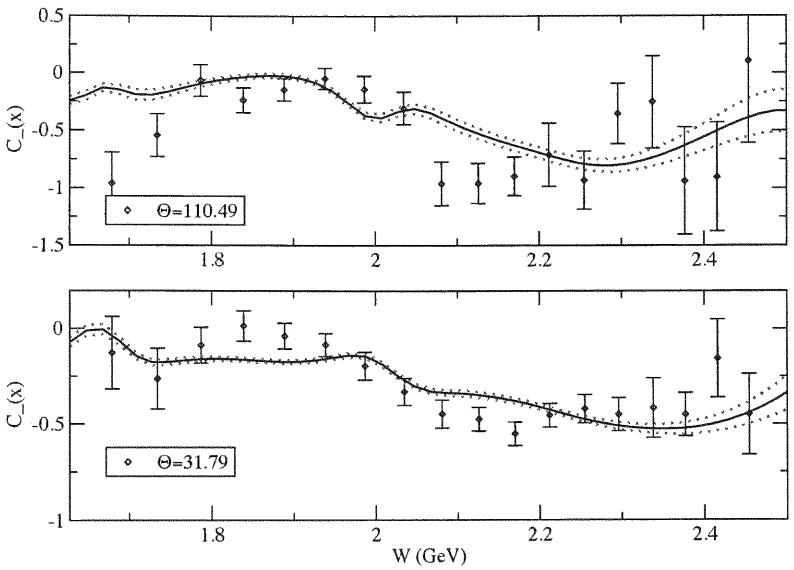

Figure 5.28: Asymmetry C_x as a function of the total CM energy at two scattering angles, Θ_{CM}. The solid curves were obtained using the parameters listed in Tables (5.15) and (5.16). The dotted curves represent the uncertainty in the fit.

The asymmetries C_x and C_z are depicted in Figs. (5.28) and (5.29) as functions of the total CM energy. For C_x and C_z the model describes the data well for all CM energies at forward angles, but fails to do so at angles greater than 90°. In the low energy region, the fit to C_z does well near threshold, unlike C_x for which the model overestimates the data. Figures (5.30) and (5.31) depict the angular distribution of C_x and C_z respectively. The model yields better results for C_x. The data suggests that for most energies and angles that the polarization transfer has no preferred direction. The results are quiet different for C_z, for which the data suggests that that transfer of polarization has a preferred direction. The fit is poorest at high energies, since it is here that the data not lying around 90° suggest values for C_z which are greater than one. Discrepancies with the data are thus unavoidable

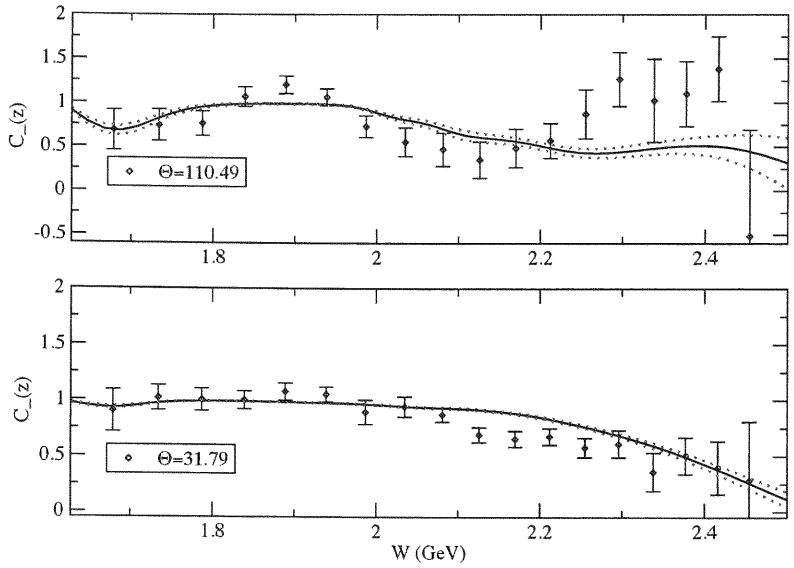

Figure 5.29: Asymmetry C_z as a function of the total CM energy at two scattering angles, Θ_{CM}. The solid curves were obtained using the parameters listed in Tables (5.15) and (5.16). The dotted curves represent the uncertainty in the fit.

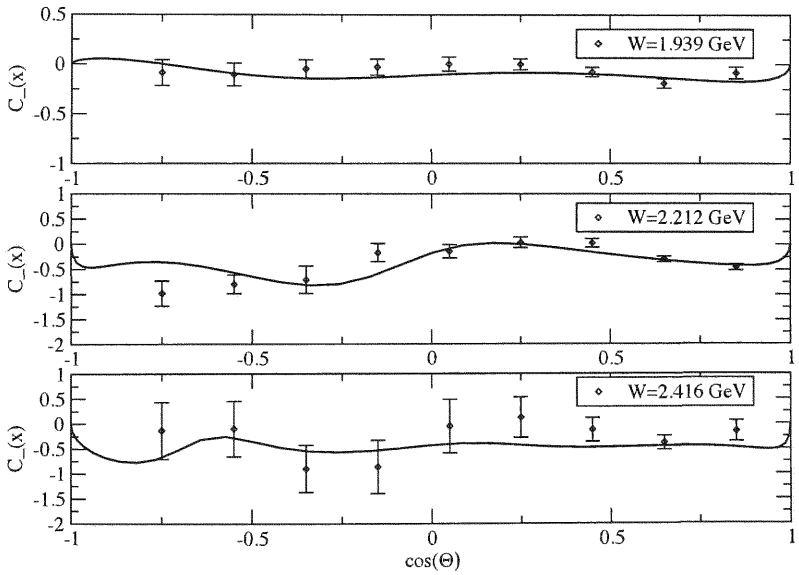

Figure 5.30: Asymmetry C_x as a function of Θ_{CM}. The solid curves were obtained using the parameters listed in Tables (5.15) and (5.16).

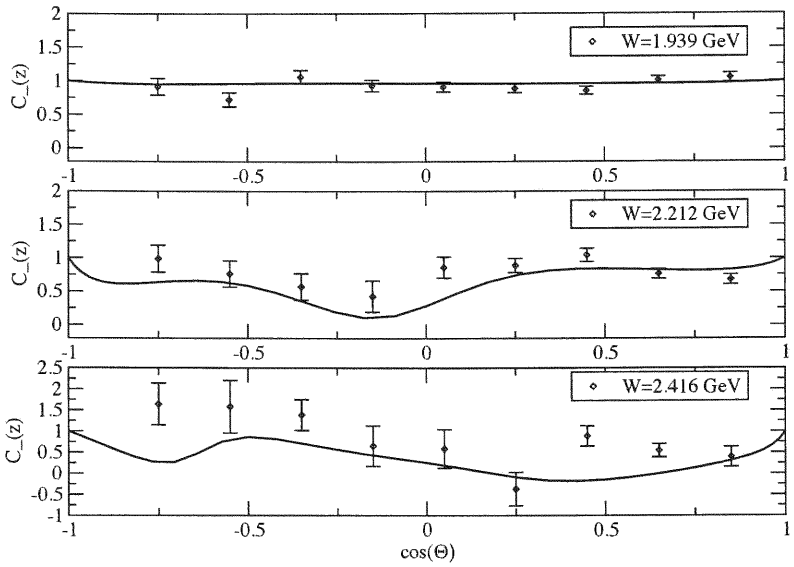

Figure 5.31: Asymmetry C_z as a function of Θ_{CM}. The solid curves were obtained using the parameters listed in Tables (5.15) and (5.16).

in this region since the polarization transfer observables are defined to lie in the range $-1 \leq C_z \leq 1$.

Using the parameters listed in Tables (5.15) and (5.16) as starting parameters, we studied the behavior of the fits when each of the four less well-established spin $\frac{3}{2}$ and $\frac{5}{2}$ resonances was removed. A fit was conducted for each individual resonance eliminated to study the behavior of the χ^2_ν. We made use of the parameter:

$$f_{N^*} = \frac{\chi^2_{All} - \chi^2_{All-N^*}}{\chi^2_{All}} \cdot 100, \tag{5.2}$$

introduced in the multipole analysis of the CLAS data in [45], which measures the relative change in the χ^2_ν when a N^* resonance is removed from the fitting procedure. The resulting f_{N^*} obtained from the fits are listed in Table (5.17). Judging from Table (5.17) we can conclude that the fit is thus more sensitive to the positive parity spin $\frac{3}{2}$ $N^*(1900)$ state and the positive parity spin $\frac{5}{2}$ $N^*(2000)$ state. In particular, including just these two states in the fits yields values for the Born coupling $g_{pK\Lambda}$ in close agreement to the value obtained in the high energy fit, Table (5.15). Figure (5.32) depicts the total CM energy distribution

J^P	Mass (MeV)	$\chi^2_{N^*}$	χ^2_{All}	f_{N^*}	$g_{pK\Lambda}$
$\frac{3}{2}^+$	1900	5.372	2.907	85%	−0.403
$\frac{3}{2}^-$	2080	2.965	2.907	2%	−0.250
$\frac{5}{2}^+$	2000	4.564	2.907	57%	−0.068
$\frac{5}{2}^-$	2200	3.018	2.907	4%	−0.237

Table 5.17: Relative χ^2_ν differences from fits excluding individual resonances.

at both backward and forward angles. The solid black curves were obtained by fitting the observables without the $N^*(2080)$ and $N^*(2200)$ states. This fit has comparable quality to that of the high energy fit depicted in Fig. (5.27). This result is consistent with Table (5.17), since eliminating either resonance from the fitting procedure led to a relative χ^2_ν deviation below five percent. The dashed curves were obtained by fitting the observables without parameters associated with the spin $\frac{3}{2}$ positive parity $N^*(1900)$ state. The fit is clearly shifted to the left, and fails to describe the data well at around 1.9 GeV. The fitting procedure attempted to compensate for the absence of this state by overestimating the cross section at lower energies. Beyond 2 GeV, excluding the $N^*(1900)$ does not affect the quality of the fit. The dotted dashed curves were obtained by fitting without the positive parity spin $\frac{5}{2}$ state. The absence of this resonance in the fit only affected the quality of the fit at back angles well beyond 2.4 GeV. It is clear from all the fits that there seems to be a structure around 2.3 Gev which was not accounted for in this study.

We also studied the sensitivity of the model to the absence of each of the kaon resonances. The solid curves in Fig. (5.33) depict the cross section as a function of Θ_{CM} using the parameters in Tables (5.15) and (5.16), setting the coupling products for the $K^*(892)$ resonance to zero. The dashed curves depict the cross section, when the remaining parameters are refit without the $K^*(892)$ resonance. The χ^2_ν obtained from this fit is extremely high, but more interesting, yields a Born coupling very close to zero, $g_{pK\Lambda} = 0.0004$. Clearly, the absence of the $K^*(892)$ state forces the Born coupling to decrease in magnitude, overestimating the cross section at both backward and forward angles. It appears that the inclusion of kaon excited states is important in the model if one wants to reproduce the Born coupling in closer agreement with previous theoretical studies, such as those mentioned in Section (4.4).

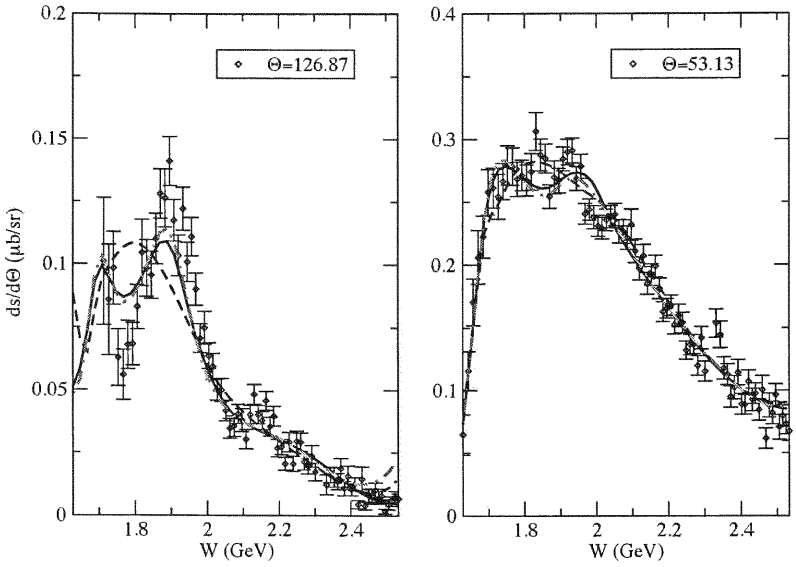

Figure 5.32: Unpolarized differential cross section for the reaction $\gamma + p \rightarrow K^+ + \Lambda$ at two scattering angles, Θ_{CM}. The solid black represent a fit without the $N^*(2080)$ and $N^*(2200)$ states, the dashed curves represent a fit without the $N^*(1900)$ state, and the dotted dashed curves represent a fit without the $N^*(2000)$ state.

Looking at the solid curves, one can conclude that the $K^*(892)$ has a stronger contribution at forward angles, which appears more relevant at energies above 2.0 GeV. The solid curves in Fig. (5.34) depict the cross section as a function of Θ_{CM} using again the parameters in Tables (5.15) and (5.16), setting the coupling products for the $K1(1270)$ resonance to zero. This curve clearly shows that the resonance does not impose a prefered angular dependence on the distribution. In fact, the shift appears uniform throughout the angular range. The dashed curves shows a fit to the cross section which does not include the $K1(1270)$ state. Eliminating this state from the fitting procedure yielded a $\chi^2 = 100.3$, an order of magnitude smaller than that obtained by eliminating the $K^*(892)$ state. The smaller value of the χ^2_ν is a result of the apparent angle independence of this resonance. Eliminating this resonance from the fitting procedure yielded also a smaller value for the Born coupling $g_{pK\Lambda} = -0.0002$, as well as a smaller coupling for the $N^*(1440)$ state, $F_{N^*} = -1.509$, when compared to those listed in Table (5.15). Clearly, these two are the dominant background contributions, and thus, their contributions are significantly affected after excluding the $K1(1270)$.

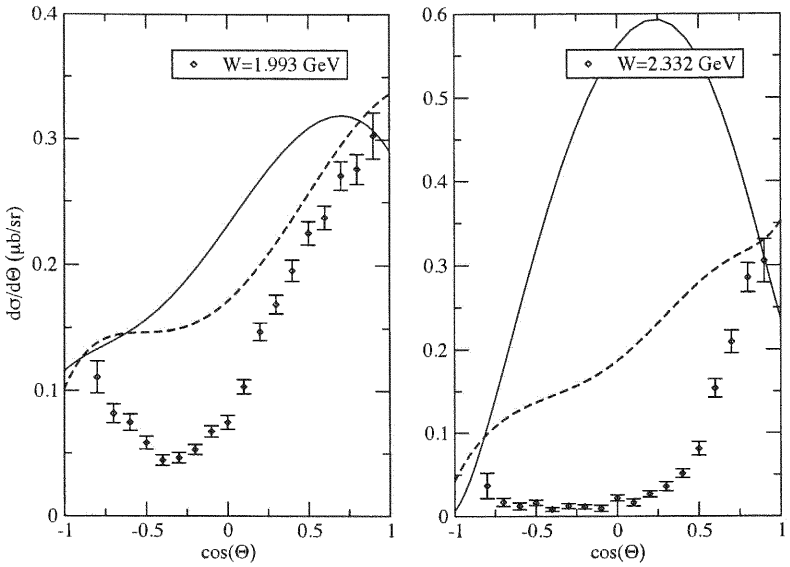

Figure 5.33: Unpolarized differential cross section angular distribution. The solid curves were obtained using the parameters in Tabless (5.15) and (5.16) with zero couplings for the $K^*(892)$ state. The dashed curves represent a fit to the cross section without a $K^*(892)$ contribution.

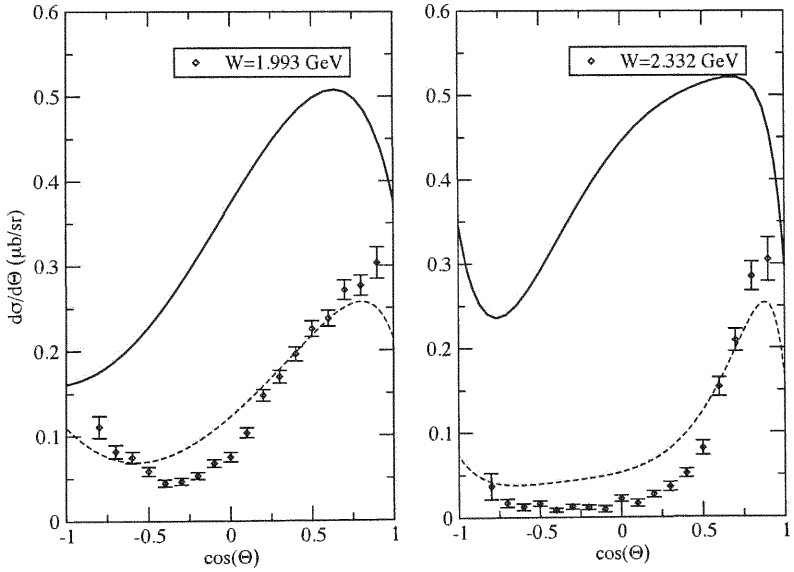

Figure 5.34: Unpolarized differential cross section angular distribution. The solid curves were obtained using the parameters in Tabels (5.15) and (5.16) with zero couplings for the $K^*(1270)$ state. The dashed curves represent a fit to the cross section without a $K^*(1270)$ contribution.

Eliminating kaon resonances form the isobar model discussed in this study has a direct effect on both the Born coupling and the Roper resonance $N^*(1440)$. Including them in the model significantly affects the background contributions to the observables and becomes highly important if the model is to predict a value for the Born coupling that is in closer agreement with the theoretical works discussed in Section (4.4). Unlike the $K1(1270)$ resonance, the $K^*(892)$ appears to have a strong angular dependence, where most of its background contribution lies in the forward angular region.

5.3 Conclusions

Using the isobar model developed here, we studied the reaction $\gamma + p \rightarrow K^+ + \Lambda$ using experimental data for the unpolarized differential cross section and two double polarization observables, C_x and C_z. The study was conducted by performing a fit to the experimental data at both low and high energies. The parameters used in the model were the coupling products between the electromagnetic and strong vertices for nucleon, hyperon and kaon resonances with masses below 2.2 Gev, and the total decay widths for resonances that have not been well established experimentally but have been predicted by various theoretical models.

Within the low energy fitting procedure, we were able to determine that for an accurate description of the experimental data, both cross section and polarization observables had to be fit simultaneously. Furthermore, incorporating polarization data in the fits was useful in discriminating between different sets of starting parameters that resulted in similar χ^2_ν values when only the cross sections were fit. In addition, fits to the low energy region led to the conclusion that the incorporation of a wide spectrum of hyperon resonances with angular momentum $J \leq \frac{5}{2}$ leads to undesirable uncertainties in the u-channel parameters. Large uncertainties indicate a lack of sensitivity of the model to these parameters, and thus, the model cannot be used to determine with certainty the values for the u-channel coupling products. Furthermore, incorporating a wide spectrum of u-channel resonances led to undesirable uncertainties in the fits to the obesrvables, in particular, where the uncertainty bars

associated with the experimental data are large. This behavior associated with u-channel resonances can be traced back to their respective propagators. The u-channel variable in the hyperon's propagator is often negative and far off the mass-shell. In particular, hyperons with the same quantum numbers becomes indistiguishable, and thus a large number of different parameter combinations becomes available, which lead to comparable fits. Within the low energy regime, we were able to systematically remove u-channel resonances from the fit without significantly affecting the value of the χ^2_ν. We observed a significant decrease in both the coupling products and uncertainties associated with resonances in the u-channel. Furthermore, it was noted that removing u-channel parameters from the fitting procedure did not significantly affect the values of the parameters associated with the s and t-channel resonances, but resulted in slight increases in the parameter uncertainties. It was also noted that systematically removing u-channel resonances from the fitting procedure led to very small uncertainties in the fitted observables. This was evidence that the remaining parameters in the model were better constained within the low energy region.

Attempts to use the parameters obtained in the low energy fits for energies above 2 Gev, without refitting revealed that employing parameters obtained from lower energy fits do not describe the photoproduction reaction very well at higher energies. Furthemore, carrying out fits with just the low energy resonances introduced in Section (5.1) led to large values of the χ^2_ν, indicating a poor description of the experimental data in the 1.9 GeV region, as well as above 2.4 GeV. This result was helpful in determining that s-channel resonances with masses greater than 1.9 GeV are needed for an accurate description of the data. The behavior of the u-channel parameters seen in the low energy fits was also evident when attempting to incorporate all u-channel resonances into fits to higher energy. In particular, minimizing both the uncertainties in the u-channel parameters as well as the uncertainties in the fits to the observbles while keeping a desirable value for the χ^2_ν was only made possible by excluding the same set of resonances eliminated from the low energy fit, with the exception of the $\Sigma^*(1750)$ state. Furthermore, eliminating this set of resonances from the fitting procedure led to smaller uncertainties of the parameters associated with

the remaining u-channel resonances, as well as parameters associated with s and t-channel states, as can be seen by comparing Tables (5.8) and (5.9) with Tables (5.15) and (5.16). A larger range of energies available for fits to experimental data better constrained the parameters used in the isobar model.

We arrived at the following observations after comparing the parameters obtained from the low energy fit to those obtained in the high energy fit. It was noted that the parameters associated with positive parity spin $\frac{1}{2}$ s-channel states increased in magnitude, while the parameters associated with negative parity spin $\frac{1}{2}$ states decreased. Furthermore, with the exception of the $N^*(1535)$, all s-channel spin $\frac{1}{2}$ parameters had the same signs after extending the fits to higher energies. A rather different result was observed for states with total angular momentum $J = \frac{3}{2}$ and $\frac{5}{2}$. With the exception of the $N^*(1520)$ state, which attained a higher coupling of the same sign between the fits, there was no clear trend in the parameters associated with resonances carrying the same quantum numbers. The lack of consistency between fits could be attributed to the fact that most of the higher angular momentum states, $J \geq \frac{3}{2}$, have masses very close to 1700 MeV and thus their contributions tend to become indistinguishable. In the isobar model employed, states with the same angular momentum and opposite parities differ only by a negative sign and thus can be easily mixed to produce a lower χ^2_ν, especially if their coupling products are close to zero. In addition, in both low and high energy fits, it was observed that states with total angular momentum $J = \frac{5}{2}$ couple weakly to the $K\Lambda$ channel for the energies considered in this study.

The leading coupling constant, $g_{pK\Lambda}$, was also affected by incorporating higher energies into the fits. The value for $g_{pK\Lambda}$ decreased in magnitude from -0.667 in the low energy fit to -0.245 in the high energy fit. Both fits agree on the sign of $g_{pK\Lambda}$, but the magnitudes obtained are far less than the values obtained from other fits to photoproduction data as well as from QCD inspired models, discussed in Section (4.4). This disagreement can be attributed to the fact that some ingredients are still missing from this model. In particular,

a complete description of the photoproduction mechanism may be sought by incorporating hadronic form factors that take into account the structure of the hadrons. In addition, incorporating off-shell parameters into the intermediate particle propagators may significantly affect the contributions to the amplitudes, given that they take into account the lower spin components of interacting particles with total angular momentum $J \geq \frac{3}{2}$.

Through a systematic analysis of the four less-well established resonances incorporated in the high energy fit, we were able to determine those for which the photoproduction reaction is more sensitive. It was concluded that the photoproduction reaction is mostly sensitive to both the positive parity spin $\frac{3}{2}$ $N^*(1900)$ state as well as the positive parity spin $\frac{5}{2}$ $N^*(2000)$ state. Eliminating both the $N^*(2080)$ and $N^*(2200)$ did not significantly affect the quality of the fits, and thus they are not relevant in the description of the experimental data within the model employed in this study. Furthemore, the total decay widths Γ_R associated with the $N^*(1900)$ and $N^*(2000)$ states are significantly smaller than those listed in the Particle Data Tables [18].

A detailed study of resonaces in the t-channel was also conducted. The study revealed that both the $K^*(892)$ state, and the $K1(1270)$ significantly affect the background contributions to the photoproduction reaction. In particular, it was observed that excluding either resonance from the fitting procedure led to a value for the leading coupling constant, $g_{pK\Lambda}$, very close to zero. It was also noted that unlike the $K1(1270)$ state, the $K^*(892)$ has a strong angular dependence, especially at forward angles. The parameters associated with the t-channel resonances obtained in the low energy fit differed from those obtained in the high energy fit. In particular, no unambiguous values could be determined for either the vector and tensor couplings associated with these resonances, only that they are highly correlated to the leading coupling constant.

The physical observables included in this study have been well reproduced within the effective lagrangian model studied here. Furthermore, we were able to extend the fit by incorporating two resonances, whose existence is not yet well determined. In addition, it was

determined that an accurate description of u-channel resonances is not available through this phenomenological approach, but a limited number of u-channel parameters is indeed needed to reproduce the physical observables considered here. The results shown in this study can serve as a foundation to study other photoproduction and electroproduction reactions. In particular, parameters obtained throughout these fits can be used as starting points in models which are used to obtain other parameters such as hadronic and electromagnetic form factors.

[1] J.R. Christman. $SU(3)$ and the quark model. *Project Physnet*, pages 1–18, 2001.

[2] H. Thom. *Physical Review*, 151:1322, 1966.

[3] F.M. Renard and Y. Renard. Photoproduction of $K^+\Lambda$ and $K^+\Sigma^o$ and $g_{\Lambda KN}$ and $g_{\Sigma KN}$ coupling constants. *Nuclear Physics*, **B25**:490–498, 1971.

[4] J.J. De Swart. The octet model and its clebsch-gordan coefficients. *Reviews of Modern Physics*, **34**:916–932, 1963.

[5] D. Faiman and A.W. Hendry. Harmonic-oscillator model for baryons. *Physical Review*, **173**:1720–1730, 1968.

[6] D. Faiman. Harmonic oscillator analysis of the hyperon spectrum. *Nuclear Physics*, **B32**:573–608, 1971.

[7] D. Faiman and D.E Plane. An $SU(6)_W$ fit to the negative parity baryon decays rates. *Nuclear Physics*, **B50**:379–406, 1972.

[8] D. Faiman. Roper. *Nuclear Physics*, **B115**:478–504, 1976.

[9] A.J.G. Hey, P.J. Litchfield and R.J. Cashmore. $SU(6)_W$ and decays of baryon resonances. *Nuclear Physics*, **B95**:516–546, 1975.

[10] R. Bradford, R.A. Shumacher, J.W.C. McNabb, L. Todor et al.,. Differential cross sections for $\gamma + p \rightarrow K^+ + Y$ for Λ and Σ^0 hyperons. *Physical Review*, **C73**:035202–1, 2006.

[11] R. Bradford, R.A. Shumacher, G. Adams et al.,. First measurement of beam-recoil observables C_x and C_z in hyperon photoproduction. *Physical Review*, **C75**:035205–1, 2007.

[12] J.W.C McNabb, R.A. Shumacher, L. Todor et al.,. Hyperon photoproduction in the nucleon resonance region. *Physical Review*, **C69**:042201–1, 2004.

[13] L.J. Reinders, H. Rubinstein and S. Yazaki. Hadron couplings to goldstone bosons in QCD. *Nuclear Physics*, **B213**:109, 1983.

[14] S. Choe, M.K. Cheoun and S.H. Lee. $g_{KN\Lambda}$ and $g_{KN\Sigma}$ from QCD sum rules. *Physical Review*, **C53**:1362, 1996.

[15] R.A. Adelseck, C. Benhold and L.E. Wright. Kaon photoproduction operator for use in nuclear physics. *Physical Review*, **C32**:1681–1692, 1985.

[16] Oren V. Maxwell. Model dependence in the photoproduction of kaons from protons and deuterons. *Physical Review*, **C70**, 2004.

[17] J.C. David, C. Fayard, G.H. Lamot and B. Saghai. Electromagnetic production of associated strangeness. *Physical Review*, **C53**:2613–2637, 1996.

[18] T. Mizutani, C. Fayard, G.H. Lamot and B. Saghai. Off-shell effects in the electromagnetic production of strangeness. *Physical Review*, **C58**:75–90, 1998.

[19] W-M Yao. Nuclear and particle physics. *Journal of Physics*, **G33**:1–, 2006.

[20] A.V Sarantev, V.A. Nikonov, A.V. Anisovich E,. Klempt and U. Thoma. Decays of baryon resonances into Λ K^+ Σ^0 K^+ and $\Sigma^+ K^0$. *Eur. Phys. J.*, **A25**:441–453, 2005.

[21] T. Mart, A. Sulaksono and C. Bennhold. Missing resonances in kaon photoproduction on the nucleon. *Physical Review*, **C61**:108, 2000.

[22] T. Mart and C. Benhold. Evidence for a missing nucleon resonance in kaon photoproduction. *Physical Review*, **C61**:012201–1, 1999.

[23] S. Capstick and W. Roberts. Strange decay of nonstrange baryons. *Physical Review*, **D58**:074011–1, 1998.

[24] M. Gell-Mann. A schematic model of baryons and mesons. *Physics Letters*, **8**:214–, 1964.

[25] G. Zweig. An $SU(3)$ model for strong interaction symmetry and its breaking. *CERN Reports*, **8182**:TH401, 1964.

[26] Nathan W. Dean. *Introduction to the strong interactions.* Gordon and Breach Science Publishers, 1976.

[27] D. Gross and F. Wilczeck. Asymptotically free gauge theories. *Physical Review*, **D8**:3633, 1973.

[28] Ta-Pei Cheng and Ling-Fong Li. *Gauge Theory of Elementary Particle Physics.* Clarendon Press, 1984.

[29] R.H. Dalitz. *Les Houches Lectures.* Gordon and Breach Science Publishers, Inc., 1965.

[30] Michael E. Peskin and Daniel V. Schroeder. *An Introduction to Quantum Field Theory.* Westview Press, 1995.

[31] Bong Soo Han et al. An isobaric model for kaon photoproduction. *Nuclear Physics*, **A691**:713–749, 2001.

[32] C. Fernandez-Ramirez, E. Moya de Guerra and J.M. Udias. Effective lagrangian approach to pion photoproduction from the nucleon. *Annals of Physics*, **321**:1408–1456, 2006.

[33] M. Napsuciale, M. Kirchbach and S. Rodriguez. Spin $\frac{3}{2}$ beyond the rarita-schwinger framework. *Eur. Phys. J.*, **A29**:289–306, 2006.

[34] Huang Shi-Zhong, Zhang Peng-Fei, Ruan Tu-Nan, Zhu Yu-Can and Zheng Zhi-Peng. Feynman propagator for a particle with arbitrary spin. *Eur. Phys. J.*, **C42**:375–389, 2005.

[35] C. Bennhold and L.E. Wright. Pseudovector versus pseudoscalar theory in kaon photoproduction from nucleons and nuclei. *Physical Review*, **C36**:438–440, 1986.

[36] S. S. Hsiao, D. H. Lu and Shin Nan Yang. Pseudovector versus pseudoscalr coupling in kaon photoproduction reexamined. *Physical Review*, **C61**:1–4, 2000.

[37] M. Fierz and W. Pauli. Need title here. *Proc. R. Soc. London*, **A173**:211, 1939.

[38] W. Rarita and J. Schwinger. On the theory of particles with half integral spin. *Physical Review*, **60**:61, 1941.

[39] L.M. Nath, B. Etemadi and J.D. Kimel. Uniqueness of the interaction involving spin $\frac{3}{2}$ particles. *Physical Review*, **D3**:2153–2161, 1971.

[40] M. Benmerrouche, R.M. Davidson and N.C. Mukhopadhyay. Problems of describing spin $\frac{3}{2}$ baryon resonances in the effective lagrangian theory. *Physical Review*, **C39**:2339–2348, 1989.

[41] J. Niederle and A.G Nikitin. Relativistic wave equations of interacting, massive particles with arbitray half integer spins. *Physical Review*, **D64**:125013–1, 2001.

[42] Oren V. Maxwell. Rescattering contributions to the photoproduction of kaons from the deuteron. *Physical Review*, **C69**:034605, 2004.

[43] R.A. Adelseck and B. Saghai. Kaon photoproduction: Data consistency, coupling constants, and polarization observables. *Physical Review*, **C42**:108–42, 1992.

[44] R.A. Adelseck and L.E. Wright. Electromagnetic production of kaons. *Physical Review*, **C38**:1965–1967, 1988.

[45] T. Mart and A. Sulaksono. Kaon photoproduction in a multipole approach. *Physical Review*, **C74**:055203–1, 2006.

Appendices

Appendix A

The lorentz four-vectors I^μ,J^μ, K^μ, and N^μ appearing in Eqs. (4.73) and (4.74) are linear combinations of the photon and intermediate state four momentum, labeled p^μ and p_γ^μ respectively; as well as the photon polarization four-vector ϵ^μ. In the s-channel the vector I^μ can be obtainded by first defining the following terms:

$$\begin{aligned} I_1 &= -\{p_K \cdot p_\gamma - \frac{1}{M_R^2}(p_K \cdot p)(p_\gamma \cdot p)\} \\ I_2 &= -\{\epsilon \cdot p_K - \frac{1}{M_R^2}(p_K \cdot p)(\epsilon \cdot p)\} \\ I_3 &= \frac{1}{M_R^2}\{(p_K \cdot p_\gamma)(\epsilon \cdot p) - \frac{1}{M_R^2}(p_K \cdot p)(p_\gamma \cdot p)(\epsilon \cdot p)\} \\ &+ \frac{1}{M_R^2}\{(\epsilon \cdot p_K)(p_\gamma \cdot p) - \frac{1}{M_R^2}(p_K \cdot p)(p_\gamma \cdot p)(\epsilon \cdot p)\}, \end{aligned} \tag{A.1}$$

where M_R is the mass of the intermediate state in the s-channel. Using Eq. (A.1) the vector I^μ can be expressedn by

$$I^\mu = I_1\epsilon^\mu + I_2 p_\gamma^\mu + I_3 p^\mu. \tag{A.2}$$

Similarly, the vector K^μ can be obtained by first defining the following:

$$\begin{aligned}
K_1 &= \frac{1}{M_R^2}\{(p_K\cdot p_\gamma)(p_K\cdot p) - \frac{1}{M_R^2}(p_K\cdot p)^2(\epsilon\cdot p)\} \\
K_2 &= \frac{1}{M_R^2}\{\epsilon\cdot p_K)(p_K\cdot p) - \frac{1}{M_R^2}(p_K\cdot p)^2(\epsilon\cdot p)\} \\
K_3 &= -\frac{1}{M_R^4}\{(p_K\cdot p_\gamma)(p_K\cdot p)(\epsilon\cdot p) - \frac{1}{M_R^2}(p_K\cdot p)^2(p_\gamma\cdot p)(\epsilon\cdot p)\} \\
&- \frac{1}{M_R^4}\{(p_K\cdot p)(\epsilon\cdot p_K)(p_\gamma\cdot p) - \frac{1}{M_R^2}(p_K\cdot p)^2(p_\gamma\cdot p)(\epsilon\cdot p)\}.
\end{aligned} \tag{A.3}$$

Using Eq. (A.3), the vector K^μ can be expressed by

$$K^\mu = K_1\epsilon^\mu + K_2 p_\gamma^\mu + K_3 p^\mu \tag{A.4}$$

The vector J^μ can be expressed by

$$J^\mu = J_1 p_\gamma^\mu + J_2 p^\mu, \tag{A.5}$$

where

$$\begin{aligned}
J_1 &= -(p_K\cdot p_\gamma) + \frac{1}{M_R^2}(p_K\cdot p)(p_\gamma\cdot p) \\
J_2 &= \frac{1}{M_R^2}\{(p_K\cdot p_\gamma)(p_\gamma\cdot p) - \frac{1}{M_R^2}(p_K\cdot p)(p_\gamma\cdot p)^2\}.
\end{aligned} \tag{A.6}$$

The vector N^μ can be expressed by

$$N^\mu = N_1 p_\gamma^\mu + N_2 p^\mu, \tag{A.7}$$

where

$$\begin{aligned}
N_1 &= \frac{1}{M_R^2}\{(p_K\cdot p_\gamma)(p_K\cdot p) - \frac{1}{M_R^2}(p_K\cdot p)^2(p_\gamma\cdot p)\} \\
N_2 &= -\frac{1}{M_R^4}\{(p_K\cdot p_\gamma)(p_K\cdot p)(p_\gamma\cdot p) - \frac{1}{M_R^2}(p_K\cdot p)^2(p_\gamma\cdot p)^2\}
\end{aligned} \tag{A.8}$$

The lorentz scalars a, b, a', and b' appearing alson in Eqs. (4.73) and (4.74) in the s-channel are defined as follows:

$$\begin{aligned}
a &= (p_K \cdot p_\gamma)(p_K \cdot \epsilon) - \frac{1}{M_R^2}(P_K \cdot p_\gamma)(p_K \cdot p)(\epsilon \cdot p) \\
&- \frac{1}{M_R^2}(p_K \cdot p)(p_K \cdot \epsilon)(p_\gamma \cdot p) + \frac{1}{M_R^4}(p_K \cdot p)^2(p_\gamma \cdot p)(\epsilon \cdot p) \\
b &= -\frac{1}{M_R^2}M_K^2(p_\gamma \cdot p)(\epsilon \cdot p) + \frac{1}{M_R^4}(p_K \cdot p)^2(p_\gamma \cdot p)(\epsilon \cdot p) \\
a' &= (p_K \cdot p_\gamma)^2 - \frac{1}{M_R^2}(P_K \cdot p_\gamma)(p_K \cdot p)(p_\gamma \cdot p) \\
&- \frac{1}{M_R^2}(p_K \cdot p_\gamma)(p_K \cdot p)(p_\gamma \cdot p) + \frac{1}{M_R^4}(p_K \cdot p)^2(p_\gamma \cdot p)^2 \\
b' &= -\frac{1}{M_R^2}M_K^2(p_\gamma \cdot p)^2 + \frac{1}{M_R^4}(p_K \cdot p)^2(p_\gamma \cdot p)^2,
\end{aligned} \tag{A.9}$$

where M_K is the mass of the kaon.

The expressions for I^μ, K^μ, J^μ, and N^μ as well as for a, b, a', and b' found in Eqs. (4.78) and (4.79) in the u-channel are identical as those defined above.

Appendix B

The operators $\hat{A}$, $\hat{B}$, $\hat{C}$, and $\hat{D}$ appearing in Eq. (4.97) depend on the spin and parity of the particular intermediate hadron considered. They can all be expressed in terms of a set of Σ and Ω operators defined by the relations

$$\begin{aligned} \Sigma(a,b) &= a_0 b_0 - \sigma \cdot \mathbf{a}\sigma \cdot \mathbf{b} \\ \Omega(a,b) &= b_0 \sigma \cdot \mathbf{a} - a_0 \sigma \cdot \mathbf{b}, \end{aligned} \tag{B.1}$$

$$\begin{aligned} \Sigma_3(a,b,c) &= a_0 \Sigma(b,c) - \sigma \cdot \mathbf{a}\Omega(b,c) \\ \Omega_3(a,b,c) &= a_0 \Omega(b,c) - \sigma \cdot \mathbf{a}\Sigma(b,c), \end{aligned} \tag{B.2}$$

and

$$\begin{aligned} \Sigma_4(a,b,c,d) &= \Sigma(a,b)\Sigma(c,d) + \Omega(a,b)\Omega(c,d) \\ \Omega_4(a,b,c,d) &= \Sigma(a,b)\Omega(c,d) + \Omega(a,b)\Sigma(c,d), \end{aligned} \tag{B.3}$$

where a_0 and $\mathbf{a}$ are the time and space components of the 4-vector a. In terms of these operators, the operators for intermediate baryons with positive parity and spin $\frac{1}{2}$ are

$$\begin{aligned}
\hat{A}_s^{\frac{1}{2}^+} &= FD(p)M_R\Omega(p_\gamma,\epsilon), \\
\hat{B}_s^{\frac{1}{2}^+} &= FD(p)M_R\Sigma(p_\gamma,\epsilon), \\
\hat{C}_s^{\frac{1}{2}^+} &= -FD(p)\Omega_3(p,p_\gamma,\epsilon), \\
\hat{D}_s^{\frac{1}{2}^+} &= -FD(p)\Sigma_3(p,p_\gamma,\epsilon)
\end{aligned} \tag{B.4}$$

in the s-channel and

$$\begin{aligned}
\hat{A}_u^{\frac{1}{2}^+} &= FD(p)M_R\Omega(p_\gamma,\epsilon), \\
\hat{B}_u^{\frac{1}{2}^+} &= FD(p)M_R\Sigma(p_\gamma,\epsilon), \\
\hat{C}_u^{\frac{1}{2}^+} &= FD(p)\Omega_3(p_\gamma,\epsilon,p), \\
\hat{D}_u^{\frac{1}{2}^+} &= FD(p)\Sigma_3(p_\gamma,\epsilon,p)
\end{aligned} \tag{B.5}$$

in the u-channel, where p_γ and ϵ are the photon 4-momentum and polarization, M_R and p are the mass and 4-momentum of the intermediate baryon, and D is the propagator denominator defined by

$$D(p) = (p^2 - M_R^2 + iM_R\Gamma)^{-1}. \tag{B.6}$$

The coupling products F are defined by Eqs (4.31) and (4.32). Note that the intermediate baryon width Γ in Eq. (B.6) is zero in the Born terms. For an intermediate proton there are additional contributions to the operators from the charge coupling. These are given by

$$\begin{aligned}
\hat{A}^{charge} &= eg_{\Lambda Kp}D(p)\Omega(p,\epsilon), \\
\hat{B}^{charge} &= eg_{\Lambda Kp}D(p)\Sigma(p,\epsilon), \\
\hat{C}^{charge} &= eg_{\Lambda Kp}D(p)M_R\sigma\cdot\epsilon, \\
\hat{D}^{charge} &= 0.
\end{aligned} \tag{B.7}$$

For contributions with intermediate spin $\frac{3}{2}$ resonances, we define the coupling parameters

$$\begin{aligned}
\beta_1 &= F_1 + F_2, \\
\beta_2 &= F_2 - 2F_1, \\
\beta_3 &= 3F_1 - F_2
\end{aligned} \tag{B.8}$$

with

$$\begin{aligned}
F_1 &= \frac{G^1}{2M_B M_\pi} D(p), \\
F_2 &= \frac{M_R G^2}{(2M_B)^2 M_\pi} D(p),
\end{aligned} \tag{B.9}$$

where M_B is the mass of the ground state baryon at the photon vertex, and G^1 and G^2 are the couplings defined by Eqs. (4.59) and (4.60). With these definitions, the operators for intermediate resonances of positive parity and spin $\frac{3}{2}$ are given by

$$\begin{aligned}
\hat{A}_s^{\frac{3}{2}^+} &= \frac{1}{3}[\beta_1 \Omega(p_K, k_1) + 2F_1(p_K \cdot p)\Omega(p_\gamma, \epsilon) - 3\Omega(p, q_1) - 2F_1 \Omega_4(p, p_K, p_\gamma, \epsilon)], \\
\hat{B}_s^{\frac{3}{2}^+} &= \frac{1}{3}[\beta_1 \Sigma(p_K, k_1) + 2F_1(p_K \cdot p)\Sigma(p_\gamma, \epsilon) - 3\Sigma(p, q_1) - 2F_1 \Sigma_4(p, p_K, p_\gamma, \epsilon) - 3F_2(p_K \cdot k_1)], \\
\hat{C}_s^{\frac{3}{2}^+} &= \frac{1}{3M_R}[\beta_1 \Omega_3(p, p_K, k_1) + 2F_1(p_K \cdot p)\Omega_3(p, p_\gamma, \epsilon) + 3F_2(p_K \cdot k_1)\sigma \cdot \mathbf{p} \\
&\quad + 3M_R^2 \sigma \cdot \mathbf{q}_1 - 2M_R^2 F_1 \Omega_3(p_K, p_\gamma, \epsilon)], \\
\hat{D}_s^{\frac{3}{2}^+} &= \frac{1}{3M_R}[\beta_1 \Sigma_3(p, p_K, k_1) + 2F_1(p_K \cdot p)\Sigma_3(p, p_\gamma, \epsilon) - 3F_2(p_K \cdot k_1)E \\
&\quad - 3M_R^2 q_1^0 - 2M_R^2 F_1 \Sigma_3(p_K, p_\gamma, \epsilon)]
\end{aligned} \tag{B.10}$$

in the s-channel and

$$\begin{aligned}
\hat{A}_u^{\frac{3}{2}^+} &= \frac{1}{3}[-\beta_3\Omega(k_1,p_K) - 2F_1(p_K\cdot p)\Omega(\epsilon,p_\gamma) + 3\Omega(p,q_1) + 2F_1\Omega_4(p,\epsilon,p_\gamma,p_K)], \\
\hat{B}_u^{\frac{3}{2}^+} &= \frac{1}{3}[-\beta_3\Sigma(k_1,p_K) - 2F_1(p_K\cdot p)\Sigma(\epsilon,p_\gamma) + 3\Sigma(p,q_1) + 2F_1\Sigma_4(p,\epsilon,p_\gamma,p_K) - 3\beta_2(p_K\cdot k_1)], \\
\hat{C}_u^{\frac{3}{2}^+} &= \frac{1}{3M_R}[-\beta_1\Omega_3(p,k_1,p_K) - 2F_1(p_K\cdot p)\Omega_3(p,\epsilon,p_\gamma) - 3F_2(p_K\cdot k_1)\sigma\cdot\mathbf{p} \\
&\quad -3M_R^2\sigma\cdot\mathbf{q}_2 + 2M_R^2F_1\Omega_3(\epsilon,p_\gamma,p_K)], \\
\hat{D}_u^{\frac{3}{2}^+} &= \frac{1}{3M_R}[-\beta_1\Sigma_3(p,k_1,p_K) - 2F_1(p_K\cdot p)\Sigma_3(p,\epsilon,p_\gamma) + 3F_2(p_K\cdot k_1)E \\
&\quad +3M_R^2q_2^0 + 2M_R^2F_1\Sigma_3(\epsilon,p_\gamma,p_K)]
\end{aligned} \tag{B.11}$$

in the u-channel, where E is the energy of the intermediate resonance, p_K is the kaon 4-momentum,

$$\begin{aligned}
k_1 &= (p\cdot\epsilon)p_\gamma - (p\cdot p_\gamma)\epsilon, \\
k_2 &= (p_K\cdot\epsilon)p_\gamma - (p_K\cdot p_\gamma)\epsilon,
\end{aligned} \tag{B.12}$$

and

$$\begin{aligned}
q_1 &= F_1k_2 + \beta_2\frac{p_K\cdot p}{3M_R^2}k_1, \\
q_2 &= F_1k_2 - F_2\frac{p_K\cdot p}{3M_R^2}k_1.
\end{aligned} \tag{B.13}$$

For contributions with intermediate spin $\frac{5}{2}$ resonances, we define the coupling parameters

$$\begin{aligned}
F_1 &= \frac{G^1}{2M_B(M_\pi)^3}D(p), \\
F_2 &= \frac{M_RG^2}{(2M_B)^2(M_\pi)^3}D(p),
\end{aligned} \tag{B.14}$$

where G^1 and G^2 are the coupling products given by Eqs. (4.81) and (4.82), and the linear

combinations

$$\begin{aligned} \xi_1 &= b_1 p_\gamma - b_2 \epsilon, \\ \xi_2 &= a_1 p_\gamma - a_2 \epsilon, \\ \zeta &= q \cdot \epsilon p_\gamma + q \cdot p_\gamma \epsilon, \end{aligned} \tag{B.15}$$

where

$$\begin{aligned} a_1 &= 2q \cdot p_\gamma p_B \cdot \epsilon - q \cdot \epsilon p_B \cdot p_\gamma, \\ a_2 &= q \cdot p_\gamma p_B \cdot p_\gamma, \\ b_1 &= q \cdot p_\gamma p \cdot \epsilon + q \cdot \epsilon p \cdot p_\gamma, \\ b_2 &= 2q \cdot p_\gamma p \cdot p_\gamma \end{aligned} \tag{B.16}$$

with

$$q = p_K - \beta p \tag{B.17}$$

and

$$\beta = \frac{p \cdot p_K}{M_R^2}. \tag{B.18}$$

Four other useful combinations are

$$\begin{aligned} c_1 &= q \cdot \epsilon p_K \cdot p_\gamma + q \cdot p_\gamma p_K \cdot \epsilon - p_K \cdot p_\gamma p_K \cdot \epsilon + \frac{1}{5}\beta_K p \cdot \epsilon p \cdot p_\gamma, \\ c_2 &= (2q \cdot p_\gamma - p_K \cdot p_\gamma) p_K \cdot p_\gamma + \frac{1}{5}\beta_K (p \cdot p_\gamma)^2, \\ c_3 &= \frac{a_1 p \cdot p_\gamma - a_2 p \cdot \epsilon}{M_R^2}, \\ c_4 &= a_1 p_K \cdot p_\gamma - a_2 p_K \cdot \epsilon + p_K \cdot p_\gamma (p_B \cdot p_\gamma p_K \cdot \epsilon - p_B \cdot \epsilon p_K \cdot p_\gamma) \\ &\quad + \frac{1}{5}\beta_K p \cdot p_\gamma (p \cdot p_\gamma p_B \cdot \epsilon - p \cdot \epsilon p_B \cdot p_\gamma) \end{aligned} \tag{B.19}$$

with

$$\beta_K = \frac{m_K^2 + 4(\beta M_R)^2}{M_R^2}. \tag{B.20}$$

In terms of these quantities, we have for positive parity spin $\frac{5}{2}$ resonances

$$\begin{aligned}
\hat{A}_s^{\frac{5}{2}^+} &= F_1[c_1\Omega(p,p_\gamma) - c_2\Omega(p,\epsilon)] + \frac{1}{5}F_2[c_3\Omega(q,p) - \Omega(q,\xi_2)] \\
&\quad + \frac{1}{5}F_1[\frac{1}{M_R^2}\Omega_4(p,q,p,\xi_1) + 2q\cdot p_\gamma \Omega_4(p,q,p_\gamma,\epsilon) - \Omega_4(p,q,\zeta,p_\gamma)], \\
\hat{B}_s^{\frac{5}{2}^+} &= F_2 c_4 + F_1[c_1\Sigma(p,p_\gamma) - c_2\Sigma(p,\epsilon)] + \frac{1}{5}F_2[c_3\Sigma(q,p) - \Sigma(q,\xi_2)] \\
&\quad + \frac{1}{5}F_1[\frac{1}{M_R^2}\Sigma_4(p,q,p,\xi_1) + 2q\cdot p_\gamma \Sigma_4(p,q,p_\gamma,\epsilon) - \Sigma_4(p,q,\zeta,p_\gamma)], \\
\hat{C}_s^{\frac{5}{2}^+} &= F_2\frac{c_4}{M_R}\sigma\cdot p + F_1 M_R[c_1\sigma\cdot p_\gamma - c_2\sigma\cdot\epsilon] - \frac{1}{5M_R}F_2[c_3\Omega_3(p,q,p) - \Omega_3(p,q,\xi_2)] \\
&\quad - \frac{1}{5}F_1[\frac{1}{M_R}\Omega_3(q,p,\xi_1) + 2q\cdot p_\gamma M_R\Omega_3(q,p_\gamma,\epsilon) - M_R\Omega_3(q,\zeta,p_\gamma)], \\
\hat{D}_s^{\frac{5}{2}^+} &= -F_2 c_4\frac{E}{M_R} - F_1 c_1 M_R E_\gamma - \frac{1}{5M_R}F_2[c_3\Sigma_3(p,q,p) - \Sigma_3(p,q,\xi_2)] \\
&\quad - \frac{1}{5}F_1[\frac{1}{M_R}\Sigma_3(q,p,\xi_1) + 2q\cdot p_\gamma M_R\Sigma_3(q,p_\gamma,\epsilon) - M_R\Sigma_3(q,\zeta,p_\gamma)]
\end{aligned} \tag{B.21}$$

in the s-channel and

$$\begin{aligned}
\hat{A}_u^{\frac{5}{2}^+} &= F_1[c_1\Omega(p_\gamma,p) - c_2\Omega(\epsilon,p)] + \frac{1}{5}F_2[c_3\Omega(p,q) - \Omega(\xi_2,q)] \\
&\quad + \frac{1}{5}F_1[\frac{1}{M_R^2}\Omega_4(\xi_1,p,p,q) + 2q\cdot p_\gamma \Omega_4(\epsilon,p,p_\gamma,q) - \Omega_4(p_\gamma,p,\zeta,q)], \\
\hat{B}_u^{\frac{5}{2}^+} &= F_2 c_4 + F_1[c_1\Sigma(p_\gamma,p) - c_2\Sigma(\epsilon,p)] + \frac{1}{5}F_2[c_3\Sigma(p,q) - \Sigma(\xi_2,q)] \\
&\quad + \frac{1}{5}F_1[\frac{1}{M_R^2}\Sigma_4(\xi_1,p,p,q) + 2q\cdot p_\gamma \Sigma_4(\epsilon,p,p_\gamma,q) - \Sigma_4(p_\gamma,p,\zeta,q)], \\
\hat{C}_u^{\frac{5}{2}^+} &= -F_2\frac{c_4}{M_R}\sigma\cdot p + F_1 M_R[c_2\sigma\cdot\epsilon - c_1\sigma\cdot p_\gamma] + \frac{1}{5M_R}F_2[c_3\Omega_3(p,p,q) - \Omega_3(p,\xi_2,q)] \\
&\quad + \frac{1}{5}F_1[\frac{1}{M_R}\Omega_3(\xi_1,p,q) + 2q\cdot p_\gamma M_R\Omega_3(\epsilon,p_\gamma,q) - M_R\Omega_3(p_\gamma,\zeta,q)], \\
\hat{D}_u^{\frac{5}{2}^+} &= F_2 c_4\frac{E}{M_R} + F_1 c_1 M_R E_\gamma + \frac{1}{5M_R}F_2[c_3\Sigma_3(p,p,q) - \Sigma_3(p,\xi_2,q)] \\
&\quad + \frac{1}{5}F_1[\frac{1}{M_R}\Sigma_3(\xi_1,p,q) + 2q\cdot p_\gamma M_R\Sigma_3(\epsilon,p_\gamma,q) - M_R\Sigma_3(p_\gamma,\zeta,q)]
\end{aligned} \tag{B.22}$$

in the u-channel.

For intermediate baryons of negative parity, the $\hat{A}$ and $\hat{B}$ operators are given by the same expressions as for intermediate baryons of positive parity and the same spin; whereas, the $\hat{C}$ and $\hat{D}$ operators are given by expressions that are the negatives of the corresponding positive parity expressions.

For the t-channel, we define the coupling parameters

$$\begin{aligned} \alpha^V &= \frac{G^V_{K^\star}}{M_{sc}} D(p), \\ \alpha^T &= \frac{G^T_{K^\star}}{M_{sc}(M_p + M_\Lambda)} D(p) \end{aligned} \tag{B.23}$$

where M_{sc} is the same scaling mass that appears in Eqs. (4.88) and (4.89), and the $G_{K^\star}$ are the coupling products defined by Eqs. (4.92) and (4.94). In terms of these parameters, the t-channel operators are given by

$$\begin{aligned} \hat{A}^t_K &= 0, \\ \hat{B}^t_K &= e g_{\Lambda K p} D(p) \\ \hat{C}^t_K &= 0, \\ \hat{D}^t_K &= 0 \end{aligned} \tag{B.24}$$

for an intermediate kaon,

$$\begin{aligned} \hat{A}^t_{K^\star} &= i\alpha^T (Ef - \sigma \cdot \mathbf{p}\sigma \cdot \xi), \\ \hat{B}^t_{K^\star} &= -i\alpha^T (E\sigma \cdot \xi - f\sigma \cdot \mathbf{p}), \\ \hat{C}^t_{K^\star} &= i\alpha^V f, \\ \hat{D}^t_{K^\star} &= -i\alpha^V \sigma \cdot \xi \end{aligned} \tag{B.25}$$

for an intemediate $K^{\star}(892)$ resonance, and

$$\begin{aligned}
\hat{A}^t_{K1} &= \alpha^T[\epsilon \cdot p_K \Omega(p, p_\gamma) + E p_\gamma \cdot p_K \sigma \cdot \epsilon], \\
\hat{B}^t_{K1} &= \alpha^T[\epsilon \cdot p_K \Sigma(p, p_\gamma) + p_\gamma \cdot p_K \sigma \cdot \mathbf{p} \sigma \cdot \epsilon], \\
\hat{C}^t_{K1} &= \alpha^V[p_\gamma \cdot p_K \sigma \cdot \epsilon - \epsilon \cdot p_K \sigma \cdot \mathbf{p}_\gamma], \\
\hat{D}^t_{K1} &= \alpha^V \epsilon \cdot p_K E_\gamma
\end{aligned} \tag{B.26}$$

for an intermediate $K1(1270)$ resonance, where p and E are the 4-momentum and energy of the intermediate meson,

$$f = \epsilon \cdot \mathbf{p}_\gamma \times \mathbf{p}_K, \tag{B.27}$$

and

$$\xi = \epsilon \times (E_K \mathbf{p}_\gamma - E_\gamma \mathbf{p}_K). \tag{B.28}$$